

ISSN 2435-7499 (Online)

ISSN 2189-6909 (Print)

December 2022

LASTI

Annual Report

Laboratory of Advanced Science and Technology for Industry
University of Hyogo

Vol.23 (2021)



PREFACE

This annual report reviews the research activities of the Laboratory of Advanced Science and Technology for Industry (LASTI) in the academic year of 2021 which is from April 2021 to March 2022 including research activities using NewSUBARU light source at the SPring-8 site and other research activities carried out at the Center for Advanced Science and Technology (CAST) II. NewSUBARU facility has a 1.0-1.5 GeV electron storage ring, which provides light beams from infrared (IR) to hard X-ray regions, and is the largest university-operated synchrotron light facility in Japan.

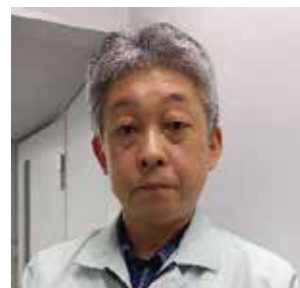
At NewSUBARU, researches are mainly focusing on the academic fields of 1) development of new synchrotron light source technology, 2) the next generation lithography using extreme ultraviolet (EUV) conducted at beamlines BL3, BL9B, BL9C, and BL10, 3) applications of lithographie galvanofornung abformung (LIGA) process technology at BL2 and BL11, 4) materials analysis by X-ray absorption spectroscopy at BL5, BL7 and BL9A, X-ray emission spectroscopy at BL9A, and photoemission spectroscopy at BL7. Other than the synchrotron radiation researches, various researches, such as material syntheses, device fabrication, and microfluid mechanics, are also being conducted at CAST II. Most of our research activities are being conducted in collaboration research works with industries, research institutes, and other universities, inside and outside Japan. We would like to take this opportunity to thank all the collaborators.

Previously, the SPring-8 linear accelerator had also been used to injection of the electron beam to the NewSUBARU electron storage ring in cooperation of the Spring-8 accelerator team. However, the new linear accelerator dedicated to NewSUBARU was installed at the beam transportation tunnel in 2020 and it started operation in April 2021. The construction of the new injector has been completed in great cooperation of the SPring-8 accelerator team. We would like to appreciate the SPring-8 accelerator team for their huge contributions.

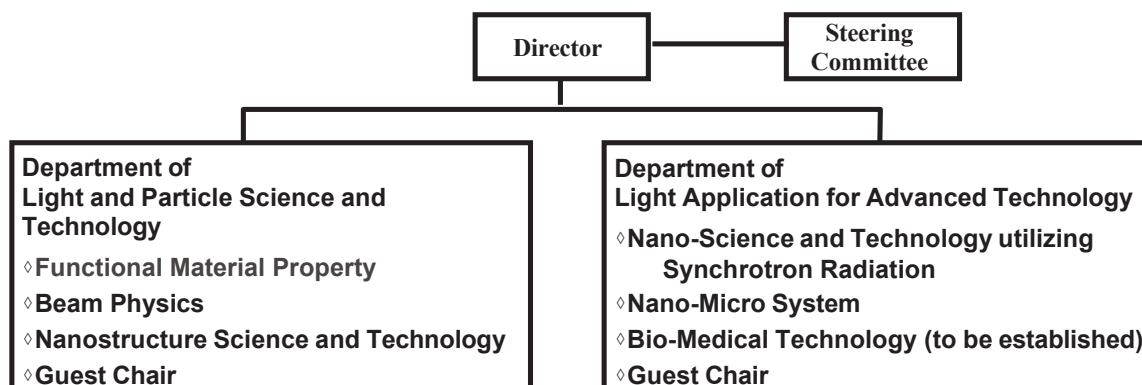
Satoru Suzuki

Satoru Suzuki

Director of Laboratory of Advanced Science
and Technology for Industry, University of Hyogo



The Organization of Laboratory of Advanced Science and Technology for Industry (LASTI) at University of Hyogo



Staff (FY 2021)

Research and faculty staff

WATANABE Takeo, Professor, Director
 KANDA Kazuhiro, Professor
 SUZUKI Satoru, Professor
 UTSUMI Yuichi, Professor
 HARADA Tetsuo, Associate Professor
 HARUYAMA Yuichi, Associate Professor
 HASHIMOTO Satoshi, Associate Professor
 NAKANISHI Koji, Associate Professor
 SHOJI Yoshihiko, Associate Professor
 YAMAGUCHI Akinobu, Associate Professor
 AMANO Sho, Research Associate
 FUJII Satoshi, Research Associate
 YAMAKAWA Shinji, Research Associate

Specially appointed staff

TERANISHI Nobukazu, Professor

Administrative staff

HAYASHI Masahiko, General Manager
 HIROKAGA Yasuhiro, Manager
 KAYAHASHI Hidetoshi, Chief
 AKAMATSU Sumiyo, CAST
 FUJIWARA Riho, CAST
 KONO Kimi, CAST
 YOSHIDA Mizuho, CAST
 MAEDA Yasuhide, CAST
 SENBA Ayako, CAST
 KUSUMOTO Kumi, CAST
 KUWATA Ayami, NewSUBARU

Guest staff

MIYAMOTO Shuji, Professor
 HARADA Yoshihisa, Professor
 HORIBE Hideo, Professor
 KOIKE Masato, Professor
 KUDO Hiroto, Professor
 SASAKI Shigemi, Professor
 SUGIYAMA Munehiro, Professor
 NIIBE Masahito, Associate Professor
 FUKUOKA Takao, Researcher
 KAGEYAMA Hiroyuki, Researcher
 MAEKAWA Satoshi, Researcher
 OKADA Ikuo, Researcher
 OKUI Masato, Researcher
 SAIKI Tsunemasa, Researcher
 SAKURAI Yuuya, Researcher
 TOKUSHIMA Kou, Researcher
 YAMADA Motoyuki, Researcher
 YAMASHITA Kenji, Researcher

Contact address

Advanced Research Building of LASTI

3-1-2 Kouto, Kamigori-cho, Ako-gun, Hyogo, 678-1205 JAPAN.
 Phone: +81-791-58-0249 Fax: +81-791-58-0242

NewSUBARU Synchrotron Radiation Facility

1-1-2 Kouto, Kamigori-cho, Ako-gun, Hyogo, 678-1205 JAPAN.
 Phone: +81-791-58-2503 Fax: +81-791-58-2504

Web URL <https://www.lasti.u-hyogo.ac.jp/english/index.html>
<https://www.lasti.u-hyogo.ac.jp/NS/>

E-mail ns-clerk@lasti.u-hyogo.ac.jp

Access <https://www.lasti.u-hyogo.ac.jp/NS-en/access/>

CONTENTS

PREFACE	i
ORGANIZATION of LASTI	iii
Part 1. Current Status of NewSUBARU and Other Light Source	
Electron accelerators at NewSUBARU	1
Satoshi Hashimoto (<i>LASTI/University of Hyogo</i>)	
NewSUBARU Beamlines	6
Koji Nakanishi (<i>LASTI/University of Hyogo</i>)	
Part 2. Research Activities	
Anomaly Detection of Electron Beam by Machine Learning	17
H. Fujii ¹ , S. Matsuo ² , and S. Hashimoto ¹ (¹ <i>LASTI</i> , ² <i>University of Hyogo</i>)	
Fundamental Evaluation of Resist on EUV Lithography at NewSUBARU Synchrotron Light Facility	19
Takeo Watanabe, Tetsuo Harada, Shinji Yamakawa (<i>Center for EUVL, LASTI, University of Hyogo</i>)	
Synthesis and Characterization of the Polymer Having Photoacid Generator for EUV Resist	24
Shinji Yamakawa, Tetsuo Harada, Takeo Watanabe (<i>Center for EUVL, LASTI, University of Hyogo</i>)	
Relocation and Upgrade of Tender X-ray XAFS Beamline for High-Accuracy and Advanced Measurements	27
Koji Nakanishi (<i>LASTI, University of Hyogo</i>)	
The Effect on Exit Beam Height by Change of Incident Beam Height in Symmetrical Layout Type Double Crystal Monochromator	31
Masato Okui ^{1,2} , Naoki Yato ¹ , Atsushi Shimoguchi ¹ , Norio Murayama ¹ , Ichiro Tsuboki ¹ , and Kazuhiro Kanda ² (<i>¹Kohzu Precision Co., Ltd.</i> , <i>²LASTI, University of Hyogo</i>)	
Structural Changes of Highly Hydrogenated Diamondlike Carbon Films by Soft X-ray Irradiation	34
Daisuke Niwa ¹ , Tomohiro Mishima ¹ , Hibiki Terai ¹ , Koji Nakanishi ¹ , Masahito Niibe ¹ ,	

Kazuhiro Kanda¹, Fuminobu Hori², Atsushi Yabuuchi³, Atsushi Kinomura³
 (¹LASTI, Univ. Hyogo, ²Eng., Osaka Pref., Univ., ³RNS, Kyoto Univ.)

Development of an Improved Multi-Layer Mirror for the New γ-Beam Source via X-Ray Compton Scattering.....	37
Norihito Muramatsu ¹ , Tetsuo Harada ² , Schin Daté ³ , Kazuhiro Kanda ² , Manabu Miyabe ¹ , Shuji Miyamoto ² , Haruo Ohkuma ^{3,4} , Masahiro Okabe ¹ , Hajime Shimizu ¹ , Shinsuke Suzuki ³ , Atsushi Tokiyasu ¹ , Takeo Watanabe ² (¹ ELPH, Tohoku University, ² LASTI, University of Hyogo, ³ RCNP, Osaka University, ⁴ Aichi Synchrotron Radiation Center)	
Reduction of Graphene Oxide by Combination of Atomic Hydrogen Annealing and Soft X-Ray Irradiation.....	39
Akira Heya ¹ , Akinori Fujibuchi ¹ , Masahiro Hirata ¹ , Kazuhiro Kanda ² , and Koji Sumitomo ¹ (¹ University of Hyogo, ² LASTI, University of Hyogo)	
PES and XAS Study of the Effect of Atomic Hydrogen Annealing Treatment for Conductive Thin Film Sb-SnO₂.....	41
Takeshi Fukuda ¹ , Akira Heya ¹ , Takanori Yamamoto ¹ , Ryuki Tsuji ¹ , Yuichi Haruyama ² , Masahito Niibe ² , Satoru Suzuki ² , and Seigo Ito ¹ (¹ Department of Materials and Synchrotron Radiation Engineering, Graduate School of Engineering, University of Hyogo, ² LASTI, University of Hyogo)	
Resonant Photoemission Spectroscopy Study on the 5d Level of Ir Nanoparticles.....	43
Takahiro Maruyama ^{1,2} and Yuichi Haruyama ^{3,4} (¹ Department of Applied Chemistry, Faculty of Science and Technology, Meijo University, ² Nanomaterial Research Center, Meijo University, ³ Department of Materials and Synchrotron Radiation Engineering, Graduate School of Engineering, University of Hyogo, ⁴ Laboratory of Advanced Science and Technology for Industry, University of Hyogo)	
Effect of Atomic Hydrogen Exposure on Hydrogenated Amorphous Carbon Thin Films.....	45
Y. Haruyama ¹ , D. Morimoto ¹ , A. Heya ² , K. Sumitomo ² , S. Ito ² , K. Yokota ³ , and M. Tagawa ³ (¹ Laboratory of Advanced Science and Technology for Industry, University of Hyogo, ² Graduate School of Engineering, University of Hyogo, ³ Graduate School of Engineering, Kobe University)	
Fundamental Study of EUV Mask on EUV Lithography at NewSUBARU Synchrotron Light Facility.....	48
Takeo Watanabe, Tetsuo Harada, Shinji Yamakawa (Center for EUVL, LASTI, University of Hyogo)	
Hydrogen Cleaning Evaluation of Mo/Si Multilayer Using an EUV Irradiation Tool at NewSUBARU.....	54
Tetsuo Harada, Shinji Yamakawa, Takeo Watanabe (Center for EUVL, LASTI, Univ. of Hyogo)	

X-ray Absorption Spectroscopy of Liquids and Gases using a Simple Liquid Cell.....	55
Tomoki Eguchi, Koji Takahara, Satoru Suzuki (<i>LASTI, University of Hyogo</i>)	
In-situ XANES Measurements of the Heated Sugar for Clarifying the Melting Point Fluctuation.....	58
Kae Hiramatsu and Yasuji Muramatsu (<i>Graduate School of Engineering, University of Hyogo</i>)	
In-situ XANES Measurements of Eggs during Heating.....	61
Ikuya Shimogaki and Yasuji Muramatsu (<i>Graduate School of Engineering, University of Hyogo</i>)	
C K-XANES of Long-Chain Aliphatic Carbons Analyzed by the First Principles Calculations.....	63
Toshiyuki Tanaka and Yasuji Muramatsu (<i>Graduate School of Engineering, University of Hyogo</i>)	
Fabrication of Ni-W Microgears Using LIGA Process.....	65
Kohzo Tamada ¹ , Sho Amano ¹ , Kana Okamoto ² , Masaya Takeuchi ^{1,3} , Akinobu Yamaguchi ¹ , Yuichi Utsumi ¹ , and Tohru Yamasaki ² (¹ <i>Laboratory of Advanced Science and Technology for Industry, University of Hyogo,</i> ² <i>Research Center for Advanced Metallic Materials, University of Hyogo,</i> ³ <i>Graduate School of Engineering, University of Hyogo</i>)	
Fabrication of Free-Form Shape Using LIGA Process with Independently Moving X-ray Mask.....	69
Taki Watanabe, Sho Amano, Akinobu Yamaguchi, and Yuichi Utsumi (<i>LAST, University of Hyogo</i>)	
Deviation of Photoelectron Intensity from the Lambert-Beer's Law in Near-Ambient Pressure Hard X-Ray Photoelectron Spectroscopy.....	73
Kento Takenaka ¹ , Nanami Hosoe ¹ , Koji Takahara ² , Tomoaki Eguchi ² , Hirosuke Sumida ³ , Satoru Suzuki ² (¹ <i>Graduate School of Science, University of Hyogo,</i> ² <i>LASTI, University of Hyogo,</i> ³ <i>Mazda Motor Corp.</i>)	
Shape Observation of Micro- and Nanobubbles Formed In-situ in a Scanning Electron Microscope.....	77
Koji Takahara, Satoru Suzuki (<i>LASTI, University of Hyogo</i>)	

List of Publications

- (1) Papers
- (2) International meetings
- (3) Academic degrees

Part 1. Current Status of NewSUBARU and Other Light Source



NewSUBARU Synchrotron Radiation Facility

Electron accelerators at NewSUBARU

Satoshi Hashimoto
LASTI, University of Hyogo

1. Introduction

NewSUBARU synchrotron light facility has a 1.5 GeV electron storage ring, which is the largest accelerator among universities in Japan. For more than 20 years, not only basic research but also student education and industrial use have been carried out using high quality soft X-rays. Synchrotron radiation science and accelerator science are one of the major features of our university.

The new 1.0 GeV linac dedicated to the NewSUBARU ring was constructed in 2020 with the help of SPring-8 accelerator staff. FY2021 was the first year of operation of the storage ring with the new injector, and the two accelerators have been operating without serious failure.

2. Overview of electron accelerators

The general layout of the ring is shown in Figure 1. The ring is consisted with 6 DBA cells with inverse bending magnets. There are 6 straight sections between each cell, and they are used for an injection septum, an accelerating RF cavity and three undulators.

Of the two 15m long straight sections, one is equipped with the 10.8m Long Undulator (LU) and the other is used for both generating Laser Compton Scattering (LCS) gamma-rays and FEL

for generating ultra-short radiation pulse (SC³ project). The main parameters of the ring are listed in Table I. The main feature of this ring is that the stored beam energy is variable in the range of 0.5 to 1.5 GeV.

Table I Main parameters of the NewSUBARU storage ring

Circumference	118.73 m
Lattice	DBA + inv. Bends
Injection beam energy	0.5 – 1.0 GeV
Stored beam energy	0.5 – 1.5 GeV
Mac. Stored current	500 mA
Number of bends	12
Radius of curvature	3.217 m
RF frequency	499.955 MHz
Harmonic number	198
Betatron tunes	6.29(H), 2.22 (V)
Number of IDs	3
Radiation loss per turn	33.4 keV (@1.0GeV)
Energy acceptance	±0.85%
Injection repetition rate	1 Hz

The general layout of the injector linac is shown in Figure 2. The performance of the linac is shown in Table II. The main characteristics of the injector linac are as follows [1].

50 kV gun using gridded thermionic cathode
A composite RF gun with a gridded thermionic

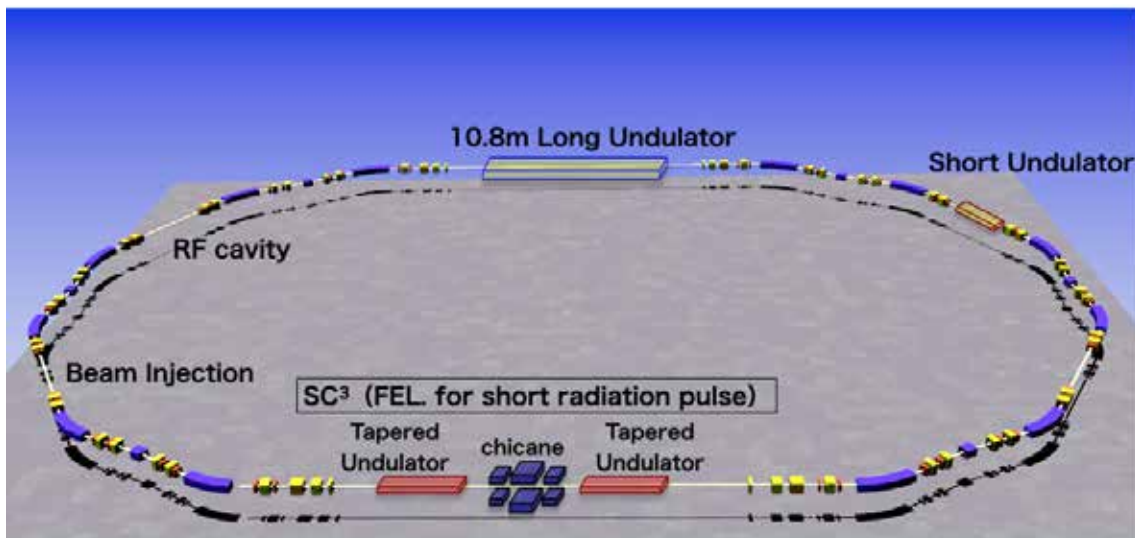


Fig.1. General layout of the NewSUBARU storage ring. Electron beams are injected from the newly-constructed 1.0 GeV linac dedicated to the ring.

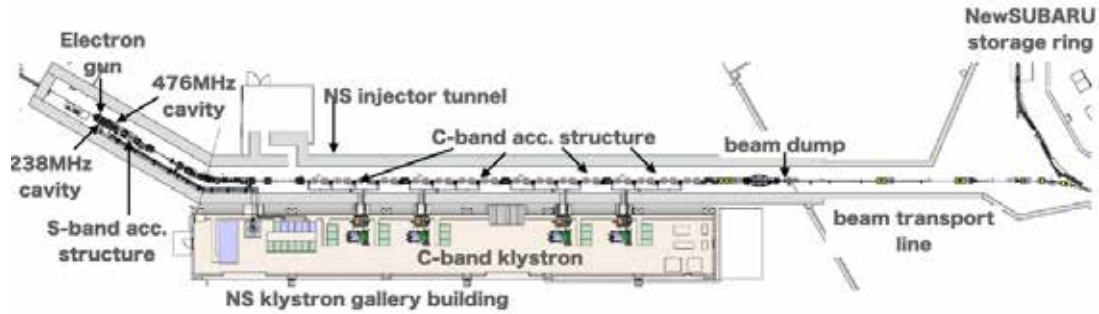


Fig.2. General layout of the 1.0 GeV linac dedicated to the NewSUBARU ring.

cathode is used for generating stable and low emittance beam [2]. Stable emission of a short pulse beam is achieved without any special adjustment.

238 MHz cavity

The electron gun and focusing magnetic lens are mounted in a 238MHz cavity. The 50 keV beam emitted by the electron gun is accelerated by the cavity up to 500 keV to suppress emittance growth due to space charge. The cavity is driven by 42 kW solid state amplifier.

476 MHz cavity

The following 476 MHz cavity provides velocity bunch compression. It decelerates beams from 500 KeV to 270~360 keV providing the energy chirp. Velocity bunch compression reduces the bunch length from 200 ps (FWHM) to several ps at S-band first cavity.

S-band accelerating structure

One S-band accelerating structure is used to accelerate the electron beam up to 50 MeV.

C-band accelerating structure

C-band accelerating structure shown in Figure 3 is the same type as SACLA. It is well proven and has a high acceleration gradient of about 31MV/m [3]. The length of one acceleration tube is 2m. One unit (8.6m, 250MeV) consists of four acceleration tubes and is driven by a C-band klystron. Four units are used for 1.0 GeV acceleration.

Table II Performance of the new injector linac.

	Require	Measurement
Beam Energy	1.0 GeV	1.0 GeV
Bunch charge	100 pC	100 pC
Normalized emittance	<10 mm-mrad	<10 mm-mrad
Energy spread	<±0.5%	0.1% (FWHM)
Energy stability	-	0.4% (STD)
Bunch length	5ps (FWHM)	<1ps (FWHM)
Injection efficiency	>90%	>90%



Fig.3. C-band accelerating structure of the 1.0 GeV linac.

3. Operation Status in FY2021

Our facility has two operation modes for user-time; 1.0 GeV top-up mode and 1.5 GeV current decay mode. The basic operation time is 9:00 - 21:00 of weekdays. Monday is used for machine R&D, Tuesday is for 1.5 GeV user time, Wednesday and Thursday are for 1.0 GeV top-up user time, Friday is for 1.0 GeV or 1.5 GeV user time.

Until FY2020, weekday night and weekend could be used for additional machine study or user time with the special mode, such as a single bunch operation or an operation with arbitrary electron energy. From 2021, the operation of the accelerators has been limited to weekday 9:00-21:00, because the accelerator operation business was outsourced to a private company.

Figure 4 shows the breakdown of machine uptime in FY2021. The total machine time was 1,919 hours, 188% of that of FY2020, excluding the beam down time. The beam down time includes not only the down due to machine trouble, but also the off-beam period after the beam is aborted due to beam instability or erroneous operation. The total down time in FY2021 was about 57 hours, 3 % of the total operation time. The tuning time and study time have increased by about 200 hours in total compared to before the new injector.

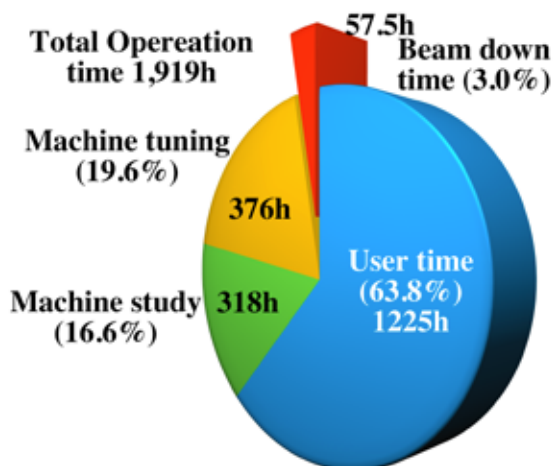


Fig. 4. Operation time of NewSUBARU in FY2021.

4. Machine Trouble

The beam down time in FY2021 was 57 hours. Typical troubles for both hardware and software are as follows.

4-1. Corrosion of high voltage electrodes of sputter ion pump

The high voltage electrode of a sputter ion pump was corroded. The cause is suspected to be radiation and water adhering to the electrode. All pumps will be visually checked this summer.

4-2. Failure of the real-time betatron tune correction system

In normal operation, horizontal and vertical betatron tunes are constantly measured and corrected in real-time if they deviate from optimal values. When evaluating the tune values in real-time from a noisy waveform, a measurement error caused the tune value to shift and the beam to be lost. To solve this problem, we are developing a waveform analysis technique that applies machine learning.

4-3. Vacuum deterioration and RF reflection of C-band klystrons

Among the four klystrons, in order to avoid stop due to RF reflection, CB1 and CB3 are operating at lower power than others.

4-4. Failure of the pulsed power supply for the electron gun

The 50kV power supply failed several times due to insufficient insulation on one of the six high voltage boards. Repairs by the manufacturer solved the problem.

5. Machine Study

In FY2021, we spent a lot of time tuning the

injector linac, but the main theme of ring R&D was the SC³ project aimed at generating ultrashort pulsed light. And another topic was the preparation for resuming gamma-ray use at beamline BL01.

5-1. Tuning of the injector linac

With one year of operation experience, we have become proficient in operating the linac and have endeavored to improve the beam and operation performance. For example,

- Stable operation of the injector for a long period of time.
- Increased beam intensity from linac (0.9nC) and maintenance of high injection efficiency to the ring (~90%).
- Increased stored current in the ring. From 300 to 350 mA at 1.0 GeV top-up. From 350 to 400 mA at 1.5 GeV decay.
- Low energy top-up operation at 0.75 GeV. This is useful for gamma-ray generation and FEL.

5-2. SC³ project (mono-cycle FEL)

Under the collaboration with RIKEN SPring-8 center, University of Hyogo Graduate School of Material Science and LASTI, we are running the SC³ (Slippage-Controlled Coherent radiation by Chirped micro-bunching) project, where the generation of the extremely short radiation pulse corresponding to only a few wavelengths will be experimentally proved at NewSUBARU using arbitrary tapered undulators [4], a magnetic chicane and a chirped seed laser. Main parameters of modulator, radiator and chicane are shown in Table III.

In FY2021, we succeeded in forming micro-bunch in a single electron bunch and observing coherent light. Details will be reported in the near future.



Fig. 5. Insertion device for generating mono-cycle FEL light pulse. Modulator and radiator with high K parameter and a magnetic chicane between them.

Table III Main parameters of SC³ insertion device.

[Modulator/Radiator]	
magnet	permanent
wavelength	15 cm
Number of periods	24
Total length	7.2 m
Max. field	0.7 T
Max. K parameter	10
Gap	280~50 mm
(Gap can be longitudinally tapered)	
[Chicane]	
Magnet	Electromagnet
Number of coils	Main x1, Sub x2
Total length	600 mm
Max. field	0.7 T

5-3. LCS gamma-ray

BL01, a beamline for light source R&D, has been built and upgraded by Prof. Miyamoto and has been used in various studies using LCS gamma rays [5-10]. As shown in fig. 6 and 7, visible or infrared incident laser photons are scattered by high-energy electrons and bounce off as high-energy photons in the γ -ray region.

The beamline was suspended in FY2020. In FY2021, successors learned beamline operation and gamma-ray measurement techniques and the beamline resumed use by outside users in February 2022. Figure 8 shows a typical spectrum of LCS gamma photons using a laser with a wavelength of 1064 nm and an electron beam of 1.0 GeV. We will continue to promote the sophistication and use of gamma-ray light sources.

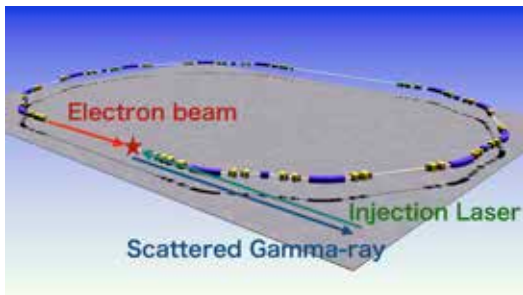


Fig. 6. General scheme of Laser Compton Scattering (LCS) gamma-ray generation at BL01.

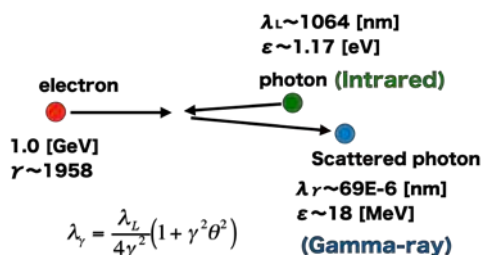


Fig. 7. Typical general scheme of LCS gamma-ray generation at BL01.

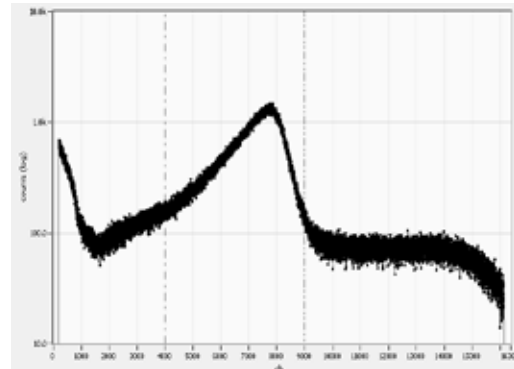


Fig. 8. Typical gamma-ray spectrum measured at BL01.

5-4. Another studies

We conducted several other studies. Examples include developing a beam instability monitor in collaboration with KEK, operating the ring at the new operating point, measuring lattice functions and circulating beam parameters, optimizing pulsed magnets for injection, and readjusting the beam monitor.

Summary

In FY2021 the operation of the 1.0 GeV injector linac and the storage ring of NewSUBARU was generally smooth. We have gained a lot of experience in operating new injectors. The stable supply of high-quality electron beams from the injector has improved the performance of the storage ring.

Currently, it is difficult to secure sufficient operating days in FY2022 due to soaring electricity prices. However, we will continue to advance the sophistication of accelerators, develop new light sources and provide industrial support by providing a stable supply of high-quality synchrotron radiation.

Acknowledgements

We would like to express our sincere gratitude to the accelerator staff at RIKEN SPring-8 center, JASRI and SES for their great cooperation in the operation of the injector linac. We would also like to thank to Dr. Y. Minagawa, Mr. K. Kajimoto, Mr. H. Hirayama, Mr. S. Nakata of SES for their machine operation. And we greatly thanks to Mr. T. Ushizawa and Dr. T. Sakurai of JASRI for their efforts for stable operation of accelerators.

References

- [1]"Construction of a Compact Electron Injector Using A Gridded Rf Thermionic Gun And A C-Band Accelerator", T. Inagaki†, T. Fukui, T. Hara, T. Hiraiwa, H. Maesaka, H. Tanaka, T. Asaka, H. Dewa, N. Hosoda, E. Iwai, C. Kondo,

- T. Magome, T. Ohshima, T. Sakurai, K. Yanagida, S. Inoue, K. Kajimoto, Y. Minagawa, S. Nakata, T. Seno, H. Sumitomo, R. Takesako, S. Tanaka, R. Yamamoto, M. Yoshioka, S. Hashimoto, IPAC2021, WEPAB039 (2021)
- [2] T. Asaka, *et. al.*, Phys. Rev. Accel. Beams 23, 063401 (2020)
- [3] T. Inagaki, *et. al.*, PRST-AB 17, 080702 (2014)
- [4]“Development of an undulator with a variable magnetic field profile”, T. Tanaka, Y. Kida, R. Kinjo, T. Togashi, H. Tomizawa, S. Hashimoto, S. Miyamoto, S. Okabe, Y. Tanaka, Journal of synchrotron radiation 28, p.404-409 (2020)
- [5]“High-energy photon beam production with laser-Compton backscattering”, K. Aoki *et al.*, Nuclear Instruments and Methods in Physics Research A 516 (2004) 228–236
- [6] “Laser Compton back-scattering gamma-ray beamline on NewSUBARU”, Shuji Miyamoto *et al.*, Radiation Measurements 41 (2007) S179–S185
- [7] “Measurements for the energy and flux of laser Compton scattering g-ray photons generated in an electron storage ring: NewSUBARU”, Ken Horikawa *et al.*, Nuclear Instruments and Methods in Physics Research A 618 (2010) 209–215
- [8] “Half-life of ^{184}Re populated by the (γ, n) reaction from laser Compton scattering γ rays at the electron storage ring NewSUBARU”, T. Hayakawa *et al.*, PHYSICAL REVIEW C 74, 065802 (2006)
- [9]“Experimental Study of Photoneuclear Reactions of Light Nuclei with NewSUBARU γ -ray Beam”, Tatsushi Shima *et al.*, Proc of Science-NIC X. 148 (2008)
- [10] “New Results on Photodisintegration of ^4He ”, Tatsushi Shima *et al.*, Proc of Science-CD09, 107 (2009)

NewSUBARU Beamlines

Koji Nakanishi
LASTI, University of Hyogo

The arrangement of the beamlines in the NewSUBARU synchrotron radiation (SR) facility is shown in Fig.1. Total nine beamlines are operating in the NewSUBARU SR facility.

Four beamlines of BL01, 03, 06 and 11 were constructed until 1999. Three beamlines of BL07, 09 and 10 were started the operation from 2000.

BL02 beamline was constructed for the usage of LIGA in 2003.

BL03B beamline branched from the BL03 beamline propose for the usage of the EUVL (extreme ultraviolet lithography) microscope for the EUVL finished mask inspection.

BL05 was built to perform industrial analysis by soft X-ray XAFS and PES. A major upgrade was started in 2020 for more effective use. A part of BL05 was relocated to BL06, and its performance was upgraded.

A new photoemission electron microscope (PEEM) has been installed on BL09A.

BL09B beamline branched from BL09 beamline for the usage of the EUV interference lithography to evaluate. And BL09C beamline branched from BL09B beamline for the usage of the thickness measurement of the carbon contamination originated to the resist outgassing during the EUV exposure.

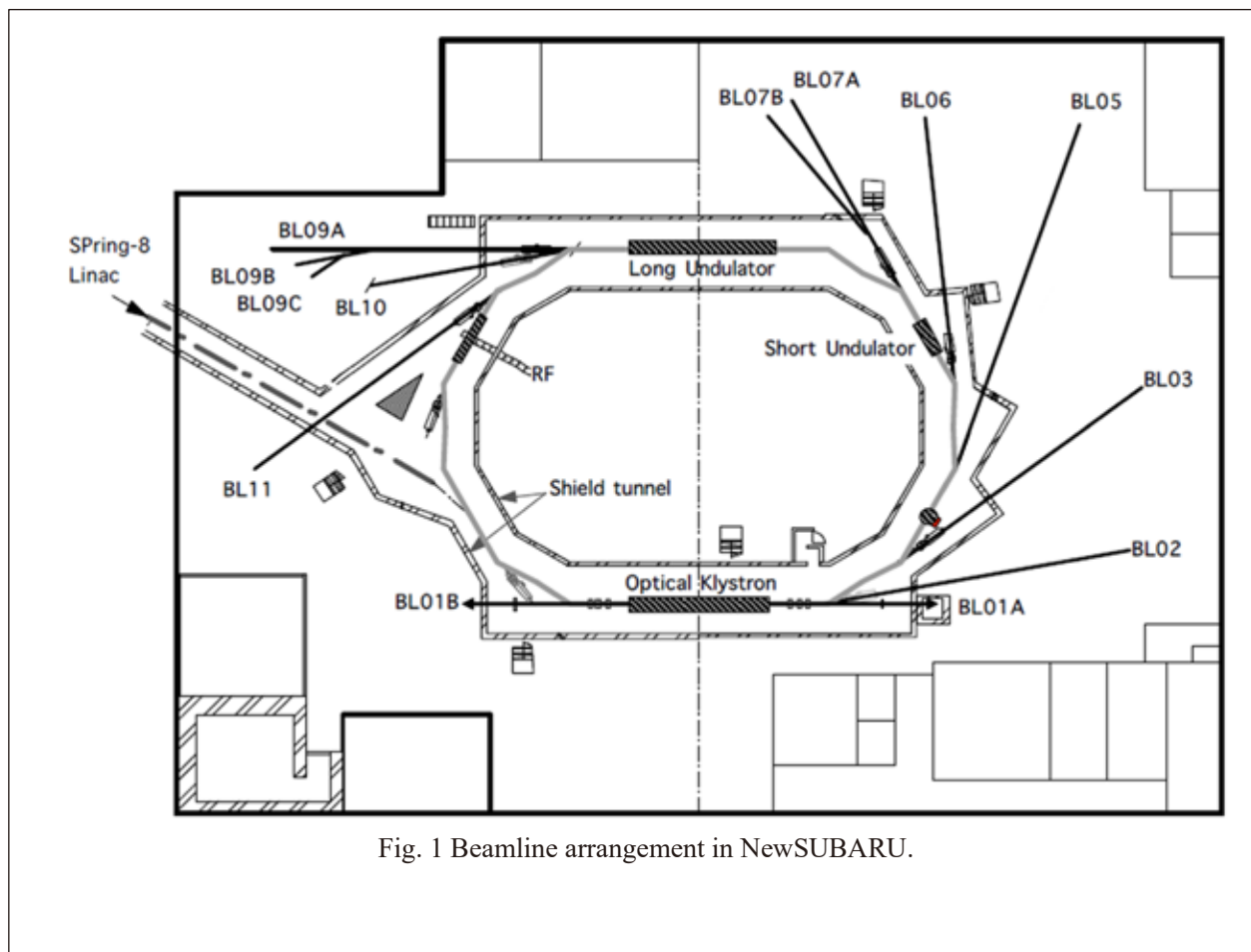


Fig. 1 Beamline arrangement in NewSUBARU.

I. BL01

BL01 is a beamline for research and developing new light sources. This beamline is one of two long straight section on NewSUBARU. Optical klystron was installed at this straight section. Upstream side of this beamline (BL01B) is intended to be used for visible and infrared light generated from free electron laser (FEL) or synchrotron radiation (SR). Downstream side of this beamline (BL01A) is used

for laser Compton scattering gamma-rays source. Gamma-ray beamline hutch just outside of the storage ring tunnel was constructed in 2004 for gamma-ray irradiation experiments. Specification of this gamma-ray sources are listed in Table 1. New gamma-ray irradiation hutch "GACKO" was installed at BL01A. Table 2 shows the specification of "GACKO".

Table 1. Specification of BL01 gamma beam

CO ₂ laser 10.52 μm 5W	Gamma energy : 1.7 - 4 MeV Gamma flux*: $9 \times 10^6 \gamma/\text{s}$: $6 \times 10^5 \gamma/\text{s}$ (1.5-1.7 MeV) (with 3mm ϕ collimator)
Nd laser 1.064 μm / 0.532 μm 5 W	Gamma energy : 17 - 40 MeV Gamma flux*: $7.5 \times 10^6 \gamma/\text{s}$: $3 \times 10^5 \gamma/\text{s}$ (15-17 MeV) (with 3 mm ϕ collimator)

*Electron beam energy : 1-1.5 GeV

*Electron beam current : 250 mA

*Gamma-ray beam divergence : 0.5 mrad

Table 2. Specification of "GACKO"

Maximum gamma-ray power	0.33 mW
Maximum gamma-ray energy	1.7 MeV - 73 MeV
CO ₂ laser, wavelength/power	10.59 μm / 10W
1-1.7 MeV gamma-ray flux	$2 \times 10^7 \gamma/\text{sec}@10\text{W}/300\text{mA}$
Nd:YVO ₄ laser, wavelength/power	1.064 μm / 30W, 0.532 μm / 20W
10-17 MeV gamma-ray flux	$5 \times 10^7 \gamma/\text{sec}@30\text{W}/300\text{mA}$

II. BL02

The LIGA (abbreviated name of Lithographic, Galvanoformung and Abformung) process which consists from deep X-ray lithography, electroforming, and molding process is one of the promising candidates for such 3D micofabrication. More than hundreds aspect ratio for microstructure can be attained by the usage of the higher energy X-rays (4-15 keV) from synchrotron radiation (SR) with deeper penetration depth to the photosensitive resist. In this system we have succeeded to enlarge the exposure area up to A4 size and the fabrication dimension from submicron to millimeter by varying the energy of the

X-ray source in accordance with the size of desired microparts. Microstructure with high aspect ratio over several hundred will be achieved using the X-rays over 10 keV since high energy X-ray has deep penetration depth to the photo-sensitive resist materials. Whereas, in the case of lithography for low energy X-rays from 1 keV to 2 keV, submicron structures with high aspect ratio will be achieved using the X-rays mask with precise line-width and thinner absorber, since low energy X-rays has low penetration depth. Based on this principle, the beamline for x-ray exposure have constructed with

continuous selectivity of X-rays from 100 eV to 15 keV by using the X-ray mirrors (plane and cylindrical mirror) and Be film filters. The horizontal angle of the outgoing SR could be obtained up to 12.5 mrad, which corresponds to the horizontal size of 220 mm (A4 horizontal size) at the exposure position. The second characteristic performance of the beamline is the high efficiency differential pumping system. This was necessary for maintain the vacuum difference between the storage ring ($<10^{-9}$ Pa) and the end-station ($<10^{-9}$ Pa) at which gasses for substrate cooling will be introduced in the exposure apparatus.

The flexibility for the shapes and functions of microstructure will be enlarged by achieving 3D

microfabrication process using multi step exposure at various configuration between X-ray mask and substrates. The relative positions between X-ray mask and substrates, tilt and rotation angle to the SR incident direction can be moved simultaneously during SR exposure using 5 axis stages. The movement of each axis is controlled by the PC in terms of the scanning speeds, scanning length, and repetition number. In order to decrease the heat load of sample substrate suffered during SR irradiation helium introduction and substrate cooling mechanism were also equipped. Specification of spectrometer is listed in Table 3.

Table 3. Specification of the LIGA exposure system

Optics	Plane and cylindrical mirror, Be filters
Exposure energy	0.1 - 2 keV, and 4 – 15 keV
Exposure method	Proximity and multi-step exposure
Wafer size	A4 or 8 inch
Exposure area	230 mm(H) × 300 mm(V)
Exposure environment	< 1 atm (He-gas)

III. BL03

BL03 is a beamline for the developing the next generation lithographic technology so called extreme ultraviolet (EUV) lithography. The extreme ultraviolet lithography (EUVL) is a promise technology for fabricating a fine pattern less than 7-nm node. There are (1) a EUV resist-sensitivity evaluation tools, (2) a VUV reflectometer, and (3) an EUV microscope with Schwarzschild optics. At (1) tool, EUV resist is exposed with SR light of EUV monochromatized by 7 Mo/Si multilayer mirrors. The exposure spectrum of this tool was same as the ASML exposure tools. The monochromator of (2)

reflectometer was UV – VUV reflectometer. At EUV lithography, out-of-band radiation (100 – 300 nm) of EUV source degrades image quality. Thus, optics and resist property of out-of-band region was essential to evaluate, for example EUV mask reflectivity, and EUV resist sensitivity. The monochromator specification was shown in Table 4. The EUV microscope (3) has Schwarzschild optics, which were fabricated with collaboration of Dr. Toyoda (Tohoku Univ.). The spatial resolution was quite high of less than 28 nm, which was equal to 7 nm at wafer printing size.

Table 4. VUV monochromator specification

Mount type	Collimate plane grating monochromator
Grating	Plane Grating (1,000 lines/mm)
Energy range	4 - 120 eV (UV ~ VUV)
Resolving power (E/ΔE)	~ 1000

IV. BL05

BL05 was constructed in response to a demand in the industry, which is enhancement of the analysis ability in the soft x-ray region with the development of nanotechnology. BL05 consists of two branch lines for use in the wide range from 50 eV to 4000 eV. BL05A and BL05B are designed to cover the energy range of 1000-4000 eV and 50-1000 eV, respectively. The incident beam from the bending magnet is

provided for two branch lines through different windows of a mask. Therefore, these two branch lines can be employed simultaneously.

However, both beamlines had many problems and did not perform well enough for industrial and advanced analysis. In order to solve these problems, a drastic upgrade was started in 2020.

New BL05A

The constant-deviation monochromator consisting of a demagnifying spherical mirror and a varied-line-spacing plane grating (VLSPG), which can provide high resolution, simple wavelength scanning with fixed slits, was mounted on BL05A. The optical system consists of a first mirror (M0), a second mirror (M1), an entrance slit (S1), a pre-mirror (M2), and three kinds of plane grating (G), an exit slit (S2) and a focusing mirror (M3). The including angle of the monochromator is 175°. Two measurement chambers for XAFS and PES are prepared at the end station of

BL05A. XAFS spectra in the total electron yield mode and partial fluorescence yield using a silicon drift detector can be measured in a high vacuum chamber. In addition, photoelectron spectra can be measured using spherical electron analyzer (VG Sienta, R3000) in an ultrahigh-vacuum chamber. The chambers can be replaced by each other. Table 6 shows the specification of the monochromator.

BL05B changed its name to BL05A due to the relocation to BL06, which will be described later.

Table 5. Monochromator specification

Monochromator	Varied-line-spacing plane grating monochromator
Grating	100 lines/mm, 300 lines /mm, 800 lines /mm
Energy range	50 - 1000 eV
Resolution	$E/\Delta E=3000$

V. BL06

BL06 had been constructed for irradiation experiments such as photochemical reaction, SR-CVD, photo-etching, surface modification. BL06 for irradiation experiments was closed due to plans to build a new beamline for XAFS measurement. An X-ray mirror, Golovchenko-type double crystal monochromator, measurement systems and many other beamline components were relocated from old BL05A. New BL06 plans to have two XAFS beamlines, tender X-rays and hard X-rays, in the

future. First, the hard X-ray beamline was prepared. A Rh-coated collimating mirror with incident/reflected angle of 0.3 degrees was selected for this beamline, which allows the photon energy of not only 5-12 keV but 1-3 keV. Since the use of hard X-rays required the development of a new dedicated measurement hatch, we first installed the tender X-ray XAFS measurement system developed for the former BL05A. Table 6 shows the specification of monochromator.

Table 5. Monochromator specification

Monochromator	Double crystal monochromator
Monochromator crystals	Beryl(10-10), KTP(011), quartz(10-10), InSb(111), Ge(111), Si(111), Si(220), Ge(220), Si(331), Ge(331)
Energy range	1 - 3 keV, and 5-12 keV(in future)

VI. BL07

This beamline was designed for the development of new materials by SR technology. This beamline consists of two branch lines, which are provided with an incident beam from a 3-m-long undulator by switching the first mirror. One of them is a high photon-flux beamline with a multilayered-mirror monochromator for the study of SR-process (BL07A) and another is a high-resolution beamline with a varied line spacing grating monochromator for the evaluation of nano-structure characteristics by SR-spectroscopy (BL07B). The useful range of emitted photons from 50 to 800 eV is covered at both beamlines. The light source of BL07 is a 3-m length planar undulator, which consists of 29 sets of permanent magnets, a period length of which is 76 mm. The incident beam from the undulator is provided for two branch lines by translational switching of first mirror.

1) BL07A

The multilayered-mirror (MLM) monochromator, which has high reflectivity in the soft X-ray region, was installed at the BL07A. It consists of a switching mirror chamber, a slit chamber, a MLM monochromator, a filter chamber and a reaction chamber. To obtain a large photon flux, we decided to

use only first mirror (switching mirror), M0, for focusing. The MLM monochromator is designed to cover an energy range of up to about 800 eV by combination of three kinds of mirror pairs with 4 kinds of filter. The flux deliver by this design is estimated to be between a maximum of 10^{17} photons/s at 95 eV and a minimum 2×10^{14} photons/s at 300 eV for a 500 mA ring current. Table 7 shows the summary of BL07A. In addition, X-ray fluorescence (XRF) apparatus using spherical varied line spacing grating was mounted at the downstream of irradiation chamber. The poly capillary was used to enhance beam-condensing efficiency. Measurement energy range was from 30 eV to 450 eV. This XRF apparatus was expected to utilize the chemical analysis on the light metals, Li and Be, and light elements, B, C and N.

Two novel vacuum chambers were installed in 2019 for the measurement of inverse Compton scattering of soft X-rays. One large chamber with a size of W1120×D820×H610 mm³ was set up 16.7 m downstream of the undulator center. A multi-layer mirror was placed on high precision auto-stages inside this chamber with cooling water circulation. The other chamber was installed 2.6 m upstream of the large mirror chamber, in order to monitor radiated and reflected X-rays.

Table 7. Summary of BL07A.

Energy range (eV)	Multilayer mirror					Filter	
	Material	Spacing	Thickness Ratio	Number of layers	$\Delta E/E$	Material	Thickness
50-60	Mo/Si	20 nm	0.8	20	6.2 %	Al	100 nm
60-95						None	-
90-140	Mo/B ₄ C	11 nm	0.5	25	3.3 %	Ag	100 nm
140-194						Cr	500 nm
190-400	Ni/C	5 nm	0.5	60	2.5 %	Ni	500 nm
400-560							
550-800							

2) BL07B

The constant-deviation monochromator consisting of a demagnifying spherical mirror and varied line spacing plane grating (VLSPG), which can provide to high resolution, simple wavelength scanning with fixed slits, was mounted on BL07B. The optical system consists of a first mirror (M0), an entrance slit (S1), a pre-mirror (M1), and three kinds of plane grating (G), an exit slit (S2) and two focusing

mirrors (M2 and M3). The monochromator is designed to cover the energy range 50-800 eV with three gratings, of which including angle are 168° . The VLSPG has been well known to obtain high resolution in extreme ultraviolet region by diminishing various kinds of aberration. The total resolving power about 3000 can be realized in the whole energy region. Table 8 shows the specification of the monochromator.

Table 8. Monochromator specification

Mount type	Hettrick-Underwood type
Grating G1, G2, G3	Plane VLS (600, 1200, 2400 l/mm)
Energy range	50-150 eV, 150 – 300 eV, 300-800 eV
Resolving power ($E/\Delta E$)	~ 3000

VII. BL09

A purpose of this beamline is studies on a soft x-ray interferometry or a holographic exposure experiment with making use of highly brilliant and coherent photon beams radiated from 11 m long undulator in NewSUBARU.

BL09 consists of M0 mirror, M1 mirror, G grating and M2 mirror. M0 mirror is used for horizontal deflection and beam convergence, M1 is used for vertical beam convergence at the exit slit, and M2 is used for vertical deflection and beam convergence. A monochromator is constructed by M1 and a plane grating. The maximum acceptance of the undulator beam is 0.64 mrad in horizontal and 0.27 mrad in vertical. The acceptance can be restricted by 4-jaw slits equipped at upstream of the M0 mirror.

1) BL09A

BL09A beamline is used for material analysis: X-ray absorption spectroscopy (XAS) and X-ray photoelectron spectroscopy (XPS). In 2013, X-ray

emission spectrometer (XES) was introduced at the end-station of the BL-09A. The energy range and resolving power of the XES system was designed to be about 50-600 eV and 1500, respectively. In 2021, a photoemission electron microscope system has been installed on BL09A.

2) BL09B

BL09B beamline branched from BL09 beamline for the usage of the EUV interference lithography for the evaluation of the exposure characteristics of EUV resist. Coherence length of 1 mm at the resist exposure position was achieved using BL09B beamline. And BL09C beamline branched from BL09B beamline for the usage of the thickness measurement of the carbon contamination originated to the resist outgassing during the EUV exposure. Table 9 shows the specification of the monochromator.

Table 9. Monochromator specification

Mount type	Monk-Gillieson type
Grating	Plane VLS (300, 900, 1200 l/mm)
Energy range	50 – 750 eV
Resolving power ($E/\Delta E$)	~ 3000

VIII. BL10

BL10 is for EUV reflectometry and soft X-ray analysis. M0 mirror is used for horizontal deflection and beam convergence, M1 is used for vertical beam convergence at the exit slit, and M2 is used for vertical deflection and beam convergence. A monochromator is constructed by M1 and a plane grating. At the beginning, the multilayer reflectivity measurement was carried out at this beamline. The characteristics of this beamline and the result of the Mo/Si multilayer measurement are carried out for the development of the EUV-mask technology.

BL10 utilizes a monochromator of the varied-line-spacing plane grating (VLS-PGM). The line density of the monochromator in central region of the gratings were 600, 1800 and 2,400 lines/mm. The reflectometer has a two-axis vacuum goniometer. One axis carries the sample, which may be a mirror surface at the center of the reflectometer vacuum chamber (θ -motion). The other (ϕ -motion) carries the detector on a rotating arm.

In addition, there are linear motions to translate the sample in two orthogonal directions (x, y). All motors are controlled by computer. The reflectivity result obtained at BL10 has a good agreement with that at LBNL. Table 10 shows the specification the monochromator.

The micro-CSM tool was adapted at the most downstream of the BL10 beamline for the EUV mask defect inspection with coherent-diffraction-imaging method. This too is very effective for the inspection of the actinic patterned mask with phase imaging.

A large reflectometer was installed in a branch line for large EUV optical component including EUV collector mirrors. The reflectometer has a sample stage with y, z, θ, ϕ , and Tilt axis, which can hold large optical elements with a maximum weight of 50 kg, a diameter of up to 800 mm, and a thickness of 250 mm. The entire sample surface is able to be measured.

Table 10. Monochromator specification

Mount type	Monk-Gillieson type
Grating	Plane VLS (600, 1800, 2400 l/mm)
Energy range	50 – 1,000 eV
Resolving power ($E/\Delta E$)	~ 1000

IX. BL11

A beam line BL11 is constructed for exposure Hard X-ray Lithography (DXL) in the LIGA (German acronym for Lithographie Galvanoformung and Abformung) process. LIGA process, that utilizes a useful industrial application of SR, is one of the promising technologies for fabrication of extremely tall three-dimensional (3D) microstructures with a large aspect ratio. This process was invented at the Institut Fur Mikrostrukturtechnik (IMT) of the Karlsruhe Nuclear Center (KfK) in 1980. Microstructures with height of over a few hundred μm have been widely applied to various fields such as micro-mechanics, micro-optics, sensor and actuator technology, chemical, medical and biological engineering, and so on. This beam line was designed by the criteria; photon energy ranges from 2 keV to 8 keV, and a density of total irradiated photons $\geq 10^{11}$ photons/cm². The BL11 can provide the most suitable photon energy for microfabrication in X-ray lithography, while the BL2 is equipped for fabricating fine pattern

submicron-scale structure and microstructure with high aspect ratio by selectivity of X-rays using movable mirror system. That is, LIGA process in NewSUBARU can provide the best 3D microfabrication because the BL11 and BL2 are complementary. The beamline BL11 is consisting of an absorber chamber, a first-mirror chamber (M1), a 4-way slit chamber, a Be and polyimide window chamber, and an exposure chamber. The horizontal angle of the outgoing SR could be obtained up to 17.8 mrad, providing a beam spot size on the exposure stage $\geq 80 \times 10 \text{ mm}^2$. The micron-scale structure with high aspect ratio will be achieved using the toroidal typed mirror M1 which can produce a parallel collimated beam of X-rays. In addition, the homogeneity of the beam is excellently controlled by a novel adding system.

Using the precision stage in the exposure chamber, the flexibility for the shaped and functions of microstructure will be enlarged by achieving 3D microfabrication process using multi step exposure at

various configuration between x-ray mask and substrates. The exposure area of 200 mm × 200 mm is brought to fruition. In order to decrease the heat load of sample substrate suffered during SR

irradiation, helium introduction and substrate cooling system were also equipped. The specification of the LIGA exposure system is listed in Table 11.

Table 11. Specification of the LIGA exposure system

Exposure method	Proximity exposure
Wafer size	8 inch
Exposure area	200 mm(H)×200 mm(V)
Exposure environment	< 1atm (He-gas)

Establishment of Research Center for Advanced Synchrotron Radiation Analysis

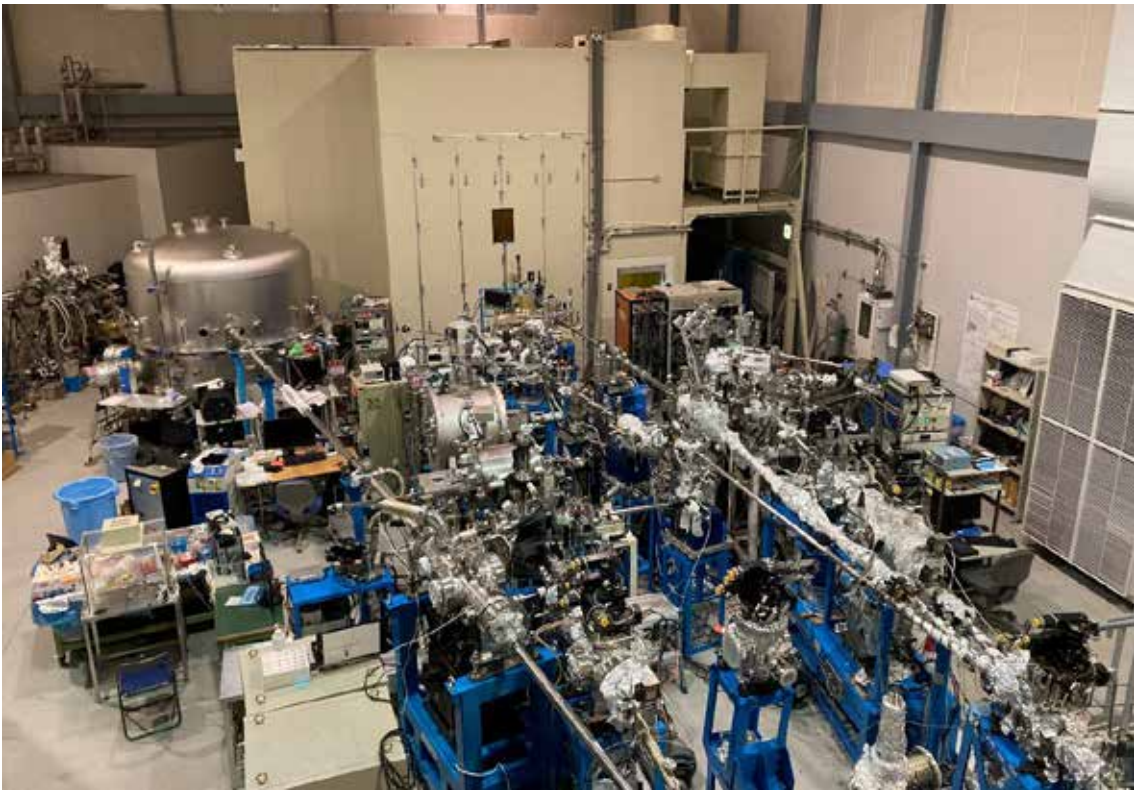
In order to respond to diverse analysis needs from industries, it is necessary to advance technological development for analyzing beamlines (BLs) of NewSUBARU SR facility to advance integrated and strategic development of analyzing technology. For this reason, the Research Center for Advanced SR Analysis was launched in August 2016. As an

organization crossing in university courses, this center is consulted and administered by all members of the LASTI related to analysis, and in collaboration with the SR Nanotechnology Center of Hyogo Prefecture, a wide range of energy from hard X-rays to soft X-rays. We aim to respond to various analysis needs of the area on a one-stop basis.

Acknowledgement

We would like to thank all the staff who work at NewSUBARU synchrotron radiation research facility for their help to describe the update details of the beamlines.

Part 2. Research Activities



EUVL R&D Beamlines

Anomaly Detection of Electron Beam by Machine Learning

H. Fujii¹, S. Matsuo², and S. Hashimoto¹
¹LASTI, ²University of Hyogo

Abstract

In NewSUBARU synchrotron light facility, various researches and developments have been carried out to realize an automatic anomaly detection system. With this system, it is possible to detect anomalies about synchrotron radiation monitor images, beam current values, and beam lifetimes. However, this anomaly detection system has a problem that correct judgment is difficult for undefined anomalies because this system is based on thresholds that are predefined by humans. Therefore, we are currently conducting research to construct a more accurate and flexible anomaly detection system by using machine learning techniques.

1. Introduction

When electron beam is injected and stored in the storage ring, some anomalies such as a decrease in injection efficiency, stored beam current, and lifetime, and fluctuations in the size of the synchrotron light source may occur. Figure 1 shows the anomalies in the beam current. In top-up operation mode, since the beam current is added at intervals of a second, it is normal that a constant value is maintained as shown in Fig. 1 (a). However, in an anomaly situation like (b), it can be seen that the current value is greatly reduced. On the other hand, in decay operation mode, it is normal that the current value is gradually decay as shown in Fig. 1 (c). If there is an anomaly, the slope of the current value is steep as shown in Fig. 1 (d). Such anomalies may be caused by a misconfiguration and performance deterioration of component equipment and changes in temperature of air and cooling water. At present, in order to deal with these anomalies, operators manually access a database which store the setting parameters and measurement values of each devices, extract relevant data, identify the cause, and take a corrective action. However, this process is time-consuming and needs resident operators familiar with beam physics. Therefore, we developed an automatic anomaly detection system. However, this system is based on manually defined thresholds given by past trouble reports. Therefore, this system cannot make a correct judgment when an undefined anomaly occurs, and it is necessary to add a new threshold in order to deal with it.

In order to solve these problems, we are developing a more accurate and flexible anomaly detection system by using machine learning techniques.

2. Experiment

In this research, autoencoder, which is a kind of neural network, is used as an anomaly detection system. Autoencoder consists of at least three layers:

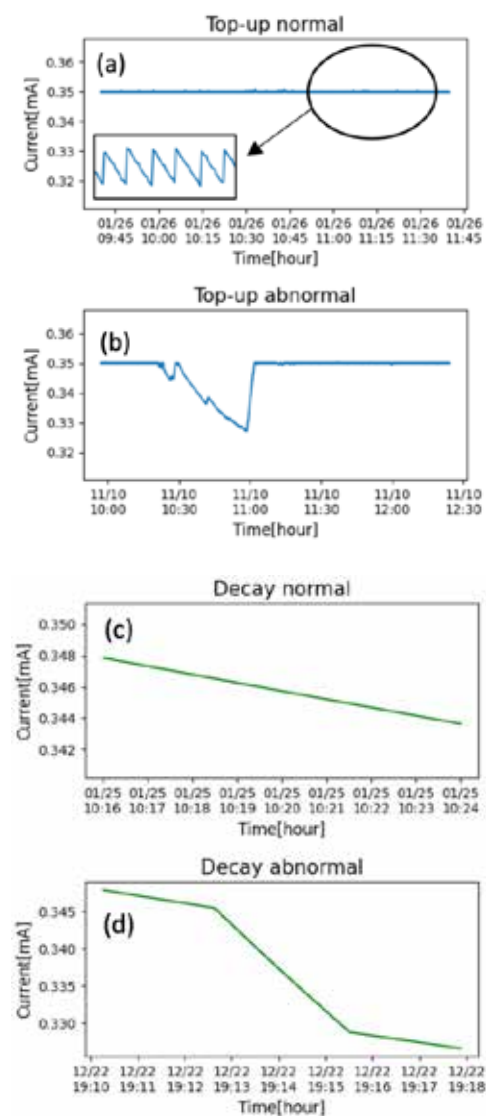


Fig. 1. Examples of stored electron beam current in storage ring. (a) and (b) are normal and anomaly current data, respectively, for top-up operation mode. (c) and (d) are for decay operation mode.

input layer, intermediate (hidden) layer, and output

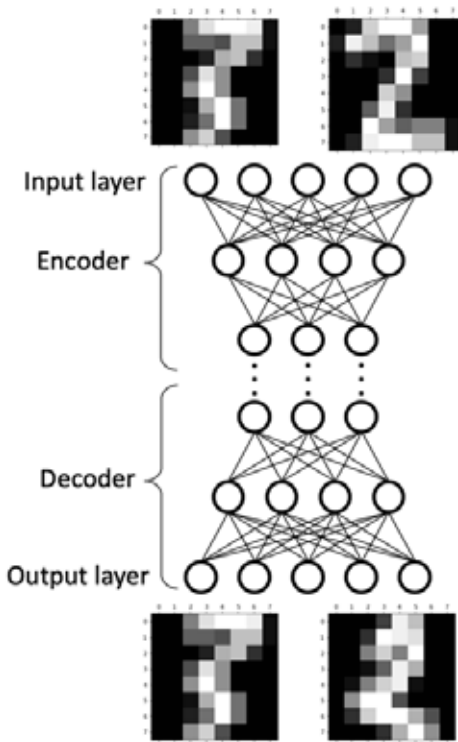


Fig. 2. Schematic illustration of Autoencoder.

This network is supposed to have learned the shape of the fig. 3.

layer. The network is trained to output the data as it is input. Here, it is important to reduce (compress) the number of features (nodes) in the intermediate layer. This forces the network to acquire a compressed representation of the input data as shown in the figure 2. In the figure, if we give the image of figure of *three* to the autoencoder that has learned various images of *three*, it should output in its original form if the learning is sufficient. Now, if we give this autoencoder an image of *two*, it will fail to reconstruct the image of *two* because the network has not learned any compressed representation for the image of *two*. That is, autoencoder has the property that it can successfully reconstruct expected (normal) input data, but cannot reconstruct unexpected (anomaly) input data. Therefore, it become possible to judge whether an input is normal or anomaly just by evaluating the difference between the input and output data without defining what is anomaly. The difference between is evaluated quantitatively by mean squared error (MSE),

$$MSE = \frac{1}{N} \sum_{i=1}^N (y_i - t_i)^2,$$

where, y_i and t_i are output and input data, respectively. N means the number of sample data. This MSE value is the only threshold for the automatic anomaly detection system.

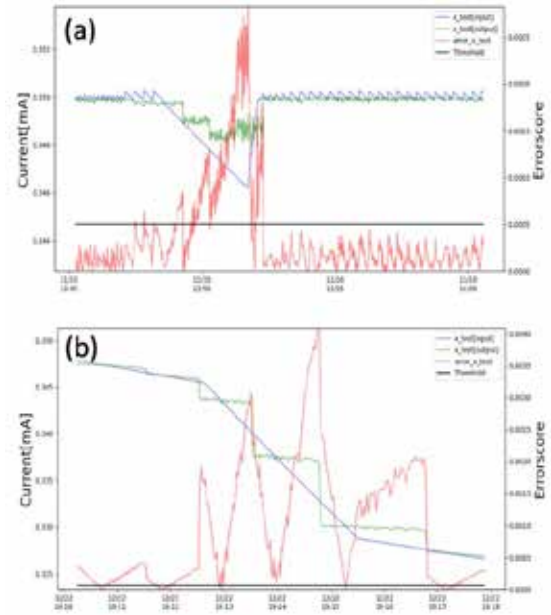


Fig. 3. Results of autoencoders. (a) is for top-up mode and (b) is for decay mode. Blue and green lines are input and output, respectively. Red line means mean squared error.

3. Results and Discussions

The learning of the autoencoder was performed separately for top-up and decay operations. For training, normal current data divided into a minute (60 points) were used. Figure 3 shows the input and output results of the autoencoder. It can be seen that the learning of the normal data is not sufficient and the input cannot be completely reproduced. To further improve the accuracy, it is necessary to increase the number of hidden layers and optimize the hyperparameters of the autoencoder. However, since the reconstruction error for normal data is smaller enough than that for anomaly data, it is possible to sufficiently detect anomaly.

In this study, the stored electron beam current value was analyzed separately for two operation modes. However, if the expression capability of the autoencoder is increased, it will be possible to detect anomalies in both top-up and decay modes simultaneously with a single autoencoder. In the future, we also plan to build a highly accurate anomaly detection system for other data such as beam lifetime, degree of vacuum, electromagnet excitation current.

Fundamental Evaluation of Resist on EUV Lithography at NewSUBARU Synchrotron Light Facility

Takeo Watanabe*, Tetsuo Harada, and Shinji Yamakawa

*Center for EUVL, Laboratory of Advanced Science and Technology for Industry,
University of Hyogo, 3-1-2 Kouto, Kamigori-cho, Akou-gun, Hyogo 678-1205,
Japan*

**takeo@lasi.u-hyogo.ac.jp*

Extreme ultraviolet lithography was started to use for the production of 7-nm node-logic-semiconductor devices in 2019. And it was adapted to use for high volume manufacturing (HVM) of 5-nm logic devices in 2020. EUVL is required to be extended to use in 1.5-nm-node-device fabrications. However, it still has many technical issues. Especially, for EUV resists, simultaneous achievement of high sensitivity and low line edge width are required. To solve the EUV resist issue, the fundamental work using synchrotron in soft X-ray region is necessary. The fundamental evaluation study of EUV resist at NewSUBARU synchrotron light facility is described in this paper.

Keywords: EUVL, resist, sensitivity, line edge roughness, EUV, soft X-ray, resonant scattering, reflectivity measurement, out of band patterning, photo-electron emission microscopy

1. Introduction

Extreme ultraviolet lithography (EUVL) was started to use for the production of 7-nm-node-logic-semiconductor devices. In addition, EUVL technology has finally begun to be used as high-volume-mass-production technology since 2020. EUV technology is going to extend to use in the fabrication of 1.5-nm node devices. EUVL still has technical issues such as EUV resist development, defect free mask fabrication including metrology and pellicle, and EUV high power and stable light source. Especially, it is required that EUV resist which has high resolution and sensitivity, low line width roughness (LWR), and low outgassing [1]. In the EUV resist technical issues, the simultaneous achievement of high resolution and sensitivity, and low LWR is very significant and not so easy. Thus, more fundamental studies are still needed.

Even if the resist material itself has high resolution, as trying to replicate a resist pattern which has narrower width, the pattern collapse interferes the fine-pattern replication. In order to increase the resolution, preventing from the pattern collapse is necessary. Thus, the fundamental study of the structure analysis of resist films using synchrotron is necessary.

In order to increase the sensitivity, studying the whole chemical reactions which occur by the EUV irradiation is necessary. And the development of EUV resist material with high sensitivity based on this study is significant. Since, the wavelength of EUV light and EUV photon energy is 13.5 nm and 91.8 eV, respectively, secondary electron ionization reaction occurs by the high energy electron region. To clarify the reaction by low energy region, it is necessary to use the fundamental evaluation using synchrotron radiation in soft X-ray region.

In addition, to achieve the low LWR resist, the fundamental study of the origin of LWR is necessary. In this study, it is also necessary to use the fundamental evaluation using synchrotron radiation in soft X-ray region as describe later. As above reasons, the fundamental evaluation studies of EUV resist at NewSUBARU synchrotron light facility [2], University of Hyogo, are described in this paper. Total nine beamlines are operating, and three beamlines which are BL03, BL09, and BL10 of NewSUBARU. We have the EUV flood exposure tool for the resist sensitivity evaluation by the actual EUV light spectrum, interference

lithographic exposure tool for the patterning 10 nm and below, outgassing and contamination growth evaluation tools by ellipsometry, and chemical reaction analysis by the soft X-ray spectroscopy (XAS). In addition, recently it is prepared additional tools for the fundamental studies of EUV resists. This paper focuses that 1) resist-film layer analysis by the resonant soft X-ray reflectivity method in soft-X-ray energy region, 2) stochastic origin analysis in EUV resist by resonant soft X-ray scattering to achieve low LWR, 3) out of band systematic analysis, and 4) preparation of the photo-electron emission microscopy for the chemical content spatial distribution analysis.

2. Layer Analysis by the Resonant Soft X-ray Reflectivity Method in soft-X-ray Energy Region

For the layer analysis [3, 4] of the single layer resist material which has a thickness of 20 – 50 nm, the resonant soft X-ray reflectivity (RSoXR) method in soft-X-ray energy region is a powerful method for the chemical layer analysis of the resist film [5]. This method is the hybrid method using soft X-ray absorption spectroscopy [6, 7] and soft X-ray reflectance measurement. By the soft X-ray absorption spectroscopy, the incident energy of the photon is selected for the soft X-ray reflectance measurement to evaluate refractive index of n and k values, and thickness of a resist film coated on a wafer. The reflectivity fringe spectrum can be fit by n and k values, and thickness of the layers.

The commercial chemical amplified (CA) resist was employed for the layer analysis. The resist was spin-coated on a 4 inches silicon wafer to have 26-nm thick. Then the layer analysis was carried out. As a result, the fitting result is shown in Table.1. Even if the CA resist for a single layer process, the thin resist film consists of three layers. The bottom, main body, and top layers have the thickness of 4.5 nm, 14.1 nm, and 7.4 nm, respectively. And these layers have the complex refractive index of k value of 0.0007, 0.0003, and 0.0004, respectively. The bottom layer between the main body layer might be a pattern collapse region.

Table 1. Result of fitting

Layer name s	Thickness (nm)	n	k	Roughness (nm)
Top	7.4	0.9996	0.0004	0.22
Main body	14.1	0.9996	0.0003	3.51
Bottom	4.5	0.9999	0.0007	4.83
SiO ₂	0.8	0.9946	0.0018	0.1
Si wafer	--	0.9951	0.0028	--

3. Stochastic Origin Analysis in EUV Resist by Resonant Soft X-ray Scattering

The low LWR is necessary to maintain the electronic characteristics of semiconductor device, such as logic and memory devices.

The origin of the LWR might be 1) spatial distribution of functional material in resist functional groups, photosensitizers (acid generators), additives such as amines, and so on, 2) spatial distribution of free volume caused by the solvent distribution in prebake process, 3) EUV photon shot noise, 4) secondary electron blur, 5) solvent effect in PEB process acid diffusion, 6) spatial distribution of developer penetration and development process yield caused by developer and rinse effects, and 7) out of band (OoB) light effect.

In order to reduce LWR of the resist pattern, the controls of the above stochastics are significant. In the above list, in order to control the chemical reaction fluctuation within the nanometer dimensions, the special distribution control of the chemical contents is very significant. However, up to now the measurement of the chemical-contents distribution has not been carried out. Thus, the method of resonant soft X-ray scattering (RSoXS) is used for the measurement. This method is the hybrid method using soft X-ray absorption spectroscopy [6, 7] and soft X-ray scattering as shown in Fig. 1. The scattering vector is defined by the following equation.

$$q = |\vec{q}| = \frac{4\pi}{\lambda} \sin \frac{\theta}{2} \quad (1)$$

By the soft X-ray absorption spectroscopy, the incident energy of the photon is selected for the soft X-ray scattering to obtain the selected chemical-bonding diffraction image. The

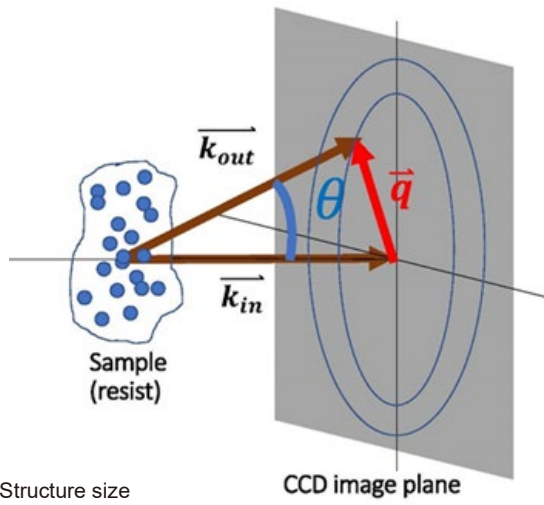


Fig. 1 Scattering vector q .

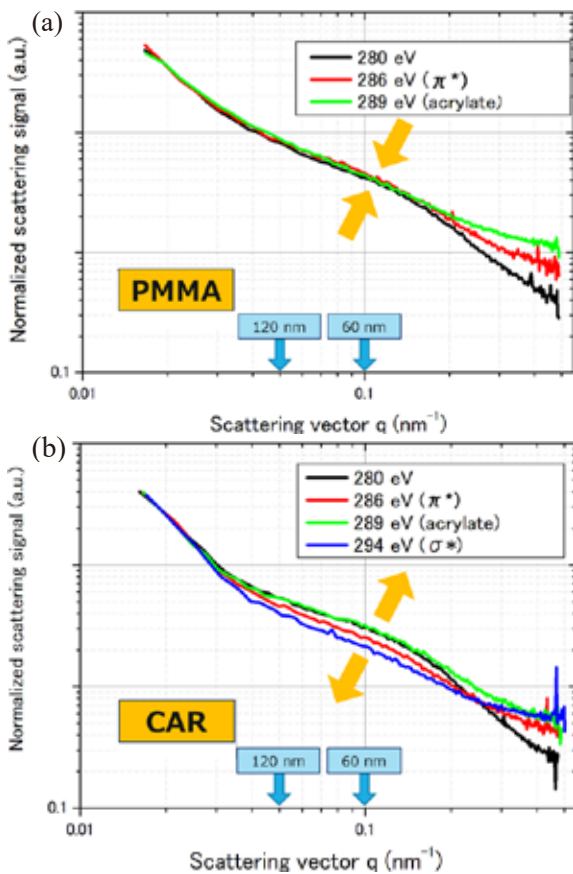


Fig. 2 Scattering vector profiles of (a) PMMA and (b) CAR.

RSOXS system at BL-10 beamline of NewSUBARU was used for this experiment [8, 9]. This beamline provides monochromatized energy of the soft X-ray region from 80 to 1000 eV [10].

The scattering vector profiles of PMMA and CA resist are shown in Figs 2(a) and 2(b). The Scattering vectors of 0.05 and 0.07 nm^{-1} correspond to the structure size of 120 nm and 60 nm, respectively. As the results, the spatial distributions between the π^* bonding and acrylate group are very similar in PMMA. However, these are quite different in CA resist. Generally, since the LWR of PMMA is smaller than that of CA resist, the results of the scattering vector profiles are consistent to the LWR tendency [11].

4. Out of Band Systematic Analysis

If the resist exposed by the light which includes the out of band (OoB) light containing the deep UV wavelength region, the OoB lights affects to the LWR of the resist pattern. Thus, reflectance measurement of the mask materials such as Mo/Si multilayer, absorber, and black border (mask substrate surface). Figure 3 shows the beamline setup of the exposure tool and reflectometer by the EUV and OoB lights at BL03A beamline of NewSUBARU. The monochromator setups to enable the EUV at the wavelength of 10 - 80 nm and OoB light at the wavelength of 100 - 200 nm are shown in Figs

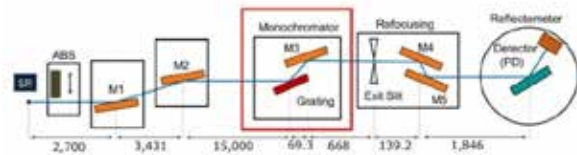


Fig. 3 Beamline setup of the EUV and OoB light exposure tool and reflectometer.

4(a). and 4(b), respectively. And LiF filter with a thickness of 1 mm were used to cut the high order lights which is shorter than the wavelength of 100 nm. The reflectance measurement results of the mask materials such as Mo/Si multilayer, absorber, and black border (mask substrate

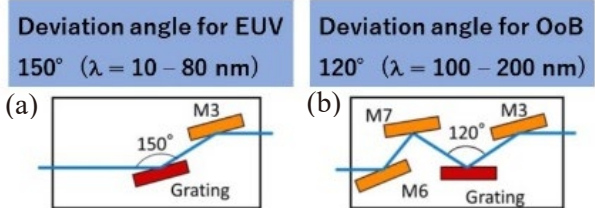


Fig. 4 The monochromator optics for (a) EUV and (b) OoB wavelength regions.

surface) are shown in Fig. 5. The reflectance spectrum of the Mo/Si multilayer was measured completely in the EUV region including high order lights. In the OoB region, the reflectance of Mo/Si multilayer, TaN absorber, and mask substrate as a black border has approximately 30% in maximum. Even if the black border, it has the reflectance of 30%, and the reflectance reduction method should be required.

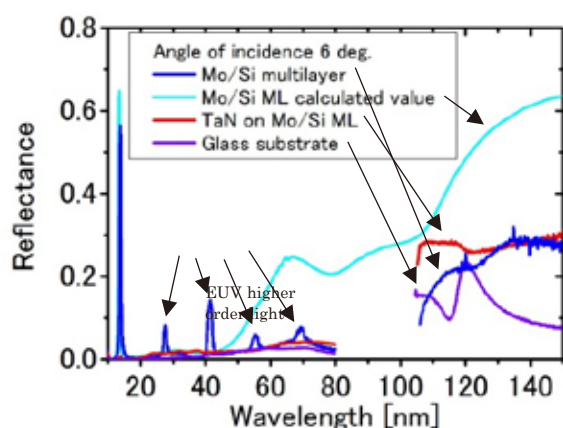


Fig. 5 Reflectance spectra of Mo/Si multilayer, TaN absorber on Mo/Si multilayer, and black border.

5. Preparation of Photo-Electron Emission Microscopy for the Chemical Content Spatial Distribution Analysis

As described in section 3 of RSoXS is one of the methods to observe the chemical-content distribution. However, since the scattering method is used, the averaged distribution is obtained. Instead of this method, we introduce the photo-electron emission microscopy (PEEM) to observe the real chemical content distribution not an averaged one of resist film.

The PEEM system is going to be installed at the BL09A beamline of NewSUBARU. The 3D design is shown in Fig. 6. The PEEM system consists of load lock chamber to exchange a sample, sample processing chamber adapted the ion beam cluster and sample heating device, and the sample observation chamber adapted the PEEM device. In order to prevent from the vibration and to achieve high spatial resolution in PEEM, the special mechanism is employed.

NewSUBARU is a middle size synchrotron light facility and soft X-ray synchrotron radiation is generated from the 1.0 GeV electron beam storage ring. The soft X-ray absorption spectroscopy in the soft X-ray region is suitable

for the chemical analysis of the light atomic elements such as carbon, nitrogen, oxygen, and fluorine etc. Thus, the PEEM in soft X-ray region can observe the chemical imaging of these atomic elements. Since the penetration depth of the soft X-ray is small enough to observe the surface chemical imaging of the resist film, the cluster ion beam tool is employed for the no damage-surface etching of the resist film and enable the chemical imaging in 3D of the resist film.

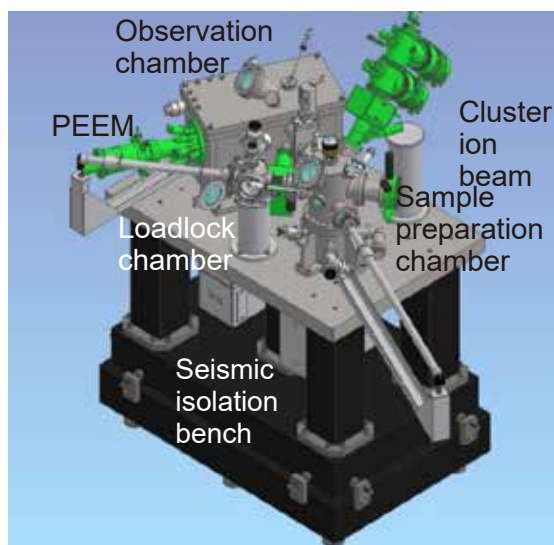


Fig. 6 3D design of the PEEM system.

6. New Injector for NewSUBARU

Photograph NewSUBARU Synchrotron light facility which consists of new linear accelerator for the injection and electron beam storage ring is shown in Fig. 7.

The SPring-8 linear accelerator which had been used as an injection of the electron beam both to SPring-8 and NewSUBARU electron beam storage rings in cooperation of the SPring-8 accelerator team, previously. This linear accelerator was shut down on July 29, 2020. From April to December, the new linear accelerator for NewSUBARU was installed at the beam transportation tunnel. This length of the new linear accelerator has a length of approximately 50-m-long and it is a half-length of the previous one. The new one employed the microwave frequency of approximately 6 GHz (C-band microwave) and it is double frequency of the previous one (S-band microwave) to shortening the length.

The commissioning of NewSUBARU phase II will start from April 20, 2021. After the beamline

tuning, user time will be operated at electron beam current of 350 mA in electron energy of 1.0 GeV top-up mode. In addition, 1.5 GeV operation will be started at the same time.



Fig. 7 Photograph of NewSUBARU Synchrotron light facility.

7. Conclusions

The RSoXR method is introduced to evaluate the chemical-layer separation of the CAR, and it is sensitive enough to it. In the single layer resist, the preventing from the pattern collapse at the boundary between the bottom and main body layer might be significant for the fine patterning.

The RSoXS method is introduced to evaluate uniformity of resist material distribution, which can modulate absorption contrast of functional group by changing the incident photon energy around carbon absorption edge. The RSoXS results are clarified the uniformity of resist material structure, which can highlight the issues to design the low LWR performance.

The out of band systematic analysis tool was prepared at BL03 beamline. In the OoB region, the reflectance of Mo/Si multilayer, TaN absorber, and mask substrate as a black border has approximately 30% in maximum. Even if the black border, it has the reflectance of 30%. And the reflectance reduction method of the OoB lights should be required for the low LWR achievement of the resist patterning.

In order to achieve low LWR, construction of the photo-electron emission microscopy to

analyze the chemical content spatial distribution analysis is in progress.

Construction of new injector for NewSUBARU is in progress toward the NewSUBARU phase II operation to start from April 20, 2021.

References

1. *International Symposium on Extreme Ultraviolet Lithography*, (2021) Closing remarks.
2. Web site of NewSUBARU Synchrotron facility, <http://www.lasti.u-hyogo.ac.jp/NS/>
3. M. Nakagawa, *Jpn. J. Polym.Sci. Tech.* **68** (2019) 24 (in Japanese)
4. M. Nakagawa, T. Uehara, Y. Ozaki, T. Nakamura, and S. Ito, *J. Vac. Sci. Technol. B* **36** (2018) 06JF02.
5. T. Ishiguro, J. Tanaka, T. Harada, and T. Watanabe, *J. Photopolym. Sci. Technol.* **32** (2019) 333.
6. K. Tsuji and Y. Muramatsu Ed., “*X-ray Spectroscopy*,” *Spectroscopy Series, The Spectroscopical Society of Japan (in Japanese)*, Kodansya, 2018, ISBN 978-4-06-513038-4.
7. T. Ohta, “*X-ray Absorption Spectroscopy*,” *IPC, in Japanese*, 2017, ISBN 9784901493215.
8. J. Tanaka, T. Ishiguro, T. Harada, and T. Watanabe, *J. Photopolym. Sci. Technol.* **32** (2019) 327.
9. J. Tanaka, T. Ishiguro, T. Harada, and T. Watanabe, *J. Photopolym. Sci. Technol.* **33** (2020) 491.
10. M. Kuki, T. Uemura, M. Yamaguchi, T. Harada, T. Watanabe, Y. Muramatsu, and H. Kinoshita, *J. Photopolym. Sci. Technol.*, **28** (2015) 531.
11. B. Cardineau, P. Garczynski, W. Earley, and R. L. Brainard, *J. Photopolym. Sci. Technol.* **26** (2013) 665.

Synthesis and Characterization of the Polymer Having Photoacid Generator for EUV Resist

Shinji Yamakawa, Tetsuo Harada, Takeo Watanabe

Center for EUVL, Laboratory of Advanced Science and Technology for Industry (LASTI), University of Hyogo

Abstract

In extreme ultraviolet (EUV) lithography, the development of new resist materials is a one of the significant issues. It is known that there are two types of the chemical amplification resists (CARs), such as photoacid generator (PAG) blend resist (a mixture of PAG and polymer) and PAG bound resist (polymers having PAG unit in sidechain). However, there are few research targeting the PAG bound resists. In this paper, we report the synthesis and characterization of new PAG bound resist.

1. Introduction

The next generation EUV photoresist is needed to satisfy with half pitch of smaller than 10 nm, sensitivity of higher than 15 mJ/cm², and low line width roughness (LWR) of lower than 1 nm. It is known that there are two types of the CARs, such as PAG blend resists and PAG bound resists. The PAG blend resist is a mixture of the polymer, PAG, and amine additive in the solvent. On the other hand, the bound resist is the polymer having PAG unit in side chain. The difference of the blend and bound resists has been reported. For example, Watanabe *et al.* have reported that the bound resist is more less line edge roughness (LER) than blend resist [1]. The reason of low LER for bound resist is expected that the uniformity of bound resist is better than blend one, however, the chemical composition distribution analysis has not been evaluated.

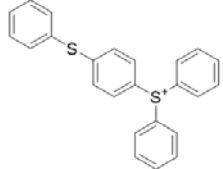
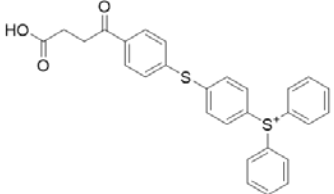
In this study, we synthesized a new PAG bound resist and evaluated the dose estimation by EUV irradiation and the chemical composition distribution by contact angle measurement.

2. Experimental

2.1. Materials

Dimethylsulfoxide-*d*₆ (DMSO-*d*₆), diethyl ether (Et₂O), tetrahydrofuran (THF), γ -butyl lactone, propylene glycol monomethyl ether acetate (PGMEA), dimethyl amino pyridine (DMAP), 1-(3-dimethylaminopropyl)-3-ethylcarbodiimide hydrochloride (EDC·HCl), and dehydrated dimethyl formamide (DMF) were used as purchased. hexamethyldisilazane (HMDS), poly(hydroxystyrene-*co-tert*-butylacrylate) (PHS-TBA), were purchased from Tokyo Ohka Kogyo Ltd. PAG-1, 2 were provided by San-Apro Ltd. Table 1 shows the structure of PAGs which were employed in this study.

Table 1. Summary of PAG structures.

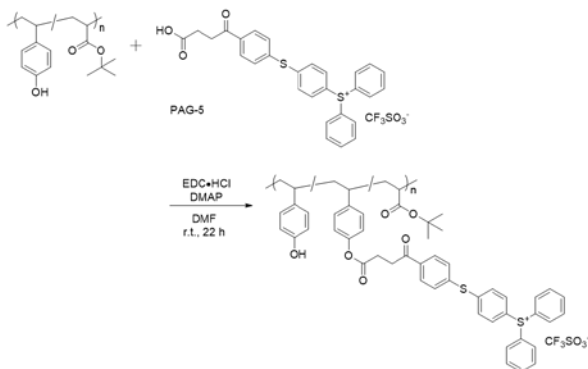
PAG	Structure	
	Cation	Anion
PAG-1		CF ₃ SO ₃ ⁻
PAG-2		CF ₃ SO ₃ ⁻

2.2. Measurements

NMR (¹H and ¹⁹F{¹H}) spectra were recorded on JEOL JNM-ECZ600R (600 MHz) spectrometer. The peaks were referenced to DMSO (δ 2.50) in the DMSO-*d*₆ solvent for ¹H NMR. Gel permeation chromatography (GPC) was performed at 60 °C on Waters Alliance e2695 HPLC system equipped with a differential refractometer detector e2998 and a variable-wavelength UV-vis detector e2410, using DMF (10 mmol/L phosphoric acid and KBr) as eluent at a flow rate of 0.6 mL min⁻¹ with Shodex AsahiPak GF-7HMQ columns. The molecular weights were calibrated based on polystyrene standards. The image of the droplet profile and calculate contact angle were recorded on Excimer SImage Entry 6. Dose estimation was examined at NewSUBARU BL03 [2].

2.3. PAG-2 introducing to the side chain of base polymer

It can be introduced into phenolic acid group under mild conditions due to PAG-2 has carboxylic group. Thus, the condensation reaction of PAG-2 and PHS-TBA was examined (Scheme 1).



Scheme 1. The condensation reaction of PHS-TBA with PAG-2.

PHS-TBA (1239 mg, 5.0 mmol), EDC·HCl (105 mg, 0.55 mmol), DMAP (10 mg, 0.082 mmol) and PAG-2 (311 mg, 0.50 mmol) were charged to 50 ml two-necked flask and purged N_2 gas. Dehydrated DMF (10 ml) was added to mixture then stirred at r.t. for 22 h. After the reaction, the reaction mixture was poured into water (150 ml). The resulted solid was obtained by suction filtration and dried under vacuum for 6 h at 60 °C. The obtained crude product was dissolved a small amount of THF, and the mixture solution was poured into a large amount of Et_2O . The resulted solid (79% yield) was obtained by suction filtration and dried under vacuum for 6 h at 60 °C.

The ration of the microstructure of the PHS unit and the degree of introduction of PAG group in the polymer was calculated from the 1H NMR peak area ratio using the following eq (1), and (2).

$$\frac{[\text{PHS unit}]}{([\text{PHS unit}] + [\text{TBA unit}])} = \frac{(\text{phenyl} / 4)}{[(\text{phenyl} / 4) + \{\text{alkyl} - (\text{phenyl} / 4) \times 3\} / 12]} \quad (1)$$

$$[\text{PAG unit}] = \text{PAG} / 18 \times [\text{PHS unit}] \quad (2)$$

The signals and their positions are as follows: 1H NMR: δ 8.19-7.39 (PAG), 7.20-6.06 (phenyl) and 2.05-0.0 (alkyl); ^{19}F $\{^1H\}$ NMR: δ -77.7 (CF_3).

2.4. Resist thin film coating on the silicon wafer

The resist solutions were filtered through a 0.22 μm PTFE syringe filter prior to spin-coating on silicon wafers which were treated by the adhesion process by HMDS. Spin-coating was performed at 3000 rpm for 30 s to form HMDS thin films on silicon wafers. Then these spin-coated films were prebaked at 130 °C for 90 s. Then, the solutions of sample #1 and 3 in PGMEA and sample #2 in γ -butyl lactone were spin-coated on the silicon wafer to prepare corresponding thin films. Spin-coating was performed at 2500 rpm for 45 s to form thin films on silicon wafers. Then these

spin-coated films were prebaked at 110 °C for 60 s. The resist thickness was measured by the optical-interference-type film thickness measurement tool (NanoSpec6100, NANO metrics Inc.).

The average film thickness and the degree of introduction (DI) of PAG (mol%) in each of the prepared samples show in Table 2.

Table 2. Summary of prepared resist samples.

Sample	Thickness (nm)	PAG structure	DI of PAG (mol%)	Resist type
1	43	PAG-1	2.2	Blend
2	22	PAG-2	5.2	Bound
3	41	-	0	Base Polymer

2.5. Contact angle measurement on the resist thin layer surface

The contact angle was measured by the sessile drop method. The measurement points on a 4 inch silicon wafer show in Fig. 1 (blue dot). Ultrapure water was used as a measurement solvent, and the liquid volume was 2.0 μl (the liquid diameter was calculated 1.6 mm when contact angle = 90 °). The $\theta/2$ method was used to calculate the contact angle. The droplet images were captured 10 s after dripping. The average value and standard deviation of the measured values at each distance (0, 20, 40 mm) from a wafer center were calculated and plotted.

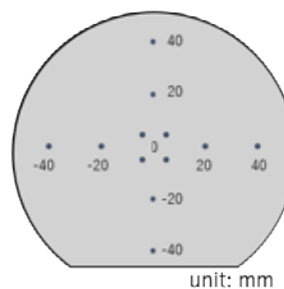


Fig. 1. Measurement points (blue dots) of the contact angle on a silicon wafer.

3. Results and discussion

3.1. Introduction of PAG-2 into base polymer

The reaction of PHS-TBA with PAG-2 was carried out using EDC·HCl as a condensation reagent under DMAP as a base catalyst at r.t. for 22 h, obtaining the polymer with $M_n = 4,500$ ($M_w/M_n = 1.88$) at 79% yield. The DI of PAG-2 as calculated by 1H NMR spectroscopy was found to be 5.2 mol%. Obtained polymer having PAG was

dissolved in γ -butyrolactone, THF, and DMSO. Thus, γ -butyrolactone was chosen as solvent for the preparation of resist thin film.

3.2. Dose estimation

Dose estimation of EUV resists were evaluated by sensitivity curves. Sample resists on Si wafer were exposed to EUV while changing exposure dose. After developing and rinse technique and measuring the thickness of the residual resist thin film, the sensitivity curve can be obtained. As a result, E_0 of PAG blend resist and bound one is smaller than 10 mJ/cm^2 . This result means these resists are highly sensitive resist for EUV. However, E_0 of bound resist is bigger than blend one. Thus, we evaluated that the contact angle for resist thin film surface. The base polymer used in CARs mainly has hydrophilic unit such as hydroxy groups and hydrophobic unit such as protecting group and PAG. Therefore, it was expected that the chemical composition distribution could be evaluated from the difference affinity (between hydrophobicity and hydrophilicity) by measuring the water-contact angle on the resist thin film surface.

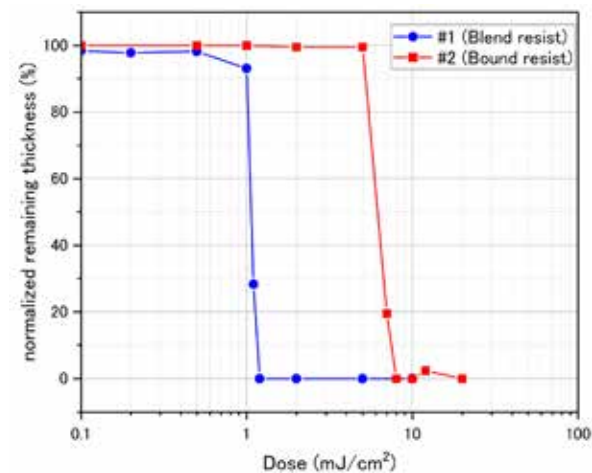


Fig. 2. Sensitivity curve of sample resists.

3.3. Contact angle measurement of sample resists

Figure 3 summarizes the results of contact angle measurement of samples #1-3. The horizontal and vertical axes show the distance from the center of silicon wafer and the contact angle of droplet, respectively. The contact angle of resist samples #1 (purple circle), and 2 (green circle) was approximately 82° in the vicinity of the wafer center. However, the contact angle of polymer sample #3 (black triangle) was approximately 80° . These results mean that resists are more hydrophobic than base polymer without PAG unit. It is considered that the reason of the increasing of hydrophobicity on the blend resist thin film is derived from PAG because PAG is without

hydroxy groups.

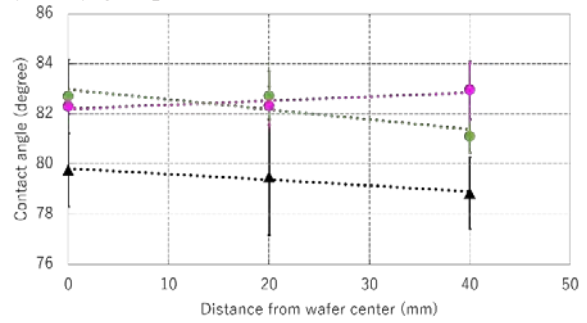


Fig. 3. Contact angle results of sample #1-3, blend resist (●), bound resist(●), and Polymer (▲).

Kawai *et al.* measured the refractive index and contact angle of resist thin films composed of novolak resin and naphthoquinone diazide after the spin coating, and it is reported that the refractive index and contact angle increase from the center to the outside of the silicon wafer [3]. The contact angle of the PAG blend resist increased from the center of the wafer to the outside in our results too. However, the result of PAG bound resist and polymer without PAG showed opposite behavior as shown Figure 3. This result means the type of resists affect the chemical composition distribution of the resist thin film surface. We consider that this difference affects EUV sensitivity.

4. Conclusion

We synthesized and characterized a new PAG bound resist. The obtained PAG bound resist showed good sensitivity for EUV. It is clarified that the resist thin film has different chemical composition distributions from the center to the outside of wafer depend of the type of resists.

References

- [1] T. Watanabe, Y. Fukushima, H. Shiotani, M. Hayakawa, S. Ogi, Y. Endo, T. Yamanaka, S. Yusa, and H. Kinoshita, *J. Photopolym. Sci. Technol.*, **19**, (2006), 521.
- [2] T. Watanabe, H. Kinoshita, N. Sakaya, T. Shoki, and S. Y. Lee, *Jpn. J. Appl. Phys.* **44**, (2005), 5556.
- [3]. K. Nagata, and A. Kawai, *J. Adhesion Soc. of Jpn (in Japanese)*, **31**, (1995), 187.

Relocation and Upgrade of Tender X-ray XAFS Beamline for High-Accuracy and Advanced Measurements

Koji Nakanishi

Laboratory of Advanced Science and Technology for Industry (LASTI), University of Hyogo

II

Abstract

In order to promote the use of industrial analysis, double crystal monochromator beamline BL05C is relocated and reconstructed. BL05C can use X-rays in the energy range of 1-3 keV and 5-12 keV. As an evaluation of 1-3 keV XAFS, the S K-edge XAFS measurements of FeS₂ were performed. As a result, the highly-accurate XAFS spectra can be obtained in a short time. In addition, *operando* XAFS experiments of amorphous Si thin film electrodes were performed as an advanced analysis technology. BL05C promotes the use of industrial analysis with highly accurate XAFS and original analysis technology.

1. Introduction

BL05, NewSUBARU was built in 2008 to promote industrial analysis, and has been used for this purpose. BL05 is consisted of two beamlines, BL05A and BL05B. BL05A is a beamline for soft X-ray XAFS, and the photon energy of 1-4 keV (so-called “tender X-rays”) are available. On the other hands, BL05B is a beamline for soft X-ray XAFS and PES measurements, and the photon energy of 0.05-1 keV are available. However, both beamlines had many problems and needed a major upgrade in order to further expand the industry analysis. One of the serious problems was the organic contamination of M₀ mirrors installed upstream of the beamline. A common mirror chamber was used for the M₀ mirrors of BL05A and BL05B. Because the mirror chamber was large and the performance of the vacuum pump was low, an ultra-high vacuum could not be maintained, resulting in severe organic contamination of both mirrors. Especially for BL05B, which measures carbon and oxygen, it was a fatal problem. In order to overcome these problems, we installed additional vacuum pumps as a partial solution. However, it was not possible to install a sufficient number of high-performance vacuum pumps due to the availability of empty ports, and a satisfactory degree of vacuum could not be obtained. There was also another problem with empty space around the mirror chamber. Therefore, as a drastic solution, we planned to separate BL05A and BL05B completely and prepare appropriate mirror chambers for each. The concrete method is to relocate BL05A beamline to BL06. The relocation of BL05A to BL06 was carried out from August 2020.

The results of the evaluation and measurement of the new beamline that was relocated and rebuilt while being upgraded are reported in this paper. Here, the location of it is BL06, but it will be called

“BL05C” because of the role it has played and the recognition of the beamline name.

2. Experimental details

All experiments were performed at the new beamline, BL05C. BL05C mainly consists of a collimating mirror, a Golovchenko-type double crystal monochromator (DCM), an X-ray intensity monitor (I₀ monitor), a measurement chamber, a load-lock chamber and various optical apertures and slits. A pair of InSb(111) monochromatizing crystals (2d = 7.481 Å) was used for Si K-edge and S K-edge XAFS measurements.

All samples were placed in a vacuum measurement chamber kept below 10⁻⁴ Pa. For anaerobic samples, a transfer vessel was used, which allows sample transport and introduction without exposure to the air.

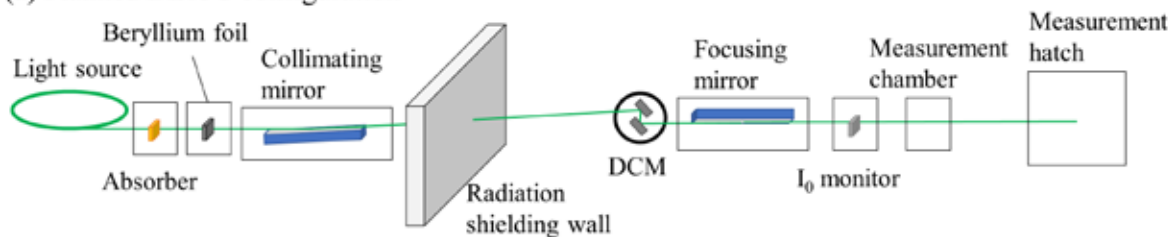
The total electron yield (TEY) with a sample drain current and partial fluorescence yield (PFY) with a silicon drift detector (SDD) and digital pulse processor were used for soft X-ray XAFS as standard detection methods. In the PFY mode, the typical peaking time of the SDD was 0.1 μs, and the dead time was kept below 2 %.

3. Results and discussion

3.1. Beamline configuration

The beamline configuration of BL05C is shown in Fig. 1. When BL05C was relocated, its beamline concept was changed. The beamline before relocation could use tender X-rays of 1-4 keV. In order to widely industrial demands, BL05C is changed the specifications of the X-ray mirrors. The former BL05A was used a nickel-coated toroidal mirror with an incident/reflection angle of 1.0 degrees, while the new BL05C is used a rhodium-coated parabolic mirror with an incident/reflection angle of 0.3 degrees. The comparison of the

(a) Planned BL05C configuration



(b) Present BL05C configuration (in 2021)

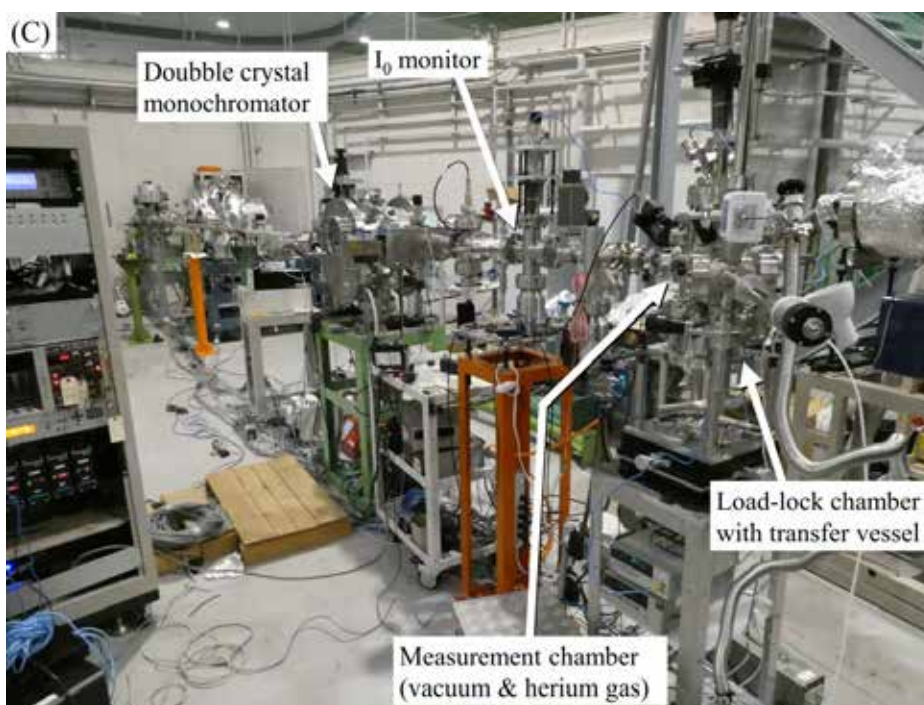
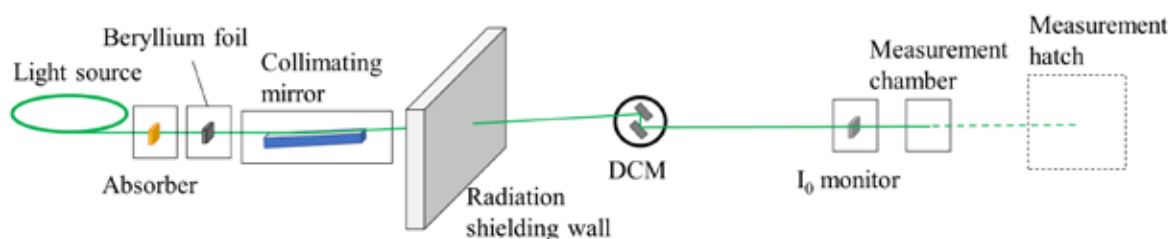


Fig. 1. Planned BL05C configuration (a), the present configuration (b) and the photograph (c).

reflectivity of each mirror is shown in fig. 2. Here, the RMS roughness value was poorly estimated and set to 3 nm. As a result, available photon energies in BL05C have been changed to 1-3 keV and 5-12 keV. This makes it possible to measure the K absorption edges of $3d$ transition metals and the L absorption edges of lanthanides, tungsten, gold, and platinum, which were previously impossible to measure with New Subaru. The above elements are the most in

demand in XAFS, making it possible to respond to a wide range of industrial analyses. As of 2021, only 1-3 keV is available because a focusing mirror and a measurement hatch for hard X-rays are not ready. Preparations for the use of hard X-rays are progressing steadily.

3.2. Evaluation of typical soft X-ray XAFS measurement (*ex situ* measurements)

FeS₂ is called “pyrite” in natural minerals and is well known for its similar appearance to gold. Although its industrial value has declined as it is no longer used as a raw material for sulfuric acid, it is considered promising as a next-generation high-capacity positive electrode active material for lithium-ion secondary batteries (LIBs) and as a material for thin-film solar cells, and its value has been reassessed in recent years.

FeS₂ powder was fixed on a carbon tape, and S K-edge XAFS measurements with simultaneous detection of the TEY and PFY were performed at BL05C (shown in Fig. 3). The dwell time was 2 seconds per point and the total acquisition time of the XAFS spectra in fig. 3 was approximately 25 minutes. Observed XAFS spectra have a very high S/N ratio. EXAFS oscillations over $k \sim 11 \text{ \AA}^{-1}$ have been obtained, and the peak derived from the second nearest neighbor is observed in the radial distance. These results indicate that the beamline performance is high enough for general industrial analysis.

Furthermore, a difference in XAFS spectra was observed between the TEY, which is surface-sensitive, and PFY, which is bulk-sensitive, due to the presence of sulfates on the FeS₂ powder surface.

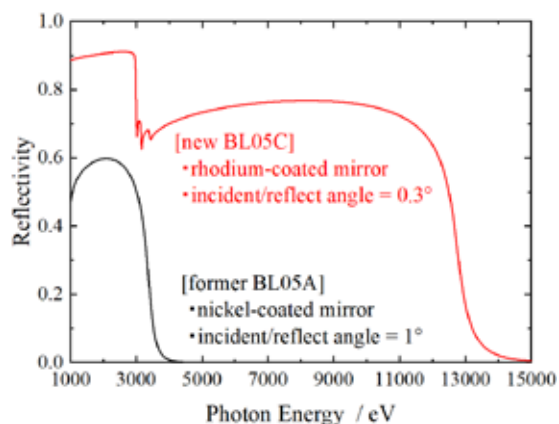


Fig. 2. Simulated reflectivity of former BL05A and new BL05C [1].

It was shown that this information on the difference in detection depth is also effective for industry analysis and can be fully utilized.

3.3. Operando soft X-ray XAFS measurement as advanced analysis

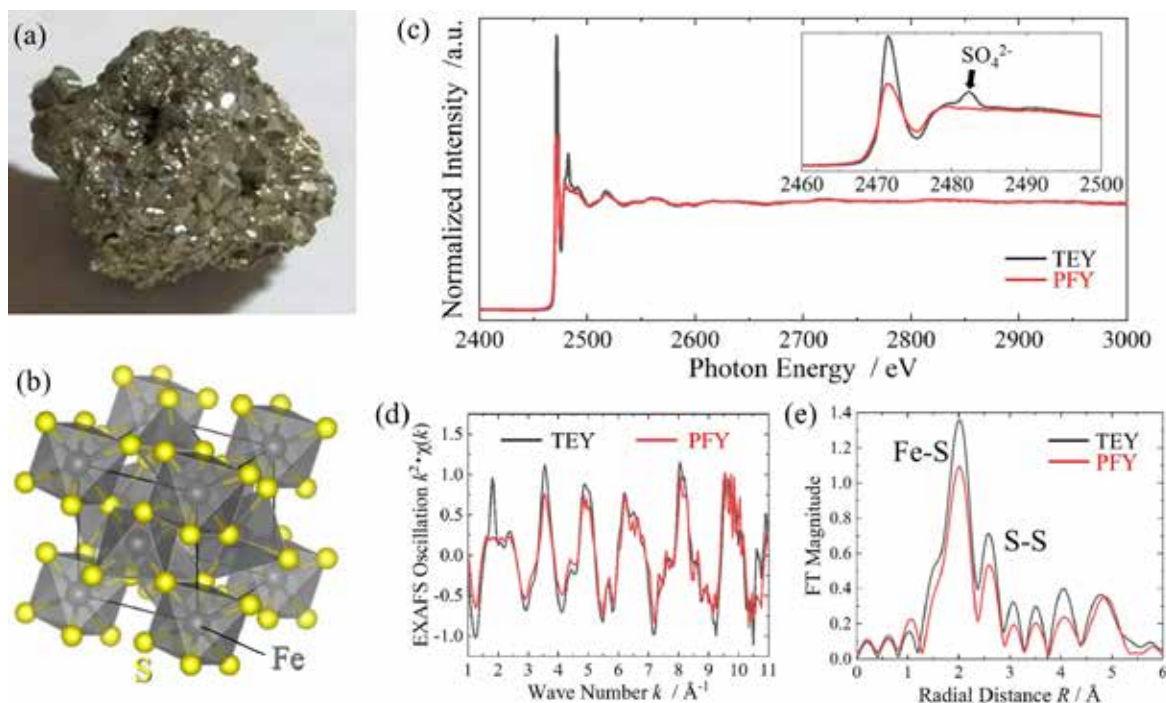


Fig. 3. XAFS spectra of FeS₂. (a) Photo of pyrite (Chemical formula: FeS₂). (b) Crystal structure of FeS₂. Observed XAFS spectra (c), EXAFS Oscillation $\chi(k)$ (d), and radial distance (e) with the TEY and PFY detection.

Silicon and silicon compounds are promising materials for high-capacity negative electrodes of next-generation LIBs. Si particles cannot withstand excessive expansion and contraction due to repeated charging and discharging, and physical destruction such as cracks and pulverization occurs in the active material [3], so the possibility of practical use is low. On the other hand, Si nanoparticles and thin films are less likely to cause this problem [4], so they have been used in many basic studies for the purpose of investigating the charge-discharge reaction of silicon. Silicon electrodes are expected to undergo alloying and dealloying reactions with lithium ions during charging and discharging. In this chemical reaction, the crystallinity of silicon is broken and it becomes amorphous, so it is difficult to analyze by XRD, which has been used several times in existing LIB electrode analysis. XPS is also difficult to analyze because an organic passivation layer called solid electrolyte interphase (SEI), which is a result of reductive decomposition of the electrolyte solution, deposits thickly on the silicon negative electrode. XAFS is very effective for the analysis of silicon and silicon compound negative electrodes, regardless of the crystallinity of the object to be analyzed and the ability to analyze deep areas of the sample. In addition, our group owns an originally-developed spectro-electrochemical cell for soft X-ray XAFS [2]. Therefore, it is possible to measure silicon and silicon compound negative electrodes during charge/discharge operation, which is difficult to perform at other facilities.

50 nm thick amorphous Si (a-Si) film electrode was prepared using DC magnetron sputter without air exposure, and the operando XAFS measurements were performed in BL05C. Observed XAFS spectra during first charge process are shown in Fig. 4. The initial XAFS spectrum is that of typical a-Si. As the charging progressed, the energy of the absorption edge shifted to the low energy side. This is attributed to the decrease in the oxidation number of Si due to the formation of the Li_xSi alloy. In addition, as the charge progressed, the small peak at 1841 eV in the initial spectrum disappeared and changed to a spectrum shape typical of metals.

In this way, BL05C enables us to observe non-equilibrium reactions of battery electrodes during device operation, which is useful for understanding true phenomena occurring in device samples.

4. Conclusion

In order to overcome the problems of the former BL05 and promote the use of industrial analysis, double crystal monochromator beamline BL05C is relocated and reconstructed. BL05C can use X-rays in the energy range of 1-3 keV and 5-12 keV. Soft X-ray XAFS of 1-3 keV was evaluated in this report. As a result, it became clear that it has high

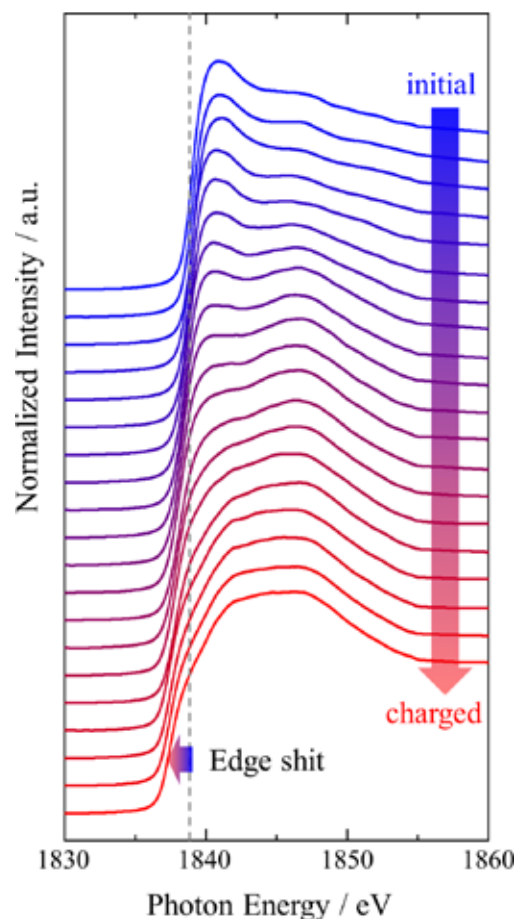


Fig. 4. operando Si K-edge XAFS spectra of a-Si thin film electrodes.

performance for XAFS. In addition, it became clear that the soft X-ray XAFS measurement during the operation of the independently developed storage battery is possible.

In the future, in addition to promoting the use of this beamline for industrial analysis, we will proceed with preparations for the setup of hard X-rays and proceed with the development of a beamline that is even more useful for industrial analysis.

References

- [1] B. L. Henke, E. M. Gullikson, J. C. Davis, *At. Data Nucl. Data Tables* **54**, (1993), 181.
- [2] K. Nakanishi, D. Kato, H. Arai, H. Tanida, T. Mori, Y. Orikasa, Y. Uchimoto, T. Ohta, Z. Ogumi, *Rev. Sci. Instrum.* **85**, (2014) 084103.
- [3] H. Wu, Y. Cui, *Nano Today* **7**, (2012), 414.
- [4] T. Jaumann, J. Balach, M. Klose, S. Oswald, U. Langklotz, A. Michaelis, J. Eckertab, L. Giebeler, *Phys. Chem. Chem. Phys.* **17**, (2015), 24956.

The Effect on Exit Beam Height by Change of Incident Beam Height in Symmetrical Layout Type Double Crystal Monochromator

Masato Okui^{1,2}, Naoki Yato¹, Atsushi Shimoguchi¹, Norio Murayama¹,
Ichiro Tsuboki¹, Kazuhiro Kanda²

¹Kohzu Precision Co., Ltd., ²LASTI, University of Hyogo

Abstract

A symmetrical layout type monochromator controlled by electronic cam was developed and its demonstration test was performed on BL06 in NewSUBARU. As the result of the demonstration test, the monochromator shows enough performance to new generation synchrotron facilities. In this report, when the height of incident beam is shifted from ideal height, suitable alignment method of this type of double crystal monochromator was examined by ray tracing and control algorithm. As the result, It is thought better by beam offset value of symmetrical layout type double crystal monochromator shall be changed is better than solution by the single axis alignment when the height of incident beam is changed.

1. Introduction

The authors have reported the result of experiment demonstrating of symmetrical layout type double crystal monochromator set temporarily on the beamline BL06 in New SUBARU in 2020 [1, 2]. This monochromator KOHZU NGM-RD1 is controlled by new developed control board with electronic cam technology [1, 2]. The monochromator has some features than previous monochromator [3] with mechanical cam. Firstly, the gravity center of the monochromator shall be kept on rotation axis on theta angle through all angles. Since 1st crystal and 2nd crystal is not combined mechanically by physical cam, it is easy to change beam offset between 1st crystal and 2nd crystal. I

In this report, the authors shall examine about alignment method of the symmetrical layout monochromator controlled by electronic cam in the case that height of actual incident beam is shifted from ideal beam position.

2. Experiments

2-1. Monochromator

The following Fig. 1 shows photograph of inside vacuum chamber of the NGM-RD1 type monochromator [1] and Fig.2 shows the schematic design drawing of the monochromator [1].

The Z_1 and Z_2 positions in each 1st crystal unit and 2nd crystal unit are controlled by the electronic cam board in real time corresponding with rotating Bragg angle value [1]. These positions are calculated by following equation (1) and (2) [1, 2]

$$Z_1(\theta) = \frac{h}{4} \left(\frac{1}{\cos \theta} - 1 \right) \quad (1)$$

$$Z_2(\theta) = -Z_1(\theta) \quad (2)$$

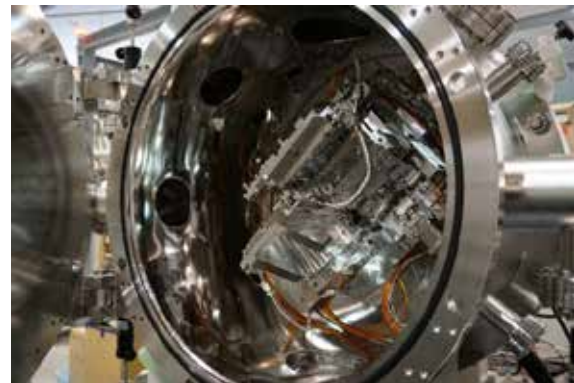


Fig. 1. Photograph of the inside vacuum chamber of NGM-RD1 type double crystal monochromator.

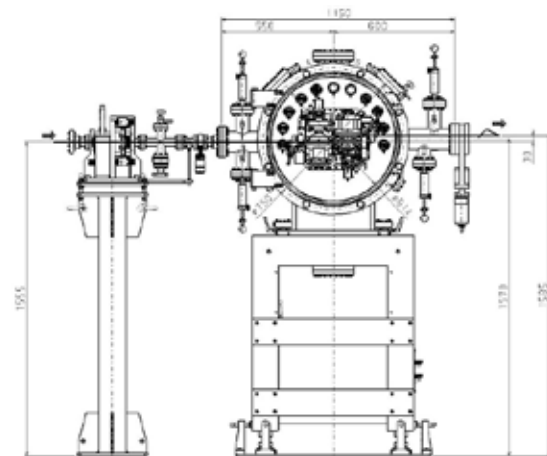


Fig. 2. Schematic design drawing of NGM-RD1 type double crystal monochromator.

In the Equation (1) and (2), θ shows Bragg angle, h shows the offset between the height of incident beam to the monochromator and the height of exit beam from it.

Okui *et al.* [1, 2] have already reported that the exit height from the monochromator have been able to keep constant by satisfied with Equations (1) and (2). In the above case, the exit height from the monochromator is kept the added beam offset on the incident beam height.

In NGM-RD1 type monochromator, the center point of footprint on 2nd crystal is moving to the upstream as Bragg angle is higher. In previous KOHZU KHL type monochromator in KEK-PF [3], long Y axis could be removed by moving footprint of only 2nd crystal, but the length of 2nd crystal is longer than the monochromators [4, 5] before KHL type.

In the present study, NGM-RD1 type monochromator, the center of footprint on 1st crystal is also moving to downstream as Bragg angle is higher [2] as well as 2nd crystal. This geometry causes the length of both 1st and 2nd crystals is shorter than the case of the previous geometry [3] since moving amount of footprint is divided to 1st and 2nd crystal.

2-2. Ray tracing

Ray tracing drawing in the case of ideal height of incident beam is shown as Fig. 3, when beam offset shall be 30 mm and Bragg angle shall be 30 degrees. The exit height from 2nd crystal is kept value add beam offset h to the height of ideal incident beam if satisfied with Equation (1) and (2) corresponding to any Bragg angle.

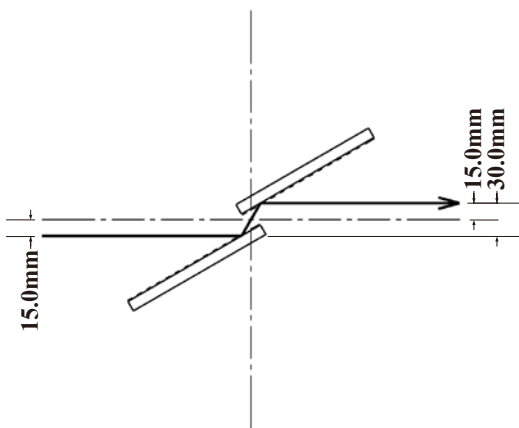


Fig. 3. Ray tracing drawing of NGM-RD1 type monochromator in the case of ideal height of the incident beam where the beam offset is 30 mm and Bragg angle is 30 degrees.

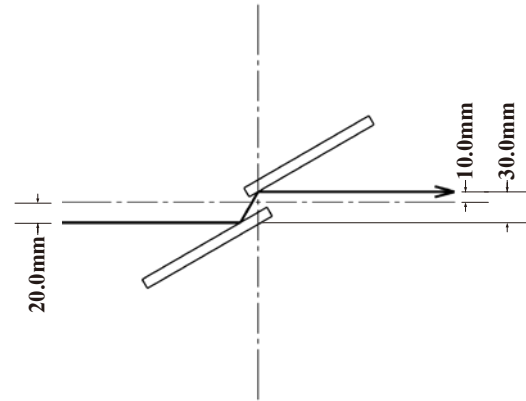


Fig. 4. Ray tracing drawing of NGM-RD1 type monochromator in the case of height of the incident beam down 5 mm from the ideal height where the beam offset is 30 mm and Bragg angle is 30 degrees.

If the height of incident beam would be down from the above ideal height, The exit height from 2nd crystal would be value add beam offset to the actual beam height and the height of exit in this case shall do down by same amount incident beam go down.

Fig 4 shows ray tracing drawing when the incident beam goes down 5 mm from ideal height, where the beam offset is 30 mm and Bragg angle is 30 degrees. The exit beam height goes down 5 mm from Fig. 3 that is the case of ideal incident beam.

3. Results and Discussions

As describing the above section, the actual exit beam height would be synchronized change with the actual incident beam height in this symmetrical layout double crystal monochromator controlled by electronic cam.

This situation is leads by that only beam offset between 1st and 2nd crystal of the layout is considered in Equation (1) used in this electronic cam control system. Firstly, beam stability should be kept in the upstream like front end, but it shall be difficult that perfectly fixed incident beam could not be supplied from the upstream of double crystal monochromator.

Thereat, the authors would like to propose solution by additional control as to cancel the incident beam vibration to electronic cam control algorithm in this report. We can suggest the change of exit beam height from the monochromator shall be able to cancel by that

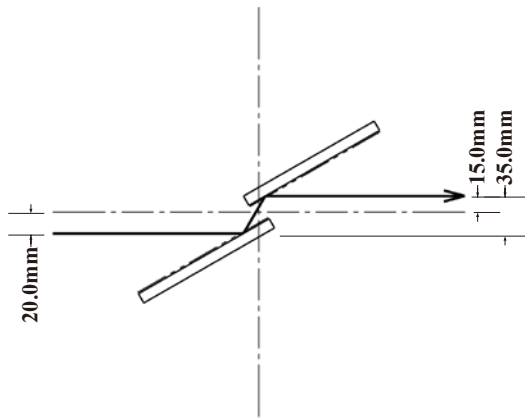


Fig. 5. Ray tracing drawing of NZD-RD1 type monochromator after beam offset adjusted to fix exit position when the incident beam goes down 5 mm from ideal height, where Bragg angle is 30 degrees and beam offset is 35 mm.

beam offset would be adjust, since the change of the exit beam height is caused by actual change of incident beam height. Fig. 5 shows our concept of method adjusting fixed beam position, where Bragg angle is 30 degrees.

In Fig. 5, $Z1$ and $Z2$ are moved far as to keep its beam offset is 35 mm from 30 mm respectively. As the result, the beam offset between 1st crystal and 2nd crystal shall be wide than the case of ideal incident beam height but the actual exit beam position from the ground shall be kept with the exit ideal beam position from the ground.

At this this time, In Equation (1), only beam offset between 1st crystal and 2nd crystal should be changed so that $Z1$ and $Z2$ are symmetrical movement for keeping gravity point of the monochromator. When amount of changing incident beam height is Δh , $Z1$ position adjusted considering incident beam vibration is expressed the following Equation (3)

$$Z_1(\theta) = \frac{h+\Delta h}{4} \left(\frac{1}{\cos \theta} - 1 \right) \quad (3)$$

If the adjustment of the monochromator was be done by only either $Z1$ or $Z2$ to keep exit beam position from ground, functions of $Z1$ and $Z2$, especially concerned with velocities, are different each other and complex. The difference will cause the real-time control on electronic cam board would be difficult. By the above the authors recommend adjusted control according to Equation (3). After this adjustment positional moving range of footprint of beam shall change from the range of the case of ideal height of

incident beam. Thus, it is necessary that the enough length of 1st and 2nd crystal should be allowed for not cutting footprint.

4. Conclusion

From result of ray tracing and easiness of controlled electronic cam, adjustment by beam offset value of symmetrical layout type double crystal monochromator shall be changed is better than solution by the single axis alignment when the height of incident beam is changed.

Acknowledgement

The authors thank deeply for significant advice by Miss. Naoko Sawada, Technical division, Kohzu Precision Co., Ltd.

References

- [1] Okui *et al.*, *LASTI Annual Report* **21**, (2019) 33.
- [2] Okui *et al.*, *J. Phys.: Conf. Series* (accepted).
- [3] Kawata *et al.*, *AIP Conf. Proc.*, **705**, (2004) 663.
- [4] Matsushita *et al.*, *Nucl. Instrum. Methods*, **A246**, (1986) 377.
- [5] Yabashi *et al.*, *Proc. SPIE*, **3773**, (1999), 2.

Structural Changes of Highly Hydrogenated Diamond-Like Carbon Films by Soft X-Ray Irradiation

Daisuke Niwa¹, Tomohiro Mishima¹, Hibiki Terai¹, Koji Nakanishi¹, Masahito Niibe¹,
Kazuhiro Kanda¹, Fuminobu Hori², Atsushi Yabuuchi³, Atsushi Kinomura³
¹LASTI, Univ. Hyogo, ²Eng., Osaka Pref., Univ., ³RNS, Kyoto Univ.

Abstract

Highly hydrogenated diamond-like carbon (DLC) films have characteristics of low friction coefficient in a vacuum and they are expected to be applied as solid lubricants for devices used in space. However, it is known that hydrogen desorbs from highly hydrogenated DLC films by soft X-ray irradiation. In this report, the hydrogen desorption process and structural change of highly hydrogenated DLC films by soft X-ray irradiation was discussed by observing free volume in the DLC films by the measurement of positron annihilation spectroscopy (PAS) using slow positron beams.

1. Introduction

Diamond-like carbon (DLC) films are amorphous carbon films composed of hydrogen, sp^2 hybridized carbon (graphite structure), sp^3 hybridized carbon (diamond structure), and free volume [1]. DLC films have various excellent properties such as high hardness, low friction, gas barrier, abrasion resistance, chemical stability, surface smoothness, and high X-ray resistance. Therefore, DLC films are applied in a wide range of industrial fields such as coating materials and lubricants.

DLC films with high hydrogen content are called highly hydrogenated DLC films. Highly hydrogenated DLC films have characteristics of ultra-low friction coefficient in a vacuum. Therefore, they are expected to be applied as solid lubricants for devices used in space such as artificial satellites and probes. It is very important to understand the effect of soft X-rays on highly hydrogenated DLC films to apply highly hydrogenated DLC films to the space industry. Previous studies in our laboratory have shown that soft X-ray irradiation against the highly hydrogenated DLC films causes hydrogen desorption, carbon recombination, and an increase in density [3]. In this work, change of free volume in the highly hydrogenated DLC films was observed through positron annihilation spectroscopy (PAS) using slow positron beams, and the hydrogen desorption process from highly hydrogenated DLC films by soft X-ray irradiation was discussed.

2. Experimental

The highly hydrogenated DLC films are deposited on a Si substrate by plasma enhanced

CVD method. Film thickness was 400 nm, and the hydrogen content in the films was about 50 %. Soft X-ray white light was irradiated to the highly hydrogenated DLC films at BL-6 of the NewSUBARU [4]. The white radiation beam from a bending magnet was introduced to the sample stage using a pair of mirrors, whose incident angle was 3°. The electron energy of the NewSUBARU ring was 1.0 GeV and the SR at the BL-6 sample stage had a continuous spectrum from IR to soft X-ray, which was lower than 1 keV. The typical ring current was 300 mA during the exposure. The SR dose [mA·h] was represented by the product of the ring current [mA] with the exposure time [h]. The irradiation doses of the sample prepared in this experiment are 0 mA·h, 500 mA·h, 1000 mA·h, and 4000 mA·h.

The measurement of positron annihilation spectroscopy (PAS) was carried out using slow positron beam equipment installed in the B-1 experimental hole of the Kyoto University Research Reactor (KUR). In the B-1 experimental hole, positrons are extracted from the reactor at 10 eV and accelerated up to 30 keV just before injection into the material. PAS is a method to obtain information on the free volume by observing γ -rays generated from the annihilation of a positron injected from the reactor and an electron in the material. In the present work, two types of measurements; the positron annihilation lifetime spectroscopy and the Doppler broadening were carried out. The process of annihilation in the material is illustrated in Fig. 1. The positron injected into the material loses energy as a result of Coulomb repulsion from the positive charge of the ion core in the atom, and is trapped in the free volume. The trapped positron in the

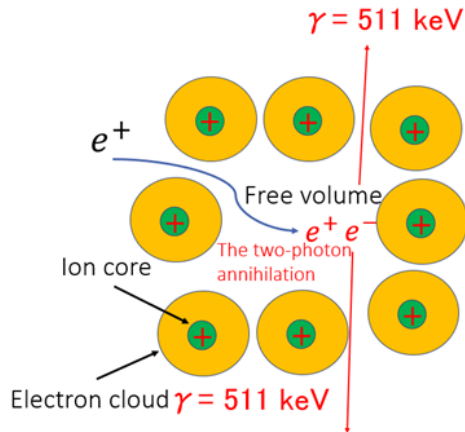


Fig. 1. Positron annihilation and γ -ray generation process

free volume annihilates with an electron, in the free volume and two γ -rays of 511 keV are emitted. In the positron annihilation lifetime spectroscopy, a pulsed positron beam was used to measure the positron annihilation lifetime (PALT) from the decay profile of γ -rays generated by annihilation. When the size of the free volume is small, the electron density is large. Therefore, positrons easily collide with electrons, and PALT is shortened. On the contrary, when the size of the free volume is large, the electron density in the free volume is small. As a result, PALT becomes longer.

In the Doppler broadening method, the energy broadening of γ -rays generated in annihilation is measured. The energy of γ -rays generated in annihilation is the sum of the mass-energy of 511 keV. Positrons trapped in free volume due to Coulomb repulsion have thermal energy. Therefore, momentum to cause the Doppler broadening of γ -rays comes from electrons. Because valence electrons have low momentum, the Doppler broadening effect is small, as a result, the emitted γ -rays are observed in the energy range around 511 keV. On the other hand, because core electrons have high momentum, the energy dispersion due to the Doppler effect is large, as a result, γ -ray is observed in a wide range from 511 keV. The S parameter is defined as a ratio of counts in the central channels to the total peak amplitude. The increase or decrease of the S parameter corresponds to the increase or decrease of the ratio of valence electrons in the free volume.

3. Results

Figure 2 shows the incident positron energy dependence of the S parameter of highly hydrogenated DLC films and a Si substrate. The detection depth changes depending on the energy of the incident positron. In the energy range higher

than 10 keV, the S parameters are mostly constant and show almost the same values as those of the Si substrate. As a result, the S parameter in this energy range is considered to obtain from the Si substrate. The S parameter in the energy range of about 1 keV to 2.5 keV can be obtained from the DLC films. The S parameters of the DLC films are in the range of 0.47 to 0.49. The S parameter decreases with increasing of a soft X-ray dose.

Figure 3 shows the soft X-ray irradiation dose dependence of PALT and the S parameter of the highly hydrogenated DLC films. The X-axis shows the soft X-ray irradiation dose. The left-side Y-axis shows the PALT represented by a black dot, and the right-side Y-axis shows the S parameter represented by a red dot. In general crystals, the PALT increases with the size of the free volume because the positrons and surrounding electrons are less likely to annihilate each other. Similarly, the S parameter increases with the size of free volume, because the fraction of valence electrons in the free volume increases [5]. However, in the present work, as shown in Fig. 3, the PALT increases but the S parameter decreases with increasing the irradiation dose.

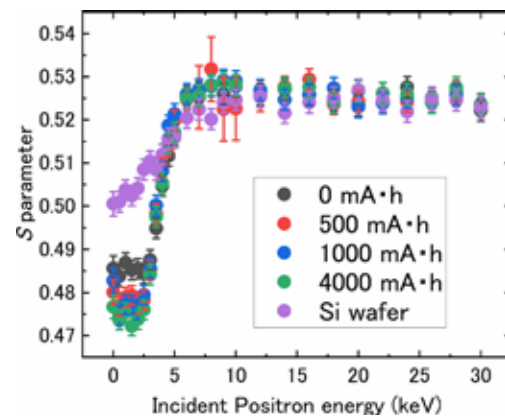


Fig. 2. Incident positron energy dependence of the S parameter.

It was reported that hydrogen is desorbed and carbon is recombined by the irradiation of soft X-rays to the highly hydrogenated DLC films [3]. The free volume in the films is considered to increase because the PALT increased. On the other hand, the decrease in the S parameter is attributable to decrease in the density of valence electron in the free volume. Carbon has core and valence electron, while hydrogen has no core electron but only valence electron. It is considered

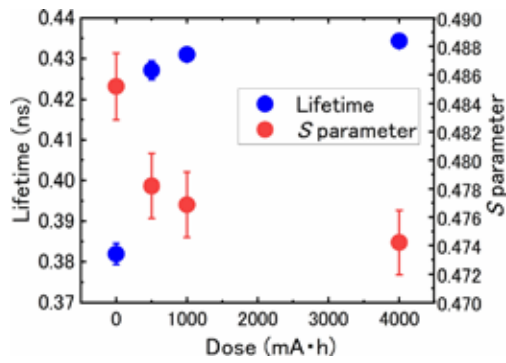


Fig. 3. Soft X-ray dose dependence of positron annihilation lifetime and S parameter

that the S parameter is decreased because the fraction of valence electron in the free volume is decreased due to desorption of hydrogen.

As described above, this study shows that soft X-ray irradiation on highly hydrogenated DLC films decreases the S parameter and increases PALT. This can be interpreted as follows: soft X-ray irradiation causes desorption of hydrogen from the highly hydrogenated DLC film, resulting in the recombination of carbon, which increases the density. But in the free volume increases, and the atoms surrounding the free volume change from hydrogen to carbon.

References

- [1] A. C. Ferrari, J. Robertson, *Phys. Rev. B* **63**, (1993) 1771.
- [2] D. C. Lugo, P. C. Silva, M. A. Ramirez, E. J. D. M. Pillaca, C. L. Rodrigues, N. K. Fukumasu, E. J. Corat, M.H. Tabacniks, V. J. Trava-Airoldia, *Surf. Coat. Tech.*, 332, (2017) 135.
- [3] R. Imai, A. Fujimoto, M. Okada, S. Matsui, T. Yokogawa, E. Miura, T. Yamasaki, T. Suzuki, K. Kanda, *Diam. Relat. Mater.*, **44**, (2014) 8.
- [4] K. Kanda, T. Ideta, Y. Haruyama, H. Ishigaki, S. Matsui, *Jpn. J. Appl. Phys.* **42**, (2003) 3983.
- [5] A. Uedono, R. Suzuki, S. Tanigawa, *Radioisotopes* **41**, (1992) 611.

Development of an Improved Multi-Layer Mirror for the New γ -Beam Source via X-Ray Compton Scattering

Norihito Muramatsu¹, Tetsuo Harada², Schin Daté³, Kazuhiro Kanda², Manabu Miyabe¹, Shuji Miyamoto², Haruo Ohkuma^{3,4}, Masahiro Okabe¹, Hajime Shimizu¹, Shinsuke Suzuki³, Atsushi Tokiyasu¹, Takeo Watanabe²
¹ELPH, Tohoku University, ²LASTI, University of Hyogo, ³RCNP, Osaka University,
⁴Aichi Synchrotron Radiation Center

II

Abstract

We are developing new techniques to produce a high energy γ -beam via Compton scattering of soft X-rays from 1 or 1.5 GeV electrons at NewSUBARU. The X-rays of 92 eV are obtained from the short undulator at BL07A and reflected backwardly into the storage ring by using a Mo/Si multi-layer mirror. We developed an improved multi-layer mirror for better surface condition and heat load. The new mirror shows a reflectance of 65.8% in a test at BL10.

1. Introduction

We are developing a new method to produce a GeV γ -beam by the Compton scattering of X-rays at an electron storage ring. In our project [1], soft X-rays of 92 eV are obtained from a short undulator (total length = 2.28 m and period length = 7.6 cm) which is located at BL07 of NewSUBARU. These X-rays are reflected to the backward direction at a Mo/Si multi-layer mirror and injected into the storage ring. In such a procedure, the maximum energy of a γ -beam produced via Compton scattering reaches 0.58 and 1.02 GeV for the electron beam energy of 1 and 1.5 GeV, respectively. The achievable energies are much higher than that of laser Compton scattering.

We have installed a large vacuum chamber at BL07A [2] to set up the Mo/Si multi-layer mirror with a water-cooled copper holder and stepping-motor stages. An X-ray wire scanner (a profile and intensity monitor) and gamma detectors (a PWO electromagnetic calorimeter, a beam profile monitor, and a rate monitor) have also been installed into BL07A, and their performance has been tested as described in Ref. [3]. Currently, an improvement of the Mo/Si multi-layer mirror is being made based on the feedback from several tests using a prototype [4]. This report shows results of property tests for a newly produced multi-layer mirror.

2. Development of an improved mirror

A prototype of the Mo/Si multi-layer mirror was made by using a substrate of a low thermal expansion glass ceramic (Zerodur) and coating Mo and Si layers with 50 periodic repetitions. Its reflective surface is cylindrically polished to make a focus on the electron beam at the 16.7 m upstream straight section of the storage ring. This cylindrical surface was made by bending the substrate with application of stress at two edges,

then polishing a surface flatly, and finally releasing the stress [3]. However, the curvature radius of the obtained cylindrical surface was measured to be 14.4 m by an ultrahigh accurate 3D profilometer [4]. There was room to improve a surface accuracy. In addition, the RMS value of surface roughness was measured to be 0.99 nm in $2 \times 2 \mu\text{m}^2$ by using an atomic force microscope (AFM) [4]. It was not very good compared with the reflecting wavelength of 13.5 nm.

In Ref. [4], we also tested temperature rise on the multi-layer mirror surface by irradiating undulator X-rays at BL07A. The maximum temperature reached 190°C in the measurement using a radiation thermometer. It turned out that heat conductance from the mirror to the water-cooled holder was bad in a vacuum. This may possibly cause a distortion of the mirror surface and lower the ability of reflected X-ray focusing.

Thus, we have newly produced a new mirror with a Silicon substrate, which has an area of $50 \times 50 \text{ mm}^2$ and a thickness of 16 mm. The reflective surface was polished in the cylindrical shape with a curvature radius of 16.7 m by applying magneto-rheological finishing. Heat conductance to the mirror holder must be improved by removing a spacer plate and putting a thin Indium sheet to the gap.

The surface condition of this new mirror was examined in a way similar to the case of the old mirror. The RMS value of surface roughness was improved to 0.2 nm in an area of $80 \times 80 \mu\text{m}^2$. The surface accuracy was also excellent, showing that the deviation from the designed cylindrical shape was within 134 nm in an effective area of $45 \times 45 \text{ mm}^2$. Fifty periodic layers of Mo and Si were finally made on the reflective surface.

The performance of the produced mirror was tested at BL10. Figure 1 shows the reflectance of X-rays around the energy of 92 eV. Different

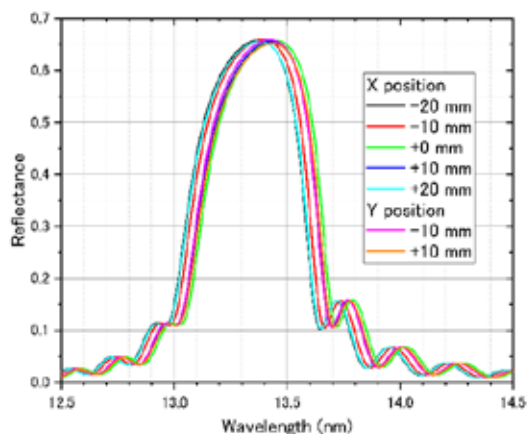


Fig. 1. Reflectance of a developed Mo/Si multi-layer mirror with a Silicon substrate.

colored lines indicate the reflectance values at seven incident points on the mirror. The maximum reflectance was 65.8% in the case of injection at the center. This value was close to the design, and higher than the reflectance of the old mirror (54.2%). A diffusion component of the reflected X-rays was also confirmed to be small enough in the case of the new mirror.

3. Prospect of our project

We will install the developed new mirror into the vacuum chamber at BL07A in FY2022. After several tests of heat conductance and X-ray reflection, we are going to demonstrate the production of a high energy γ -beam via Compton scattering of soft X-rays from electrons in the storage ring. Our development of a new γ -beam source will be helpful for next-generation researches of hadron photoproduction experiments.

Acknowledgments

This research is supported in part by Grant-in-Aid for Challenging Research (Pioneering) No. 18H05325 / 20K20344, Scientific Research (B) No. 22H01225, and Challenging Research (Exploratory) No. 22K18707.

References

- [1] <http://www.rcnp.osaka-u.ac.jp/~mura/kaitaku/>
- [2] S. Tanaka, S. Suzuki, T. Mishima, K. Kanda, *J. Synchrotron Rad.* **28**, (2021) 618.
- [3] N. Muramatsu et al., *J. Particle Accelerator Society of Japan* **Vol.16** No.3, (2019) 154.
- [4] N. Muramatsu et al., *LASTI Annual Report* **22** (2020), 29.

Reduction of Graphene Oxide by Combination of Atomic Hydrogen Annealing and Soft X-Ray Irradiation

Akira Heya¹, Akinori Fujibuchi¹, Masahiro Hirata¹, Kazuhiro Kanda², and Koji Sumitomo¹

¹University of Hyogo, ²LASTI, University of Hyogo

Abstract

The reduction of graphene oxide (GO) by atomic hydrogen annealing (AHA) and soft X-ray irradiation was investigated using microwell substrates with μm -sized holes with and without Ni underlayers. The GO film was reduced by AHA at 170 °C. In addition, the GO was also reduced by soft X-ray irradiation at 150 °C. The effect of Ni underlayer on GO reduction differed between AHA and soft X-ray irradiation. Furthermore, combinations of soft X-ray irradiation and AHA were also investigated. The order of treatment was found to affect the properties of the reduced GO films.

1. Introduction

Graphene and graphene oxide (GO) have been widely investigated for transparent conductive films, sensors, and other applications. The GO is a common precursor material for graphene because individual GO sheets are easily obtained by oxidizing graphite, permitting GO films to then be formed by solution processing. To obtain graphene (reduced GO (r-GO)) from GO, the GO film is reduced by various post-treatment methods such as thermal treatment above 1000 °C, hydrazine treatment, and ultra-violet irradiation.

To improve the sensitivity of sensors using r-GO films, the initial properties of these films are finely controlled by the reduction process. The sensors using suspended graphene such as pressure sensors, microphones, ultrasound detectors, and accelerometers have been developed. A highly-controlled reduction of the suspended GO is expected to enhance the electrical characteristics of graphene sensors.

We have investigated a novel surface treatment, named atomic hydrogen annealing (AHA) for GO reduction [1]. Graphene on Ni thin films was also synthesized from pentacene molecules ($\text{C}_{22}\text{H}_{14}$) using a high-density soft X-ray undulator source at a synchrotron facility [2]. In this study, effect of soft X-ray irradiation on reduction of GO by AHA was investigated using microwell substrate with μm sized holes and with and without Ni underlayer.

2. Experimental

Individual GO sheets were prepared from synthetic graphite flakes (flake size $\sim 100 \mu\text{m}$) based on Brodie's method. Details are indicated in Ref. 1. A $5 \times 5 \text{ mm}^2$ array of circular wells with diameters of 1, 2, 4, and $8 \mu\text{m}$, named MW substrate, was fabricated on a $\text{SiO}_2(120 \text{ nm})/\text{c-Si}$ substrate by photolithography and reactive ion etching. The Ni film with 50 nm in thickness was deposited on some

MW substrate by vacuum evaporation. The GO dispersed in 0.1 ml of solvent (0.175 mg/ml) was dropped onto cleaned MW and Ni/NW substrates on a hot plate at 150 °C.

The AHA apparatus is shown in elsewhere [2]. A $55 \times 55 \text{ mm}^2$ W mesh with a wire diameter of 0.03 mm and having 50 holes/inch was used as a catalyst for H_2 decomposition. The flow rate of H_2 and gas pressure were 150 sccm and 30 Pa, respectively. The W mesh temperature and treatment time were 1700 °C and 3600 s, respectively. The distance between the W mesh and the sample was 80 mm. In AHA, the sample temperature was automatically increased by thermal radiation from the heated W mesh. The sample temperature was measured by a K-type thermocouple in contact with the Si substrate and was 170 °C.

The irradiation of soft X-rays was carried out at BL07A of NewSUBARU. Schematic diagram of soft X-ray irradiation apparatus is shown elsewhere [2]. The light source of BL07A was a 2.28 m undulator. The storage-ring energy was 1 GeV during this experiment. The undulator gap was 55.5 mm. The main photon energy was 300 eV. A monochromator was not used to select the main photon energy. Hence, the irradiated light also contains other higher-order X-rays. The irradiation time was 1 hour. The storage-ring current and dose were 350 mA and 350 mA·h, respectively. The saturated sample temperature during irradiation was 150 °C.

The property of GO film was evaluated by X-ray photoelectron spectroscopy (XPS). Al monochromatized X-ray source (1486.60 eV) was used. The diameter of X-ray beam was $100 \mu\text{m}\phi$. A neutralizer gun was used to suppress the charge. Unfortunately, the XPS probing size is larger than the well diameter, so it was not possible to measure the suspended and supported regions separately.

3. Results and discussion

The C 1s and O 1s XPS spectra of the GO/MW and GO/Ni/MW substrates before and after various treatments are shown in Fig. 1. The C 1s spectrum of GO consists of 5 peaks, C-C (284.6 eV), C-OH (285.5 eV), C-O-C (286.6 eV), C=O (287.5 eV) and O=C-OH (288.9 eV) [3]. The O 1s spectrum of GO consists of 3 peaks, C=O (531.1 eV), C-O (532.0 eV), and C-OH (533.4 eV) [4]. Although the peaks corresponding to chemical bonds between C and O were observed before post-treatment, these peaks were reduced by AHA and soft X-ray irradiation.

For GO/SiO₂/Si substrates, C-O related peaks remained after soft X-ray irradiation compared to AHA irradiation. The O 1s spectra indicated that soft X-ray irradiation reduced the GO film but also destroyed the six-membered ring structures. When AHA was followed by soft X-ray irradiation, the C-O related peaks increased after soft X-ray irradiation. This may be due to the formation of defects in the r-GO after AHA by soft X-ray irradiation, which reacted with oxygen after air exposure, resulting in an increase in C-O related peaks. The condition of soft X-ray irradiation followed by AHA was expected to promote the most reduction of GO, but the reduction is less than that of AHA, indicating that the six-membered ring breakdown caused by soft X-ray irradiation is not fully repaired by AHA. However, the combination

of soft X-ray irradiation and AHA is expected as a fine turning for surface state of r-GO.

For GO/Ni/SiO₂/Si substrate, no degradation due to soft X-ray irradiation was observed in both C 1s and O 1s spectra with AHA and soft X-ray irradiation. It is considered that the Ni underlayer suppressed the destruction of six-membered ring structure and/or had effect of repair. The peak due to O=C-OH increased under condition of AHA followed by soft X-ray irradiation. The peak of Na KLL was observed in O 1s spectrum. The origin of Na is considered to be residues from the GO formation process. The peak due to O=C-OH increased under condition of AHA followed by soft X-ray irradiation.

The influence of Ni underlayer on GO reduction by AHA and soft X-ray irradiation is discussed. The results showed that the activity of reduction on the Ni surface was weaker than that on the SiO₂ surface. The reduction was suppressed by the Ni underlayer because of a decrease in the effective atomic hydrogen density on the surface of the GO film due to the incorporation of atomic hydrogen in the Ni underlayer. On the other hand, it was considered that the effect of Ni underlayer on GO reduction during soft X-ray irradiation was enhanced by electrons generated by soft X-ray excitation.

Conclusion

AHA and soft X-ray irradiation reduced GO film at low temperatures. For the GO/SiO₂/Si substrate, reduction activity of AHA was higher than soft X-ray irradiation. In AHA, the Ni underlayer suppressed GO reduction due to decrease in the effective atomic hydrogen density on the GO film. In contrast, with soft X-ray irradiation, the Ni underlayer suppressed the destruction of six-membered ring structure. The order of treatment affected the property of r-GO films.

References

- [1] A. Heya, N. Matsuo, *Jpn. J. Appl. Phys.* **57**, (2018), 04FL03.
- [2] A. Heya, T. Oonuki, R. Utimi, K. Kanda, R. Yamasaki, K. Sumitomo, *Thin Solid Films* **713**, (2020), 138365.
- [3] O.-K. Park, M. G. Hahm, S. Lee, H.-I. Joh, S.-I. Na, R. Vajtai, J. H. Lee, B.-C. Ku, and P. M. Ajayan, *Nano Lett.* **12**, (2012), 1789.
- [4] A. Ganguly, S. Sharma, P. Papakonstantinou, J. Hamilton, *J. Phys. Chem. C* **115**, (2011), 17009.

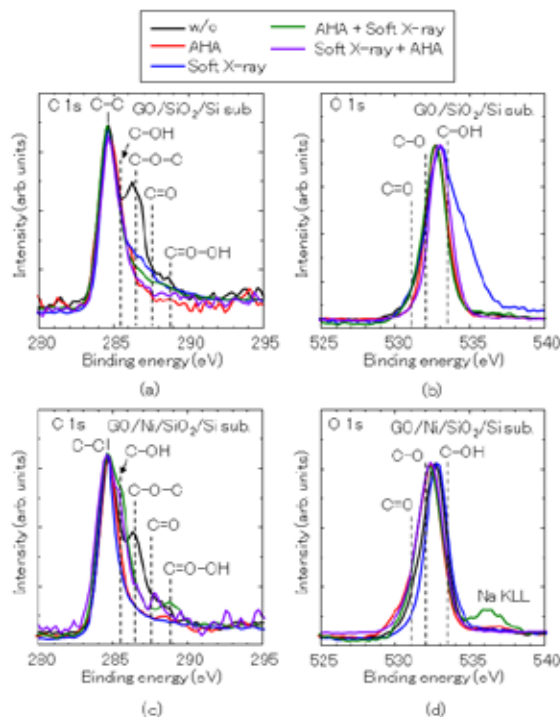


Fig. 1. C 1s and O 1s XPS spectra of the GO/MW and GO/Ni/MW substrates with various treatments. (a) C 1s and (b) O 1s of the GO/SiO₂/Si substrate. (c) C 1s and (d) O 1s of the GO/Ni/SiO₂/Si substrate.

PES and XAS Study of the Effect of Atomic Hydrogen Annealing Treatment for Conductive Thin Film Sb-SnO₂

Takeshi Fukuda¹, Akira Heya¹, Takanori Yamamoto¹, Ryuki Tsuji¹, Yuichi Haruyama², Masahito Niibe², Satoru Suzuki², Seigo Ito¹

¹Department of Materials and Synchrotron Radiation Engineering, Graduate School of Engineering, University of Hyogo, 2167 Shosha, Himeji, Hyogo 671-2280, Japan.

²Laboratory of Advanced Science and Technology for Industry, University of Hyogo, 3-1-2 Kouto, Aka, Hyogo 678-1205, Japan.

Abstract

Antimony-doped tin oxide (Sb-SnO₂) was synthesized via ozone and autoclave procedures. Hydrogen treatment on the spin-coated Sb-SnO₂ thin film significantly improved the electrical conductivity. Photoemission electron spectroscopy (PES) and X-ray absorption spectroscopy (XAS) measurements for valence band and conduction band analysis were performed with/without atomic hydrogen annealing (AHA) treatment on the thin films, in order to clarify the reason for this improvement. The results showed that the oxygen in SnO₂ was reduced by the hydrogen treatment.

1. Introduction

Conductive metal oxide nanoparticles have been applied in various fields such as fuel cell catalysts, solar cells, and displays as materials showing high electrical conductivity. Tin-doped indium oxide (ITO), which is currently the mainstream material, is expected to be developed as an alternative due to the high cost of indium. Since SnO₂ is a metal oxide with large reserves and is thermally and chemically stable, there has been much research on improving its electrical conductivity. In this study, antimony-doped tin oxide (Sb-SnO₂) was synthesized by an ozone-based method [1] with autoclave treatment. Hydrogen-treatment effect on spin-coated Sb-SnO₂ thin films was investigated to further improve conductivity.

2. Experiments

2.1. Fabrication method of Sb-SnO₂ nanoparticle

The fabrication method of Sb-SnO₂ is shown in Figure 1a. First, only 0.005 mol of tin bifluoride (SnF₂) or doping materials were

dissolved in 95 mL of distilled water at a mol ratio of 95:5. The doping materials used was SbCl₅. Next, 5 mL of tetramethylammonium hydroxide (TMAH) was added. The solution was stirred at 850 rpm with a magnetic stirrer while ozone was generated by an ozone generator and bubbled for 6 h at a flow rate of 0.3 L/min. Afterwards, the precipitates were washed by centrifugation using 2-propanol (IPA) and distilled water. Finally, the precipitate was dispersed in 5 mL of distilled water.

2.2. Fabrication method of Sb-SnO₂ thin film

Figure 1b shows how the thin films were fabricated. First, glass plates cut to 25 × 25 mm were placed in a container containing liquid detergent and distilled water and sonicated for 15 min. Next, the glass plates were rinsed with distilled water and ethanol, and then placed in a container containing ethanol and sonicated for 15 min. After washing, the glass plates were allowed to dry naturally, and UV-O₃ cleaner was used to remove organic matter from the surface. The

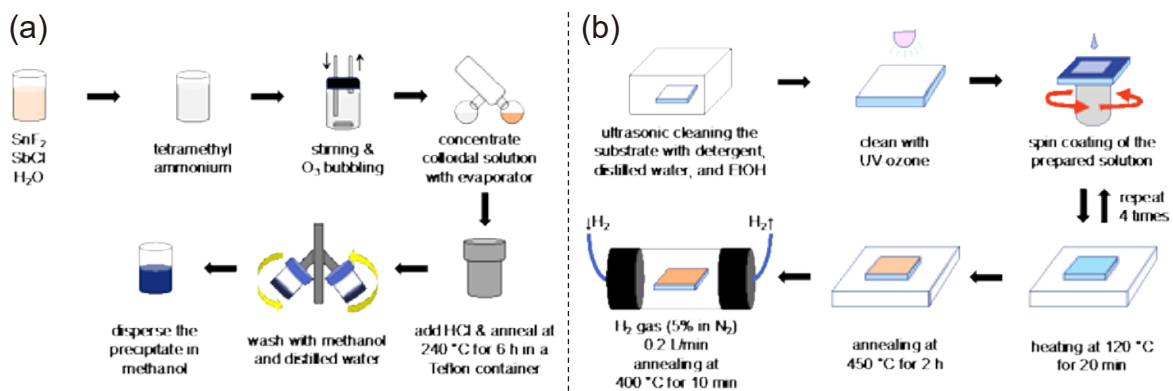


Fig. 1. Schematic images of production method, (a) Sb-SnO₂ nanoparticle colloid, (b) Sb-SnO₂ thin film coated glass substrate.

films were then spin-coated on glass plates. The amount of solution to be dropped was 120 μL , and the substrates were spin-coated and dried at 120 $^{\circ}\text{C}$ for 20 min. The substrates were then transferred to an electric furnace and annealed at 450 $^{\circ}\text{C}$ for 2 h.

3. Results and discussions

Figure 2 shows the resistivity measurement results of Sb-SnO₂. It is known that the resistivity of Sb-SnO₂ depends on the sintering temperature, and it is considered that the sintering treatment significantly improves the crystallinity and the resistivity [2]. Oxygen defects appear in Sb-SnO₂ after hydrogen annealing. Oxygen defects are considered to act as donors and supply electrons to the conductor, which further improves the resistivity [3].

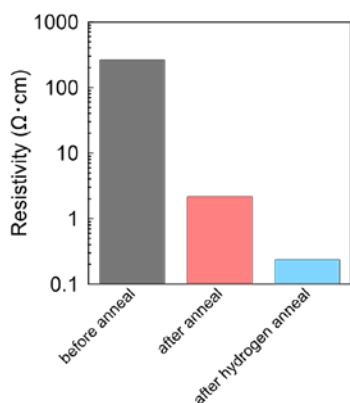


Fig. 2. Comparison of resistivity of Sb-SnO₂ before, after and after hydrogen annealing.

Photoemission electron spectroscopy (PES) and X-ray absorption spectroscopy (XAS) measurements were performed on the samples before and after atomic hydrogen annealing (AHA) treatment to verify the reason of resistivity improvement by hydrogen treatment. Figure 3a is a schematic diagram of the AHA treatment. Atomic hydrogen can be generated by passing H₂ molecules through a high-temperature tungsten mesh in a vacuum [4]. In this study, tungsten mesh was used as the catalyst for AHA treatment. The XAS results show that the π^* bond peak of oxygen slightly shifts to the lower energy side after AHA treatment. Although the shift is obscure, this may be due to the reaction of hydrogen atoms with oxygen, which reduces the O 2p-Sn 5s and O 2p-Sn 5p bonds in SnO₂, resulting in the formation of O 2p-Sn 5p in SnO [5].

In the PES measurement result in Figure 3b, there was a slight decrease in the peak intensity at the upper end of the valence band and a change in the peak position after AHA treatment. This may be due to the reduction of the oxygen orbital

at the upper end of the valence band in SnO₂ by AHA treatment, resulting in a decrease in the density of states. The PES measurement results in Figure 3c show that the structure at the upper end of the valence band was greatly changed and broadened by AHA treatment. This is because Sb-SnO₂ reacts with hydrogen atoms more easily than SnO₂, and the reduction of oxygen by AHA may have dramatically changed the state of Sb-SnO₂.

Further researches are on going for the fully understanding of the phenomenon of conductivity improvement of Sb-SnO₂ by AHA treatments.

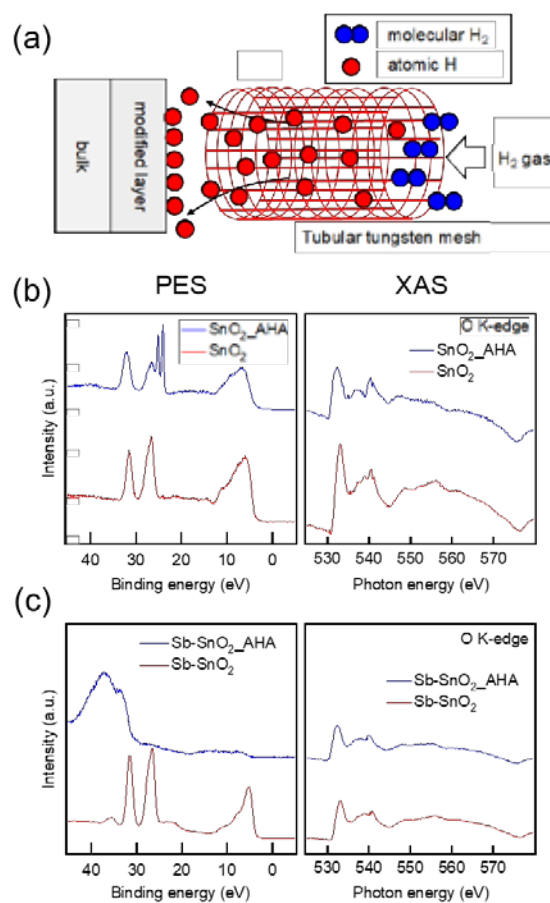


Fig. 3. PES and XAS spectra of SnO₂ and Sb-SnO₂ thin films before and after AHA treatment, (a) schematic diagram of AHA treatment, (b) SnO₂, (c) Sb-SnO₂.

References

- [1] K. Imura, *et al.*, *J. Soc. Powder Technol., Japan*, **54**, (2017), 609.
- [2] Cheng He, *et al.*, *ACS Appl. Energy Mater.* **3**, (2020), 5774.
- [3] H. Kim, *et al.*, *Appl. Phys. Lett.* **84**, (2004), 218.
- [4] A. Heya, *et al.*, *Thin Solid Films*, **625** (2017).
- [5] M. Minohara, *et al.*, *J. Mater. Chem. C*, **21** (2019).

Resonant Photoemission Spectroscopy Study on the 5d Level of Ir Nanoparticles

Takahiro Maruyama^{1,2}, Yuichi Haruyama^{3,4}

¹*Department of Applied Chemistry, Faculty of Science and Technology, Meijo University, 1-501 Shiogamaguchi, Tempaku, Nagoya 468-8502, Japan.*

²*Nanomaterial Research Center, Meijo University, 1-501 Shiogamaguchi, Tempaku, Nagoya 468-8502, Japan.*

³*Department of Materials and Synchrotron Radiation Engineering, Graduate School of Engineering, University of Hyogo, 2167 Shosha, Himeji, Hyogo 671-2280, Japan.*

⁴*Laboratory of Advanced Science and Technology for Industry, University of Hyogo, 3-1-2 Kouto, Ako, Hyogo 678-1205, Japan.*

Abstract

The 5d energy level of Ir nanoparticles deposited on SiO₂/Si substrates was studied by resonant photoemission spectroscopy (RPS). When the excitation energy was 68-70 eV, the intensity of a small peak at around -3 eV was strongly enhanced. This resonance behavior is considered to be due to the transition of photoelectron from the Ir 4f to 5d energy level, indicating that the peak composition was derived from the Ir 5d level. We demonstrated that the RPS is useful to determine the 5d energy level of Ir nanoparticles, which affects the catalyst activity.

1. Introduction

Single-walled carbon nanotubes (SWCNTs) [1] are a group of widely used carbon-based nanomaterials since they show various and tremendous electrical, thermal and mechanical properties. Their electronic properties are closely related to their structure, such as diameter and chirality, therefore, selective growth of SWCNTs with desired structures has been one of the significant issues in the nanocarbon field. Recently, our group succeeded in growth of small-diameter SWCNTs by alcohol catalytic chemical vapor deposition (ACCVD) using Ir as catalysts [2]. By using Ir catalysts, high-density SWCNTs having diameters less than 1 nm were grown. However, the growth mechanism of SWCNTs from Ir catalysts has not been investigated yet. Especially, the effect of electronic states of Ir nanoparticles on the reaction process with feedstock gas has been little understood.

To determine the electronic state of a bulk material, photoelectron spectroscopy is a powerful tool. However, the sizes of catalyst particles for SWCNT growth are a few nm, and they are generally deposited on substrate materials. Therefore, it is difficult to distinguish photoelectrons emitted from nanoparticles from that of substrates in the spectra measured for a sample where nanoparticles are deposited on substrates.

In this study, we attempted to investigate the Ir 5d level of Ir nanoparticles by ultra-violet photoelectron spectroscopy (UPS). By performing resonant photoemission spectroscopy (RPS), we determined the 5d level of Ir

nanoparticles.

2. Experiments

Ir particles were deposited on SiO₂(~100 nm)/Si substrates by using pulsed arc plasma deposition method in a high vacuum. Transmission electron microscopy (TEM) observation showed that the Ir particle sizes were distributed between 1 and 3 nm. The samples were mounted in the sample preparation chamber of the end station of BL7B. After preheating in the preparation chamber, the samples were transferred into the analysis chamber. Then, UPS measurement was performed at room temperature. To investigate the effect of excitation energy on the spectra, RPS was performed by varying the excitation energy between 58 and 72 eV. For comparison, we performed RPS for SiO₂/Si substrates without Ir nanoparticles under the same excitation energies.

Results

Figure 1 (a) shows UPS spectrum of the samples which were only SiO₂/Si substrates and Ir deposited on them. The excitation energy was 58 eV. Referring to previous report, the binding energy is calibrated to the main peak derived from SiO₂[3] and the spectral intensities are normalized with the maximum intensity of valence band. In both spectra, the SiO₂ valence bands were observed and the spectral shapes were quite similar. This would be due to quite small amount of deposited Ir nanoparticles, and the spectral shape of valence band was little affected by Ir.

Figure 1(b) shows UPS spectra for the two samples, where the excitation energy was 68 eV. Although the main spectral shapes were still similar between the two samples, a small structure is seen at around -3 eV for the Ir deposited on SiO₂/Si sample. Considering that this peak did not appear for the SiO₂/Si sample, it should be derived from the energy level of Ir nanoparticles.

To investigate the origin of the Ir derived peak at around -3 eV, we performed RPS, where UPS spectra were measured by various excitation energy from 58 to 72 eV. Figure 2 shows the dependence of the relative intensity of small peak at around -3 eV on the excitation energy. It should be noted that the relative intensity of the small peak increased above 66 eV. Considering that this energy is close to the absorption threshold from the 4*f* to 5*d* level of Ir, this enhancement should be induced by the resonance effect, and we concluded that the peak at around -3 eV was derived from Ir 5*d* level.

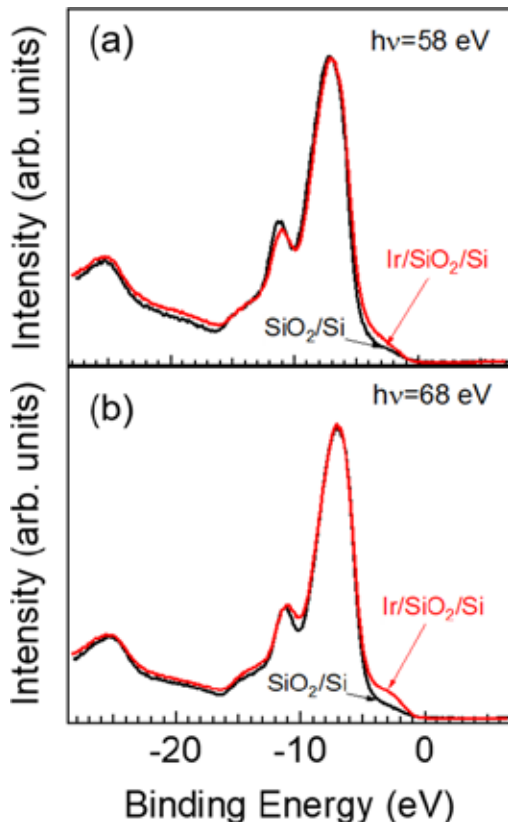


Fig. 1. UPS spectra of Ir deposited SiO₂/Si substrate and SiO₂/Si substrates measured with the excitation energy of (a) 58 eV and (b) 68 eV.

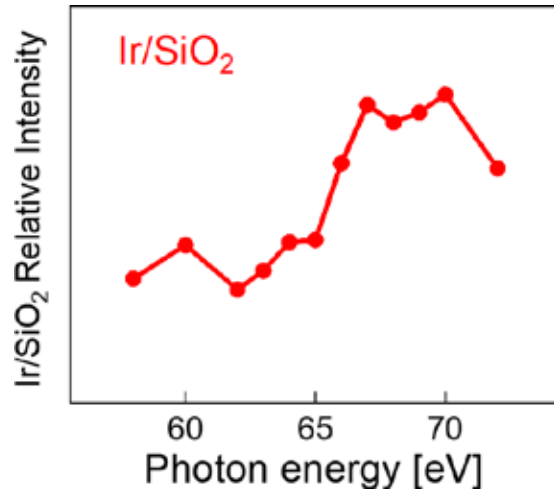


Fig. 2. Dependence of the relative intensity of the small peak at around -3 eV on the excitation energy.

Summary

We performed RPS measurements for Ir nanoparticles deposited on SiO₂/Si substrates. A peak derived from Ir nanoparticles was observed at around -3 eV and its intensity was enhanced by the excitation energy corresponding to the 4*f*-5*d* transition, indicating that this peak was derived from the Ir 5*d* level. By utilizing RPS, we could determine the 5*d* energy level of Ir nanoparticles deposited on SiO₂/Si.

Acknowledgements

This work was partially supported by JSPS KAKENHI Grant Number 19H02563.

References

- [1] S. Iijima and T. Ichihashi, *Nature* **363**, (1993), 603.
- [2] T. Maruyama *et al.*, *Appl. Surf. Sci.* **509**, (2020), 145340.
- [3] E. Bersch, *et al.*, *Phys. Rev. B* **78**, (2008), 085114.

Effect of Atomic Hydrogen Exposure on Hydrogenated Amorphous Carbon Thin Films

Y. Haruyama¹, D. Morimoto¹, A. Heya², K. Sumitomo², S. Ito², K. Yokota³, and M. Tagawa³

¹Laboratory of Advanced Science and Technology for Industry, University of Hyogo

²Graduate School of Engineering, University of Hyogo

³Graduate School of Engineering, Kobe University

Abstract

The effect of atomic hydrogen exposure on hydrogenated amorphous carbon (a-C:H) films was investigated by an X-ray photoelectron spectroscopy (XPS). From the dependence of the wide-scan XPS spectra of an a-C:H film on atomic hydrogen exposure, it was shown that the film was etched with an etching rate of 0.2 nm/min. In addition, the coordination of C atoms in the a-C:H film was investigated as a function of the atomic hydrogen exposure and photoelectron emission angle. This indicated that the coordination of C atoms at the surface of the a-C:H film was not influenced by atomic hydrogen exposure.

1. Introduction

Since amorphous carbon films have interesting properties such as high hardness, a low friction coefficient, and chemical inertness, they have attracted a great deal of attention for a wide range of applications [1, 2]. Owing to their properties, amorphous carbon films are mainly used as coatings on industrial products such as the magnetic heads and media of hard disk drives, machine parts for molds, and cutting tools. In addition, the effect of X-ray irradiation on amorphous carbon films was studied as they are expected to be used as lubricating coatings in space [3]. It was reported that amorphous carbon films are not etched by X-ray irradiation, while hydrogenated amorphous carbon (a-C:H) films are etched by X-rays [4, 5]. However, materials in space applications are subjected not only to X-rays but also bombardment by hydrogen atoms. Therefore, it is important to investigate the effect of atomic hydrogen exposure on amorphous carbon films. Recently, it was reported that hydrogenated amorphous carbon films are etched on exposure to atomic hydrogen at etching rates dependent on the hydrogen contents of the a-C:H films [6]. However, it is not clear whether the surface electronic structure of amorphous carbon films is influenced by atomic hydrogen exposure.

In this study, the effect of atomic hydrogen exposure on a-C:H films was investigated by X-ray photoelectron spectroscopy (XPS). The surface electronic structure of a-C:H films after exposure to atomic hydrogen is discussed based on analysis of the XPS spectra.

2. Experiments

a-C:H films were formed on Si wafers by the RF plasma method. The thickness of the a-C:H films was about 300 nm. The hydrogen concentration of the films was estimated to be 40

at% using the elastic recoil detection analysis method.

Atomic hydrogen was generated using a catalytic chemical vapor deposition method [7]. A schematic diagram of the atomic hydrogen generation apparatus is shown in Fig. 1. W mesh composed of 0.03 mmφ wire at a density of 30 wires per inch was used as the catalyst and heated at a temperature of about 1700 °C. An Ar (95%) and H₂ (5%) gas mixture at a pressure of 10 Pa and flow rate of 100 sccm was used to produce the atomic hydrogen. During atomic hydrogen exposure, the sample temperature measured by a type-K thermocouple was kept below 110 °C by use of a water-cooled sample holder. The distance between the sample and W mesh was 150 mm. Since the atomic hydrogen generation apparatus was connected to the photoelectron analysis chamber through a gate valve, XPS spectra of the a-C:H films after atomic hydrogen exposure were measured without exposing them to air.

All XPS measurements were performed on the BL7B end station at the NewSUBARU facility, University of Hyogo. The wide-scan and C 1s XPS spectra were measured as a function of atomic hydrogen exposure with a hemispherical spectrometer (VG Scienta R3000).

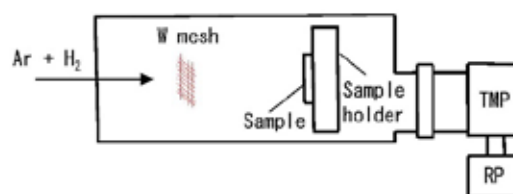


Fig. 1. Schematic diagram of the AHA apparatus.

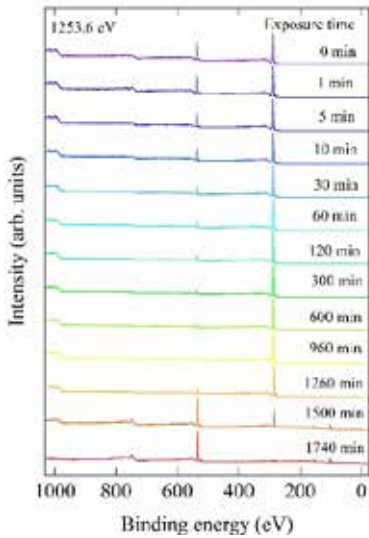


Fig. 2. Wide-scan XPS spectra of hydrogenated amorphous carbon film as a function of atomic hydrogen exposure time.

Mg $K\alpha$ line ($h\nu = 1253.6$ eV) was used as the excitation source. The base pressure in the photoelectron analysis chamber was 2×10^{-8} Pa.

3. Results and discussion

Figure 2 shows the wide-scan XPS spectra of an a-C:H film as a function of atomic hydrogen exposure time. The atomic hydrogen exposure time is indicated beside each spectrum. XPS spectra were normalized by the maximum peak intensity. Before atomic hydrogen exposure, four peaks originating from the C, and O atoms were observed in the XPS spectrum. The four peaks at ~ 1000 , ~ 750 , ~ 530 , and ~ 280 eV were assigned to Auger levels for the C KVV and O KLL decay processes and the O 1s and C 1s levels, respectively [8]. The observation of peaks at ~ 750 and ~ 530 eV suggests that O atoms are present on the surface of the a-C:H film. This is due to the exposure of the sample to air after the formation of the a-C:H film. As the atomic hydrogen exposure increased from 10 to 60 minutes, the intensity of the peaks at ~ 750 and ~ 530 eV decreased gradually. On further increasing the atomic hydrogen exposure up to 1260 minutes, no clear change was observed in the XPS spectrum. At 1500 minutes of exposure, the intensity of the peaks at ~ 750 and ~ 530 eV increased suddenly while that of the peaks at ~ 1000 and ~ 280 eV decreased. In addition, two peaks at ~ 150 and ~ 100 eV appeared. The two peaks at ~ 150 and ~ 100 eV were assigned to Si 2s and 2p levels, respectively [8]. This indicates that the two peaks at ~ 150 and ~ 100 eV originated from the Si substrate. With further

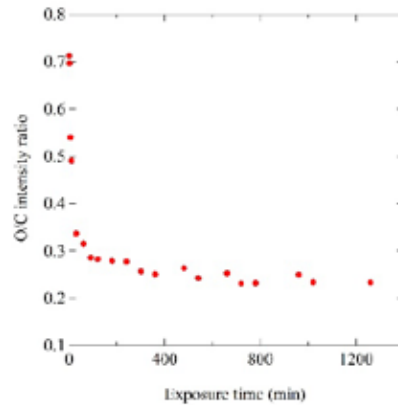


Fig. 3. Relative intensity ratio of O 1s peak to C 1s peak as a function of atomic hydrogen exposure time.

increase of the atomic hydrogen exposure to 1740 minutes, the intensity of the peaks at ~ 750 and ~ 530 eV increased and the peaks at ~ 1000 and ~ 280 eV disappeared. This means that the a-C:H film was etched by atomic hydrogen exposure. From the change in the wide-scan XPS spectra, the etching rate was estimated to be 0.2 nm/min. The evolution of the wide-scan XPS spectrum in Fig. 2 as a function of atomic hydrogen exposure shows the distribution of the chemical composition with depth in the a-C:H film. In other words, the depth profile of the a-C:H film could be revealed by atomic hydrogen etching. In Fig. 3, the relative intensity ratio of the O 1s peak to the C 1s peak (O 1s/C 1s) in the XPS spectrum is plotted as a function of atomic hydrogen exposure time. The O 1s/C 1s relative intensity ratio was 0.7 before atomic hydrogen exposure, and decreased remarkably with increasing exposure up to 60 minutes. Then, it decreased slowly and was saturated at a value of 0.25 with increasing exposure. These results indicate that the O content was greater at the surface and decreased remarkably with depth in the a-C:H film. However, some O content remained in the film. There are two possibilities as to the origin of the O content in the a-C:H film. One is O atom diffusion from the surface into the a-C:H film. The other is introduction of O atoms during the formation of the film. At present, we cannot determine the origin of the O content in the a-C:H film with certainty.

Figure 4(a) shows the XPS spectra of the C 1s level in the a-C:H film as a function of the atomic hydrogen exposure time. Before atomic hydrogen exposure, a peak at 285 eV with a tail on the higher binding energy side was observed. With increasing exposure, the tail was observed to become smaller while the spectral features of

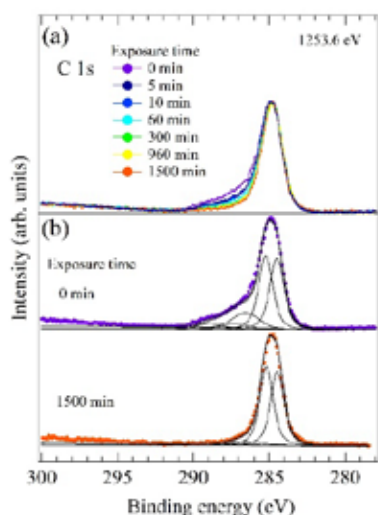


Fig. 4. (a) C 1s XPS spectra for the hydrogenated amorphous carbon film as a function of atomic hydrogen exposure time. (b) Fitting results (lines) for the hydrogenated amorphous carbon film before atomic hydrogen exposure and after atomic hydrogen exposure of 1500 minutes.

the peak at 285 eV were unchanged. In a previous photoelectron study, the C 1s spectrum at 285 eV was decomposed into two components at 284.4 and 285.2 eV [9]. The component at 284.4 eV was assigned to C 1s electrons originating from the sp^2 hybridized C atoms, while the component at 285.2 eV was assigned to C 1s electrons originating from sp^3 hybridized and C-H bonded C atoms [9, 10]. Thus, the coordination of C atoms was evaluated from the spectral features of the peak at 285 eV. The lack of change in the spectral features of the peak indicates that the coordination of C atoms in the a-C:H film was not influenced by atomic hydrogen exposure. On the other hand, the tail at the higher binding energy side was assigned to C 1s electrons originating from the C atoms bonded with O atoms [11]. Therefore, the decrease in the intensity of the tail indicates that the O content in the a-C:H film decreased with increasing atomic hydrogen exposure. This is consistent with the results obtained from the wide-scan XPS spectra of the film.

In order to clarify the coordination of C atoms, curve-fitting analysis was performed on the C 1s XPS spectra using a Mahan line shape functions. Before the fitting procedure, the Shirley background was subtracted from the C 1s XPS spectra. The XPS spectra of the C 1s level in the a-C:H film were reproduced by five components positioned at 284.4, 285.2, 286.8, 287.5, and 288.9 eV, which were assigned to the C 1s

electrons originating from sp^2 hybridized, sp^3 hybridized, C-H bonded, O=C-O bonded, C=O bonded, and O-C-O bonded C atoms, respectively. In Fig. 4(b), the best fitting results (lines) for the a-C:H film before and after atomic hydrogen exposure for 1500 minutes are shown. The five components in the a-C:H film, which were evaluated from the integrated area of each component, are summarized in Table I. With increasing atomic hydrogen exposure, the C contents with the O=C-O, the C=O, and the O-C-O bonded C atoms decreased while the ratio of the intensity of the sp^3 hybridized and C-H bonded C atoms to the sp^2 hybridized C atoms was unchanged. This indicates that the coordination of the C atoms in the a-C:H film was unchanged independent of the atomic hydrogen exposure or O contents.

The effect of atomic hydrogen exposure on a-C:H films was investigated by XPS. Exposure of the a-C:H film to atomic hydrogen induced etching of the a-C:H film. The etching rate was estimated to be 0.2 nm/min. In addition, the coordination of C atoms in a-C:H films was found to be unaffected by atomic hydrogen exposure. This indicates that the surface of the a-C:H film is not subject to damage by atomic hydrogen exposure. Therefore, we propose that the depth profile of a-C:H films can be measured with no damage by atomic hydrogen etching.

References

- [1] J. Ullmann, Nucl. Instrum. Methods Phys. Res., Sect. **B 127**, (1997), 910.
- [2] H. Tsai and D. B. Bogy, J. Vac. Sci. Technol. **A 5**, (1987), 3287.
- [3] C. Donnet *et al.*, Surf. Coat. Technol. **68–69**, (1994), 626.
- [4] H. Kyuragi and T. Urisu, Appl. Phys. Lett. **50**, (1987), 1254.
- [5] K. Kanda *et al.*, Jpn. J. Appl. Phys. **50**, (2011), 055801.
- [6] A. Heya *et al.*, J. Photopolymer Sci. and Tech. **33**, (2020), 419.
- [7] A. Heya, A. Masuda, and H. Matsumura, Appl. Phys. Lett. **74**, (1999), 2143.
- [8] C. D. Wagner *et al.*, Handbook of X-ray photoelectron spectroscopy, ed. G. E. Muilenberg (Perkin-Elmer, Eden Prairie, Minnesota, 1978).
- [9] Y. Haruyama *et al.*, Jpn. J. Appl. Phys. **47**, (2008), 3380.
- [10] Y. Haruyama *et al.*, Jpn. J. Appl. Phys. **48**, (2009), 055505-3.
- [11] A. Heya *et al.*, J. Photopolymer Sci. and Tech. **33**, (2020), 419.

Fundamental Study of EUV Mask on EUV Lithography at NewSUBARU Synchrotron Light Facility

Takeo Watanabe, Tetsuo Harada, Shinji Yamakawa

Center for EUVL, Laboratory of Advanced Science and Technology for Industry, University of Hyogo, 3-1-2 Kouto, Kamigori, Akou-gun, Hyogo 678-1205, Japan

Abstract

Since 2019, EUV lithography has started to be used for the mass production of 7-nm-node-logic devices. However, many significant issues on EUV lithography still remain in the fabrication of future devices. The technical issues are the development technologies of resist, mask, and EUV light source. Therefore, many significant fundamental research has been carried out at our facility. Here the EUV mask technologies is highlighted. It is described the fundamental research activities on EUV lithography at NewSUBARU synchrotron light facility, which is related with EUV mask technologies.

1. Introduction

Since 1996, the program of the research and development (R&D) on EUV lithography had been started at the Laboratory of Advanced Science and Technology for Industry, Himeji Institute Technology (HIT) (present University of Hyogo: UoH) using the NewSUBARU synchrotron light source^{1,2}. The collaboration work was started between HIT, Nikon, and Hitachi Central Research Laboratory in 1996. We designed three aspherical imaging optics³ and demonstrated the patterning of 42-nm-isolated line, and 56-nm line and space using the ETS-1 exposure tool which consisted of three-aspherical-imaging optics¹. And in ASET program, we demonstrated 60 nm L/S patterning in a full-field exposure area of 10 mm×10 mm using the 2nd version of ETS-1 with synchronized mask and wafer stage system.^{4,5} After that we involved in the three more consortiums such as Selete, EUVA, and EIDEC, and we collaborated with many domestics and overseas private companies, institutes, and university in the fields of optics, resist, and mask technologies. The R&D of EUV resist evaluation is listed on the papers.⁶⁻¹⁴ The Center for EUVL was established in the Laboratory of Advanced Science and Technology for Industry, UoH in October 2010. The mission of this center is to accelerate and to update the EUV technology toward the phase of high-volume manufacturing (HVM). We have total nine beamlines at the NewSUBARU synchrotron light facility, and three beamlines are performed to use only for the R&D on EUVL.

From 2019, EUV lithography was started to use for the mass production of 7-nm-node-logic devices. However, many significant issues on EUV lithography still remain for the fabrication of future devices. Therefore, many significant fundamental research concerning EUV masks including pellicles, resists, and EUV optical element have been carried out in our facility. This paper focuses about the various evaluation system which are installed at NewSUBARU beamlines.

2. Evaluation Tools

For a EUV mask, it was prepared that 1) the in-band reflectometer, 2) the bright field EUV microscope for the defect inspection of EUV masks, and 3) the EUV coherent scatterometry microscope (CSM) for the defect characterization of EUV masks. In addition, the large reflectometer for the measurement of a large collector mirror for the EUV-laser-produced-plasma light source was installed at the BL10B beamline. The EUV-CSM method has a capability for the various application including resist defect inspection. Recently, it is prepared that 1) the high-power exposure tools in hydrogen atmosphere in the same pressure condition of ASML EUV exposure tool to evaluate the radiation hardness of the materials which is used for the EUV masks, and 2) the out of band reflectometer for the EUV mask evaluation.

1.1 NewSUBARU synchrotron light facility

NewSUBARU synchrotron light facility was established at the Laboratory of Advanced Science and Technology for Industry, University of Hyogo, Japan in 1994. This synchrotron facility is the largest facility which is operated by university in Japan. The main mission of this facility is the usage of the industrial application to support the development of the advanced technology. The NewSUBARU storage ring is middle-size electron-beam storage ring and the circumstance is approximately 120 m. In this facility nine beamlines have been operated. The Center for EUVL was established in 2010 at this laboratory to support the EUV lithographic technology for the productions of advanced semiconductor devices. This center has three beamlines for the fundamental research on EUV lithography as shown in Fig.1.

NewSUBARU has restarted after an innovative renewal from April 20th, 2021. As the light intensity of the synchrotron radiation has improved up to

approximately 20%, the research and development of further advanced lithographic technologies including EUVL can accelerate. NewSUBARU is adjacent to SPring-8, electron beam has been supplied to generate synchrotron radiation from SPring-8. From recent years, aiming for more advanced operation, we have promoted the construction of a new injection system (c-band linear acceleration (linac) system) which can self-sufficient electrons to the NewSUBARU storage ring. In 2020, a new injector and an electron gun that generates electrons were installed, and after a trial run and adjustment of the new system in 2021, the user operation of NewSUBARU has started.

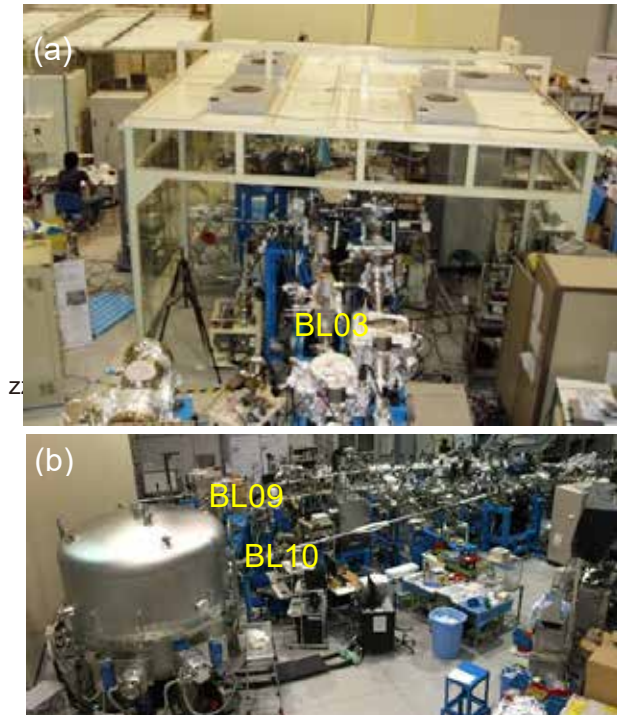


Figure 1. Three beamlines for the fundamental research on EUV lithography, (a) BL03, and (b) BL09 and BL10.

1.2 In-band reflectometer for EUV masks and optical elements

In EUV lithography, Mo/Si multilayer (ML) is used for the reflect the EUV light. The optics for EUV lithography and EUV mask is reflective -type and they are employing Mo/Si multilayer. To maintain the high throughput of the circuit patterning on a wafer the high reflectivity of Mo/Si multilayer is significant. At BL10A beamline, the multilayer reflectometer had been installed. The beamline setup and its photograph are shown in Fig. 2(a) and (b), respectively. The wavelength resolution is approximately $\lambda/3000$.

In order to increase the power of the laser produced plasma (LPP) EUV light source, the huge collector mirror is necessary. Thus, the huge reflectometer for the reflectivity measurement for the huge collector mirror of the LPP EUV light source had been installed at the BL10B beamline.¹⁵ The Mo/Si ML mirror which has a size up to 800-mm-diameter and 50-mm-thick, and a weight up to 50 kg can be measured using

this huge reflectometer. The configuration of this reflectometer is shown in Fig. 3. The height and width of the reflectometer are approximately 2.9 m and 2.6 m, respectively. The reflectivity spectra which were measured at NewSUBARU and PTB are shown in Fig. 4 for the round robin mirror sample. The reflectivity spectra of those are consistent between each other. So our huge reflectometer is assigned to be the world standard one.

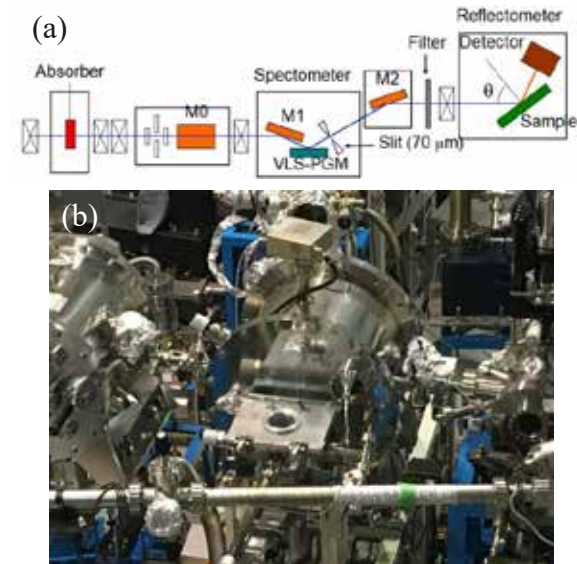


Figure 2. (a) Beamline setup of BL10A beamline for the EUV reflectometer, and (b) photograph of BL10A.

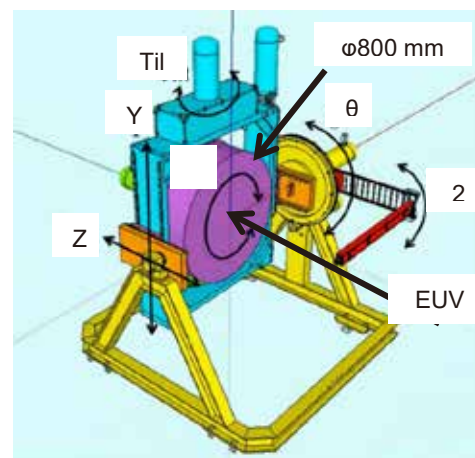


Figure 3. System configuration of large reflectometer.

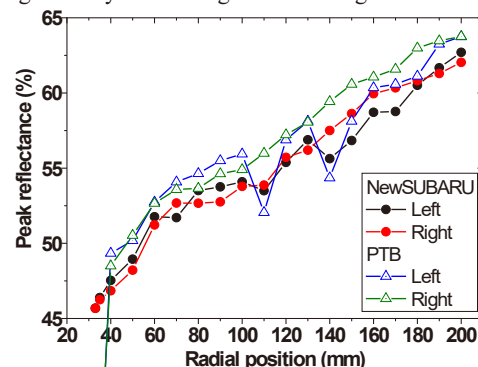


Figure 4. The round robin reflectance measurement results between NewSUBARU and PTB.

1.3 Bright field EUV microscope^{16, 17} for the EUV mask defect inspection

The bright field mask inspection tool was installed at the BL03B beamline.^{18,19} This tool consists of the loadlock chamber to exchange a EUV mask, main observation chamber to observe the absorber pattern image of EUV mask, and the zooming tube for forming the image of the mask pattern, the Schwarzschild-type imaging optics was employed as a 30X magnification optics to observe the mask pattern image combined with the 200X zooming tube. The zooming tube consists of CsI and electromagnetic lens, and micro-channel plate (MCP), and CCD camera. Thus, total magnification of the mask pattern can achieve 6,000X. The system configuration is shown in Fig. 5. Using this system, the criteria between printable and non-printable regions by parameters of defect width and depth was clarified as shown in Fig. 6.²⁰ The horizontal and vertical axes indicate the width and height of the programmed defects of EUV mask.

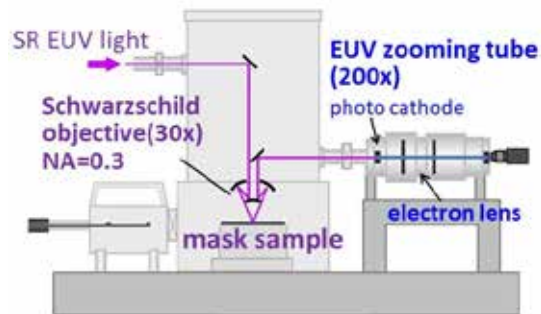


Figure 5. System configuration of brightfield EUV microscope.

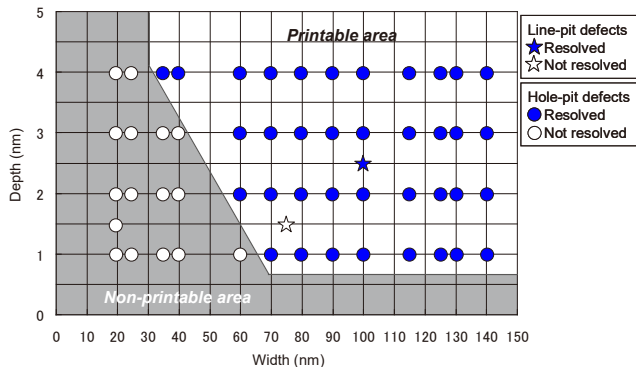


Figure 6. Defect threshold between printable and non-printable.

1.4 EUV coherent scatterometry microscope for the EUV mask defect inspection

The system configuration of EUV coherent scatterometry microscope (CSM) and is shown in Fig. 7.^{21, 22} The high harmonic laser was employed as a light source of the EUV CSM. The coherent light can be produced by the pin hole and the diffraction image by the EUV coherent light can be observed by the charged couple device (CCD) camera. The EUV mask

image of 88 nm line and space (L/S) pattern with a 30 nm line defect can be reconstructed by the iteration calculation method from the diffraction image. And the mask defect signals can be observed by the diffraction images as a horizontal line signal.

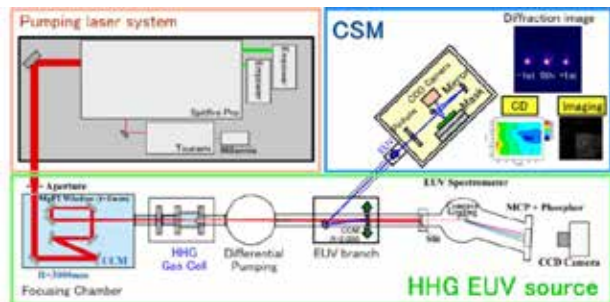


Figure 7. System configuration of the standalone CSM system with the high harmonic gas laser system.

As shown in Fig. 8, using Fresnel zone plate, the coherent EUV light can focus on a mask within 140 nm in diameter. This system so-called micro-CSM. Using this micro-CSM, the natural defect observation was succeed as shown in Fig,s 9 and 10. Figures 9 and 10 are shown the intensity and phase reconstructed images using micro-CSM, respectively. The micro-CSM observation results is consistent those of atomic micro force (AFM). The smallest with of the mask bump defect of 33 nm × 28 nm in size and 1.7 nm in height can be observed.^{23, 24}

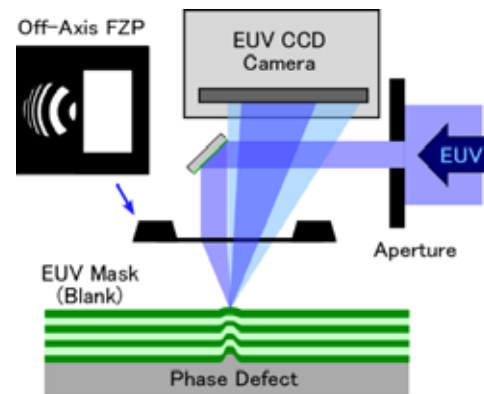


Figure 8. System configuration of micro-CSM.

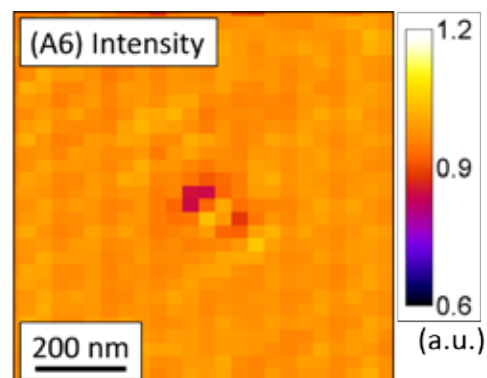


Figure 9. Intensity distribution result of mask dump natural defect of 33 nm × 28 nm in size and 1.7 nm in height.

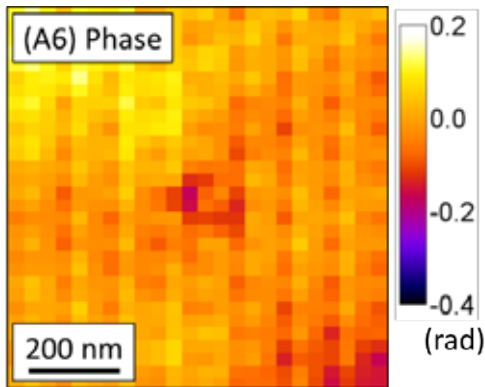


Figure 10. Phase distribution result of mask dump natural defect of $33 \text{ nm} \times 28 \text{ nm}$ in size and 1.7 nm in height.

1.5 High power EUV exposure tool in hydrogen atmosphere

The hydrogen environment in the exposure tool²⁵ which is employed in high volume manufacturing to protect from the carbon contamination during the EUV exposure. However, since hydrogen is the smallest atom and it is easy to diffuse into the materials, the hydrogen embrittlement is more likely to occur to not only the mask materials such as absorber, Mo/Si multilayer, and pellicle but also the resist materials, and the patterning characteristics becomes worse. Thus, the high power EUV exposure tool in hydrogen atmosphere is prepared at the BL09A beamline to study the hydrogen embrittlement of EUV masks and resists. The photograph of this system is shown in Fig. 11. The hydrogen can be introduced up to 70 Pa . And the EUV power up to 30 W/cm^2 on a sample can be supplied.

Figure 12 shows the results of the reflectivity changes during high power EUV exposure as the parameter of the EUV exposure dose and the hydrogen pressure. it is found out that the contamination mode and



Figure 11. the hydrogen embrittlement evaluation tool of EUV masks and resist.

contamination removal modes depend on the hydrogen pressure. In the high and low hydrogen pressure regions, the carbon removal and the carbon contamination occur dominantly, respectively. And the Mo/Si multilayer damages might occur by the existence of the particle additive during the multilayer sputtering process.

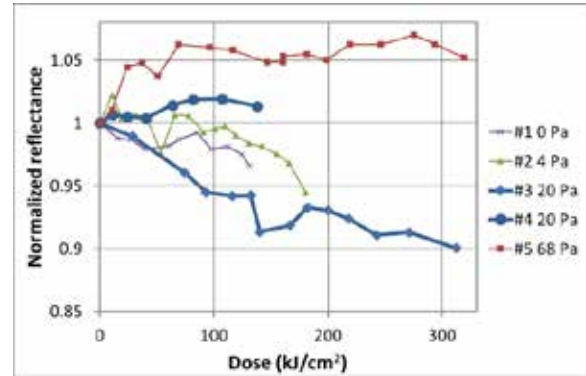


Figure 12. The study results of the reflectivity changes during high power EUV exposure as the parameter of the hydrogen pressures.

2. CONCLUSIONS

From 2019, EUV lithography was started to use for the mass production of 7-nm-node-logic devices. However, many significant issues on EUV lithography still remain for the fabrication of future devices such as 5-nm-node and beyond. The technical issues are the development technologies of resist, mask, and EUV light source. Therefore, many significant fundamental researches have been carried out at our facility. It is focused on the fundamental research activities on EUV lithography at NewSUBARU synchrotron light facility, which is related with EUV mask technologies such as 1) the in-band reflectometer for EUV masks and optical elements, 2) bright field EUV microscope for the EUV mask defect inspection, 3) EUV coherent scatterometry microscope for the EUV mask defect inspection, 4) high power EUV exposure tool in hydrogen atmosphere, 5) out of band (OoB) reflectometer. Using these tools, EUV lithography R&D will continue for the next generation lithography to use the EUV lithography to guarantee the future mass production of EUVL.

REFERENCES

- [1] Ando, A., Amano, A., Hashimoto, S., Kinoshita, H., Miyamoto, S. Mochizuki, T., Niibe, M., Shoji, Y., Terasawa, M., and Watanabe, T., "VUV and Soft X-ray Light Source "NewSUBARU," Proc. of the 1997 Particle Accelerator Conference, 757-759 (1998).
- [2] Hashimoto, S., Ando, A., Amano, S., Haruyama, Y., Hattori, H., Kanda, K., Kinoshita, H., Matsui, S.,

- Mekaru, H., Miyamoto, S. Mochizuki, T., Niibe, M., Shoji, Y., Utsumi, Y., Watanabe, T., and Tsubakino, H., "Present Status of Synchrotron Radiation Facility "NewSUBARU"," Trans. Materials Research Soc. Japan, **26**, 783-786 (2001).
- [3] Watanabe, T., Mashima, K., Niibe, N., and Kinoshita, H., "A Novel Design of Three-Aspherical-Mirror Imaging Optics for Extreme Ultra-Violet Lithography," Jpn. J. Appl. Phys., **36**, 7597-7600 (1997).
- [4] Watanabe, T., Kinoshita, H., Nii, H., Li, Y., Hamamoto, K., Oshino, T., Sugisaki, K., Murakami, K., Irie, S., Shirayone, S., Gomei, Y., and Okazaki, S., "Development of the Large Field Extreme Ultraviolet Lithography Camera," J. Vac. Sci. Technol., **B18**, 2905-2910 (2000).
- [5] Watanabe, T., Kinoshita, H., Hamamoto, K., Hosoya, M., Shoki, T., Hada, H., Komano, H., and Okazaki, S., "Fine Pattern Replication Using ETS-1 Three-Aspherical Mirror Imaging System," Jpn. J. Appl. Phys., **41**, 4105-4110 (2002).
- [6] Watanabe, T., Kinoshita, H., Sakaya, N., Shoki, T., and Lee, S. Y. "Novel Evaluation System for Extreme Ultraviolet Resist in NewSUBARU," Jpn. J. Appl. Phys., **44**, 5556-5559 (2005).
- [7] Watanabe, T., Kinoshita, H., Nii, H., Hamamoto, K., Tsunakino, H., Hada, H., Komano, H., and Irie, S., "Photoinduced Outgassing from the Resist for Extreme Ultraviolet Lithography by the Analysis of Mass Spectroscopy," J. Vac. Sci. Technol., **B19**, 736-742 (2001).
- [8] Watanabe, T., Kikuchi, Y., Takahashi, T., Katayama, K., Takagi, I., Sugie, N., Tanaka, H., Shiobara, E., Inoue, S., Harada, T., and Kinoshita, H., "Development of Tool for Contamination Layer Thickness Measurement Using High Power Extreme Ultraviolet Light and in Situ Ellipsometer," Jpn. J. Appl. Phys. **52** (2013) pp.056701-1, 056701-5.
- [9] Ohnishi, R., Watanabe, T., Fukushima, Y., Osugi, M., and Kinoshita, H., "Transmission Measurement Using Extreme Ultraviolet Light for the Development of Extreme Ultraviolet Resist," Jpn. J. Appl. Phys., **48**, 06FA08 (2009), 06FA08.
- [10] Niihara, S., Mamezaki, D., Watanabe, M., Harada, T., and Watanabe, T., "Absorption Coefficient Measurement Advanced Method of EUV Resist by Direct-Resist Coating on a Photodiode," J. Photopolym. Sci. Technol., **30**, 87-92 (2017).
- [11] Urayama, T., Watanabe, T., Yamaguchi, Y., Matsuda, N., Fukushima, Y., Iguchi, T., Harada, T., and Kinoshita, H., "EUV Interference Lithography for 1X nm," J. Photopolymer Sci. Technol., **24**, 153-157 (2011).
- [12] Yoshifuji, M., Niihara, S., Harada, T., Watanabe, T., "Fabrication of High-Aspect-Ratio Transmission Grating Using DDR Process for 10-nm EUV Resist Evaluation by EUV Interference Lithography," J. Photopolym. Sci. Technol., **31**, 215-220 (2018).
- [13] Watanabe, T., Haruyama, Y., Shiono, D., Emura, K., Urayama, T., Harada, T., and Kinoshita, H., "Chemical Reaction Analysis of EUV CA Resist using SR Absorption Spectroscopy," J. Photopolymer Sci. Technol., **25**, 569-574 (2012).
- [14] Kuki, M., Uemura, T., Yamaguchi, M., Harada, T., Watanabe, T., Muramatsu, Y., and Kinoshita, H., "Development of High-Reflective W/Si-multilayer Diffraction Grating for the Analysis of Fluorine Materials," J. Photopolym. Sci. Technol., **28**, 531- 536 (2015).
- [15] Iguchi, H., Hashimoto, H., Kuki, M., Harada, T., Watanabe, T., and Kinoshita, H., "Development of a reflectometer for a large EUV mirror in NewSUBARU," Proc. SPIE, **9658**, 965819 (2015).
- [16] Haga, T., Kinoshita, H., Hamamoto, K., Takada, S., Kazui, N., Kakunai, S., Tsubakino, H. and Watanabe, T., "Evaluation of finished extreme ultraviolet lithography (EUVL) masks using a EUV microscope," Jpn. J. Appl. Phys., **42**(Part 1, No. 6B), 3771-3775 (2003).
- [17] Watanabe, T., Haga, T., Shoki, T., Hamamoto, K., Takada, S., Kazui, N., Kakunai, S., Tsubakino, H., and Kinoshita, H., "Pattern inspection of EUV mask using a EUV microscope," Proc. SPIE, **5130**, 1005-1013 (2003).
- [18] Hamamoto, K., Tanaka, Y., Lee, S. Y., Hosokawa, N., Sakaya, N., Hosoya, M., Shoki, T., Watanabe, T. and Kinoshita, H., "Mask defect inspection using an extreme ultraviolet microscope," J. Vac. Sci. Technol., **B23**, 2852-2855 (2005).
- [19] Mizuta, Y., Osugi, M., Kishimoto, J., Sakaya, N., Hamamoto, K., Watanabe, T., and Kinoshita, H., "Development of Optical Component for EUV Phase-Shift Microscopes," Proc. SPIE, **6517**, 651733 (2007).
- [20] Takase, K., Kamaji, Y., Sakagami, N., Iguchi, T., Tada, M., Yamaguchi, Y., Fukushima, Y., Harada, T., Watanabe, T. and Kinoshita, H., "Imaging Performance Improvement of an Extreme Ultraviolet Microscope," Jpn. J. Appl. Phys., **49**, 06GD07 (2010).
- [21] Harada, T., Nakasuji, M., Kimura, T., Watanabe, T., Kinoshita, H., "Imaging of extreme-ultraviolet mask patterns using coherent extreme-ultraviolet scatterometry microscope based on coherent diffraction imaging," J. Vac. Sci. Technol., **B29**, 06F503 (2011).
- [22] Nakasuji, M., Tokimasa, A., Harada, T., Nagata, Y., Watanabe, T., Midorikawa, K., and Kinoshita, H., "Development of coherent extreme-ultraviolet scatterometry microscope with high-Order harmonic generation source for extreme-ultraviolet mask inspection and metrology," Jpn. J. Appl. Phys., **51**, 06FB09 (2012).
- [23] Harada, T., Hashimoto, H., Amano, T., Kinoshita, H. and Watanabe, T., "Actual defect observation results of an extreme-ultraviolet blank mask by coherent diffraction imaging," Appl. Phys. Express, **9**, 035202 (2016).
- [24] Hashimoto, H., Harada, T. and Watanabe, T., "Observation results of actual phase defects using

micro coherent EUV scatterometry microscope,” Proc. SPIE, **9985**, 99850K (2016).
[25] Ohgata, A., Harada, T., and Watanabe, T., “Development of High-Power EUV Irradiation Tool in Hydrogen Atmosphere,” MNC2019, Hiroshima, Japan, [27] 481N (2019).

Oct. 28, 2019.

[26] Tsuda, K., Harada, T., Watanabe, T., “Development of an EUV and OoB Reflectometer at NewSUBARU Synchrotron Light Facility,” Proc. SPIE **11148**, 111

Hydrogen Cleaning Evaluation of Mo/Si Multilayer Using an EUV Irradiation Tool at NewSUBARU

Tetsuo Harada, Shinji Yamakawa, Takeo Watanabe
Center for EUVL, LASTI, Univ. of Hyogo

Abstract

Beamline optics of BL-09C for the EUV irradiation tool was upgrade. The irradiation intensity was improved from 6 W/cm^2 to 30 W/cm^2 , which is enough high to evaluate mask and pellicle material for next generation EUV exposure tool. The preliminary irradiation result of Mo/Si multilayer sample was reported. Carbon contamination was removed by the EUV irradiation with hydrogen gas (70 Pa).

1. Introduction

In EUV lithography, the carbon contamination causes the reflectance decrease of a Mo/Si multilayer and deterioration of resolution performance. The origin of the contamination is residual carbon gas in the vacuum chamber, which is contaminated on the mirror under the high-power EUV irradiation. In order to reduce the contamination, hydrogen gas is introduced in the EUV lithography scanner. However, there is few reports for contamination cleaning performance of the hydrogen gas. On the other hand, Mo/Si multilayer could be damaged by the EUV-induced hydrogen plasma which would diffuse into the interface between Mo and Si layers. In order to evaluate this damage and cleaning effect, the EUV irradiation tool (Fig. 1) in hydrogen gas atmosphere has been developed at the BL-09-long-undulator beamline of the NewSUBARU synchrotron light facility [1, 2]. We upgraded the beamline to increase the irradiation intensity.

As the result the EUV irradiation intensity was up to 30 W/cm^2 , which are equivalent to the EUV source power of 900 W for the mask evaluation and 600 W for the pellicle evaluation, respectively. The EUV dose was

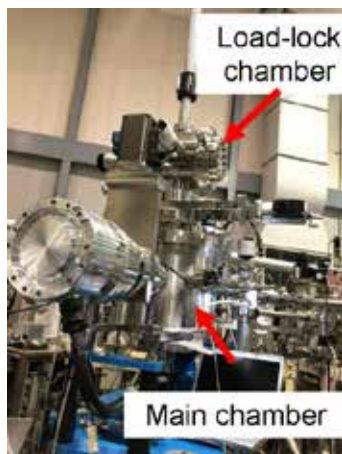


Fig. 1. Photograph of EUV Irradiation Tool at NewSUBARU BL-9C.

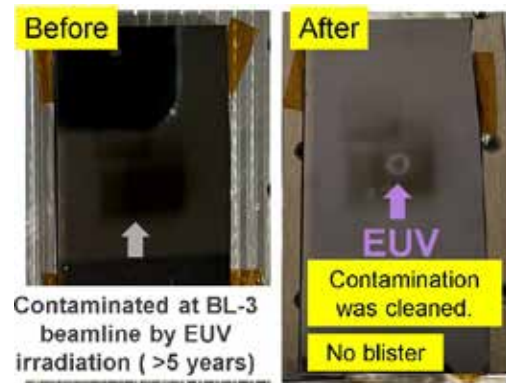


Fig. 2. Photograph of a Mo/Si multilayer before and after EUV irradiation with hydrogen gas.

108 kJ/cm^2 per hour. The hydrogen gas pressure was up to 70 Pa.

2. Experiments and Results

The irradiation sample was a Mo/Si multilayer on glass substrate. The surface of the sample was carbon contaminated shown in Fig. 1. The EUV power was 30 W/cm^2 , and the hydrogen pressure was 70 Pa. The beam size on the sample was $0.5 \text{ mm (V)} \times 1.2 \text{ mm (H)}$. The irradiation time was 9.5 hours, which was corresponded to 960 kJ/cm^2 . The carbon contamination on the irradiated position was cleaned shown by an arrow in Fig. 1. This result significantly shows the EUV induced plasma can clean carbon contamination. In addition, there was no damage (no blister) on the irradiation position.

References

- [1] T. Harada, *et al.*, *Jpn. J. Appl. Phys.* **60**, (2021), 087005.
- [2] T. Harada, *et al.*, *Proc. SPIE* **11908**, (2021) 119080U.

X-ray Absorption Spectroscopy of Liquids and Gases using a Simple Liquid Cell

Tomoki Eguchi, Koji Takahara, Satoru Suzuki
LASTI, University of Hyogo

Abstract

Our laboratory has been developing a simple liquid cell for scanning electron microscopy observation. Here, we applied the liquid cell to X-ray absorption spectroscopy of liquid and gas samples at NewSUBARU BL9A. X-ray absorption spectra were obtained for water, ammonia borane solution, γ -butyrolactone, and atmospheric nitrogen.

1. Introduction

Unlike solid states, the analysis of liquid samples is generally considered very difficult in soft X-ray absorption spectroscopy (XAS), which requires measurement under vacuum, because the shape is not fixed and evaporation occurs. There have been various approaches to synchrotron radiation analysis of liquids [1-2]. As an example, in soft X-ray emission using synchrotron radiation, the measurement of liquid water using a liquid pumping cell with a silicon nitride (SiN) thin film as a window material has been reported [3-4]. We developed a simple liquid cell to seal the liquid and gas [2], which enables a simple XAS measurement without the need for additional special equipment. In this experiment, we used encapsulated simple liquid cells. We performed a certain number of XAS measurements using the simple liquid cells, but the transmission window was not broken after the measurements. At the NewSUBARU BL9A, the prepared samples can be used not only for XAS but also for X-ray emission spectroscopy (XES) and photoelectron emission microscopy (PEEM), which enables many synchrotron radiation analyses in a microscopic region.

2. Experiments

Figure 1 shows a schematic diagram of the simple liquid or gas cell for XAS created in this experiment. Liquid cells were fabricated using Si chips with SiN films (Silson Ltd., England) or SiC

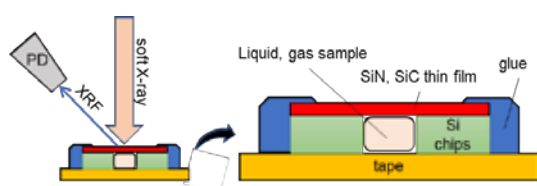


Fig. 1. Schematic diagram of the simple liquid or gas cell.

films (NTT-AT Co., Tokyo) as electron transmission windows, the thicknesses of the SiN and SiC films were 100 nm and 200 nm, respectively, and the dimensions were 1.5 mm \times 1.5 mm, 1.44 mm \times 0.43 mm. XAS measurements were performed at the synchrotron radiation facility NewSUBARU BL09A using a high-brightness light source and a high-resolution spectrometer on a long undulator, and were performed at room temperature in vacuum using the fluorescence yield method.

3. Results and discussion

Figure 2 shows the X-ray absorption spectrum of H₂O (liquid) measured. Three peaks are observed around O K region of water. The pre-peak observed at 535 eV is mainly associated with broken or weakened hydrogen bonds, indicating a transition from the 1s orbital of oxygen to $4a_1$ of oxygen. The main-peak observed at 537.7 eV is associated with the presence of interstitial water molecules, indicating a transition from the 1s orbital of oxygen to $2b_2$ of oxygen. These two peaks can be understood in terms of hydrogen bonding effects, since the excited states of both $4a_1$ and $2b_2$ of gas

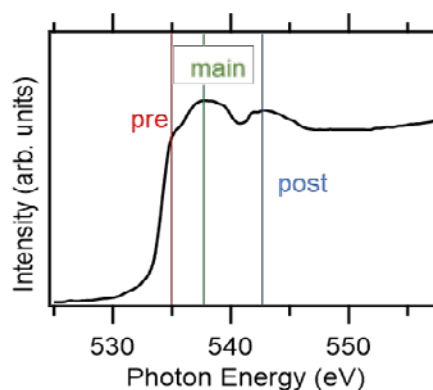


Fig. 2. The X-ray absorption spectrum of H₂O (liquid) around O K region.

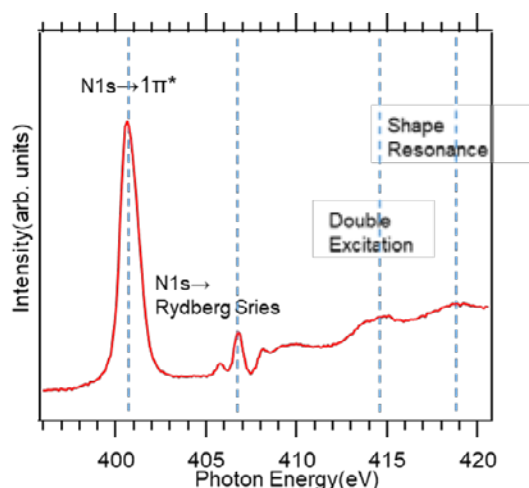


Fig. 3. The X-ray absorption spectrum of nitrogen in air around N K region.

phase water are polarized toward hydrogen atoms and are thus sensitive to hydrogen bond donation. Then, the post-peak originating from hydrogen bonding were observed at 541-543 eV [5-7]. These values are generally consistent with the reported XAS values for H₂O (liquid), and it can be said that the simple liquid cell is applicable to XAS measurements for liquid samples.

Figure 3 shows the X-ray absorption spectrum of nitrogen in air measured in this experiment. Four peaks were observed in the absorption spectrum of atmospheric nitrogen. The peak at 400.7 eV indicates a transition from the 1s orbital to the 1 π orbital of nitrogen, and the peak at 406.7 eV indicates a transition from the 1s orbital of oxygen to the electronically. It indicates a transition from the 1s orbital of oxygen to the Rydberg state, which is an excited state with an energy following the Rydberg formula. The broad bulge around 410 eV is due to the ionization energy threshold. The ionization energy threshold is the energy required to completely liberate an electron from the ionic core of an atom or molecule. The energies of the Rydberg series converge to ionization states with ionization energies: the peak observed between 414 eV and 415 eV indicates a transition to a doubly excited state, and the peak near 419 eV indicates shape resonance [8]. These values are generally consistent with those reported for nitrogen gas [8], indicating that the simple liquid cell is applicable to XAS measurements of gaseous samples.

We report the X-ray absorption spectra of aqueous ammonia borane solutions. Figures 4 show the X-ray absorption spectra of aqueous ammonia borane solutions, respectively. In this experiment, 1 mol/L aqueous ammonia borane solution was prepared and XAS measurements were performed.

In Figure 4(a), the absorption edge of boron was observed at 194 eV, and in Figure 4(b), the absorption edge of nitrogen was observed at 400.7 eV. However, due to insufficient concentration, the detected light intensity is low and strongly affected by the background shape.

We report the X-ray absorption spectrum of Γ -butyrolactone (GBL), for which there are currently no reported cases. Figures 5 show the X-ray absorption spectra of Γ -butyrolactone, respectively, divided by the spectrum of washed gold with hypochlorous acid. In general, gold mesh is often used as a light intensity monitor in soft X-ray absorption measurements at the C-K absorption edge using synchrotron radiation. However, in beamlines not equipped with a vacuum deposition system, it is very difficult to measure accurate spectra because carbon absorption structures appear in the background. In soft X-ray absorption measurements at the C-K absorption edge, washing gold with hypochlorous acid is effective in removing contamination due to carbon adsorption.

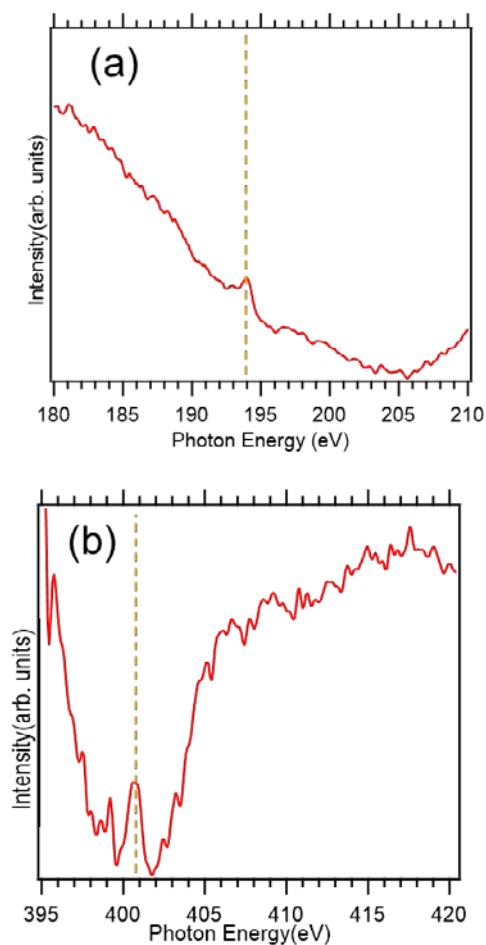


Fig. 4. the X-ray absorption spectra of aqueous ammonia borane around (a) B K and (b) N K region.

effective in removing contaminants [14]. We analyzed each peak with reference to the peaks [10–13] identified in compounds such as PBT and PET, which have similar structures and, like GBL, ester groups.

From Figure 5(a), a peak indicating the transition of C=O to the π^* orbital at 532.5 eV, a peak indicating the transition of C-O to the π^* orbital at 535 eV, a peak indicating the transition of C-O-C to the σ^* orbital, which is not observed in the carboxyl group and is unique to ester groups, at 538–539 eV, and at 542 eV a peak indicating the transition of C-O to the peak indicating the transition to the C-O σ^* orbital was observed at 542 eV. From Fig. 5(b), peaks indicating transitions to the π^* orbital of aromatic rings at 285 eV and 287.2 eV, and a peak indicating a transition to the π^* orbital of C=O at 288.3 eV were observed. At 289–291 eV, broad peaks indicating transitions of C=C (aromatic ring), C-C, C=O, and C-O to the σ^* orbital were observed.

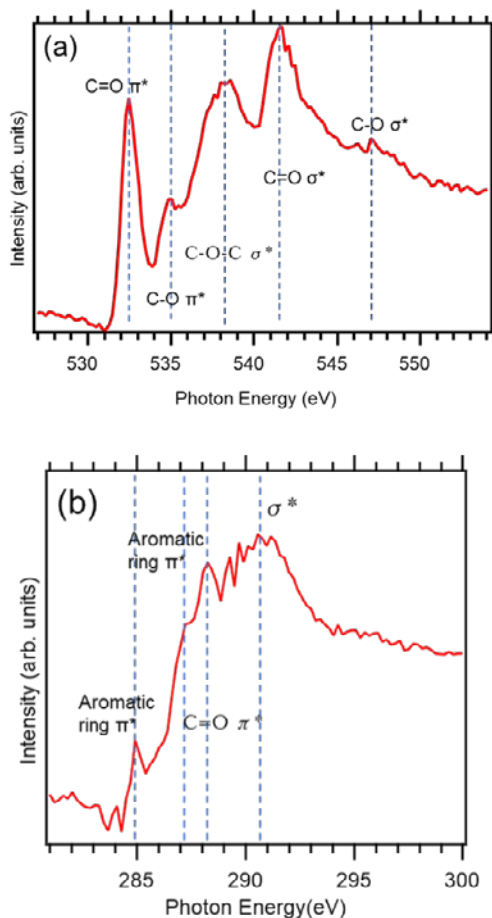


Fig. 5. X-ray absorption spectra of Γ -butyrolactone around (a) O K and (b) C K regions.

4. Conclusion

In this experiment, the following results were obtained by performing XAS measurements with the NewSUBARU BL9A using a modified simple liquid cell for SEM. First, the simple liquid cell is now applicable to XAS measurements of liquid and gaseous samples, which are considered difficult to measure with the NewSUBARU BL9A. Then, X-ray absorption spectra of aqueous ammonia boron solution and Γ -butyrolactone, which is not reported at present, were reported and their peaks were analyzed. In the future, we will expand the application of the simple liquid cell to X-ray emission spectroscopy (XES) and photoelectron emission microscopy (PEEM) in order to improve the accuracy of synchrotron radiation analysis at NewSUBARU BL9A.

References

- [1] S. Adachi et al., *The Japanese XAFS Society* (2017).
- [2] K. Takahara et al., *J. Appl. Phys.* **130**, (2021), 025302.
- [3] T. Tokushima, *Mol. Sci.* **9**, (2015), A0077.
- [4] T. Tokushima et al., *BUNSEKI KAGAKU* **64**, (2015), 237.
- [5] G. Pan et al., *Langmuir* **32**, (2016), 11133.
- [6] T. Fransson, Y. Harada et al., *ACS. Chem. Rev.* **116**, (2016), 7551.
- [7] J. A. Sellberg et al., *J. Chem. Phys.* **141**, (2014), 034507.
- [8] C. T. Chen et al., *Phys. Rev. A* **40**, (1989), 6737.
- [9] M. Morishita et al., *RCS Adv.* **11**, (2021), 14063.
- [10] T. Okajima, K. Teramoto et al., *J. Phys. Chem. A* **102**, (1998), 7093.
- [11] Y. Zubavichus, A. Shaporenko et al., *J. Phys. Chem. A* **109**, (2005), 6998.
- [12] F. Frati, M. O. J. Y. Hunault, et al., *Chem. Rev.* **120**, (2020), 4056.
- [13] T. Okajima *J. Surf. Sci. Soc. Jpn.* **23**, (2002), 359.
- [14] Yasuji Muramatsu, *Adv. X-Ray. Chem. Anal. Jpn.* **41**, (2010), 127.

In-situ XANES Measurements of the Heated Sugar for Clarifying the Melting Point Fluctuation

Kae Hiramatsu, Yasuji Muramatsu
Graduate School of Engineering, University of Hyogo

Abstract

To clarify the fluctuation of melting point (mp) in sugars, C *K* and O *K*-XANES measurements were performed while the sugar samples were heated from room temperature (RT) to 180 °C. The *in-situ* XANES spectra of heated sugar exhibited profile change dependent on heating temperature, which suggests thermal transformation of sugars. From theoretical XANES analysis using molecular dynamics (MD) and density functional theory (DFT) calculations, it is suggested that the thermal transformation of sucrose molecules depends on hydrogen bonds.

1. Introduction

Sugar consists of sucrose (C₁₂H₂₂O₁₁) molecule. Although commercially-available sugar is generally highly purified material, it usually takes a wide melting point (mp) range of 140–190 °C, depending on the sugar manufacturing process, purification methods, particle shape, and particle size. To clarify the mp fluctuation, we have measured X-ray absorption near-edge structure (XANES) in the C *K* and O *K* regions of various sugar samples [1]. It can be found that the 534.5 eV peak intensity in O *K*-XANES depends on mp. The 534.5 eV peak can be assigned to hydrogen bonds in water molecules [2]. Hence, it is suggested that hydrogen bonds formed in sucrose molecules affect the mp. To experimentally clarify the fluctuations of sugars, we have developed a sample heating system in the X-ray absorption analysis station in BL10 [3, 4].

In the present study, *in-situ* XANES measurements of sugars under heating were performed by using the heating system. In addition, theoretical XANES analysis was performed by using molecular dynamics (MD) and density functional theory (DFT) calculations to clarify the effect of hydrogen bonds in sugars.

2. Experiments and Calculations

2.1. X-ray Absorption Measurements

Granulated sugar with a melting point of 153 °C was used for X-ray absorption measurements. XANES spectra in the C *K* and O *K* regions were measured with a total electron yield (TEY) method while heating from room temperature to 180 °C. The base vacuum of the measurement chamber was 10⁻⁶ Pa. During heating up to 180 °C, the vacuum remained in the 10⁻⁵ Pa range. Hence *in-situ* XANES measurements of melted sugars under heating can be successfully performed.

2.2. MD and DFT Calculations

Calculation models of sucrose molecules were obtained with the molecular dynamics (MD)

calculations by using the MD code of Forcite on the Materials Studio platform (Dassault Systems). Initial conditions in the MD calculations were set to 30 molecules of sucrose with a temperature of 273 K and a density of 0.92 g/cm³. In the MD calculations, hydrogen bonds can be formed among the sucrose molecules. To simulate XANES of sucrose molecules, two-sucrose-molecules model forming intermolecular hydrogen bonds were extracted from the stable states in MD calculations. XANES simulations of the two-sucrose-molecules model were performed by using the DFT calculation code of CASTEP [5] on the Materials Studio platform. In a super cell, distance between cell walls and calculation model edge was set longer than 5 Å which is sufficiently longer than chemical bonds. After the calculations in the ground state and the excited state with a core hole in the C 1s or O 1s orbitals of each atom, calculated XANES spectra were obtained from transition probabilities.

3. Results and Discussion

3.1. *In-situ* XANES of Heated Sugars

Figure 1 shows the *in-situ* C *K*-XANES of sugars heated between RT–180 °C and references of sucrose, glucose, and fructose, which are normalized by the σ* peak intensity at 293.7 eV. In heated sugars, spectral differences dependent on heating temperature were clearly observed around 285 eV, 287.5 eV, and 289.2 eV. The peak at 285 eV can be assigned to π* peak of *sp*² carbons. Although sucrose molecules do not have *sp*² carbon, commercially available sugars generally contain minor amounts of reducing sugars, which includes *sp*² carbons. Therefore, the π* peak observed at RT was considered as the initial reducing sugar. Although there is little change in the π* peak intensity at RT and 120 °C, the peak intensity increased between 150–180 °C. This means that sucrose molecules are reduced by heating above mp.

The shoulder intensity at 287.5 eV (denoted by *a*) clearly decreased as the heating temperature

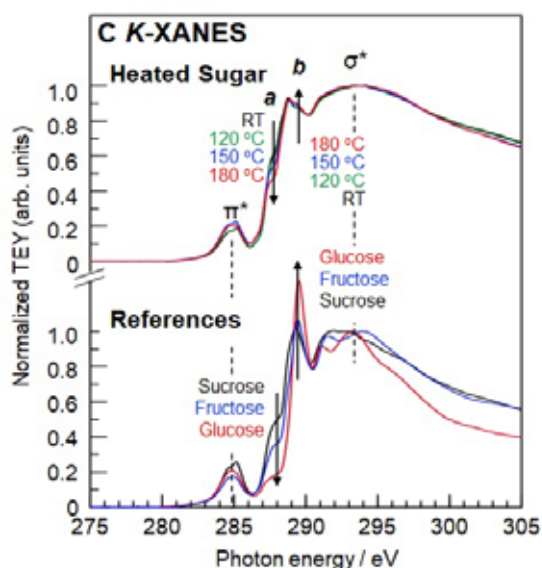


Fig. 1. *In-situ* C *K*-XANES of sugars heated between RT (27 °C)-180 °C and references.

increased between 150–180 °C. Additionally, the peak intensity at 289.2 eV (denoted by *b*) slightly increased as the heating temperature increased. It is well known that sucrose can be decomposed into glucose and fructose [6]. Compared to the reference compounds, reference compounds exhibit the shoulder at 287.5 eV, which corresponds to the shoulder *a* of heated sugars. The 287.5 eV shoulder intensity of sucrose is higher than that of fructose and glucose. Therefore, the decreased shoulder *a* intensity of heated sugars can be explained by the thermal decomposition of sugars (sucrose) into fragment molecules like glucose and fructose. The reference compounds also exhibit sharp peaks at 289.2 eV, corresponding to the peak *b* of heated sugars. The 289.2 eV peak intensity of sucrose is lower than that of glucose and fructose. Therefore, the increased peak *b* intensity of heated sugars can also be explained by the thermal decomposition of sugars into the molecules like glucose and fructose. It is therefore confirmed that the *in-situ* C *K*-XANES measurements can directly observe thermal transformations (decompositions) of sugars.

Figure 2 shows the *in-situ* O *K*-XANES of sugars heated at RT-180 °C and references of sucrose, glucose, and fructose, which are normalized by the σ^* peak intensity at 539.2 eV. The spectral differences depend on heating temperature were slightly observed around 533 eV and 545 eV. The peak at 533 eV was assigned to π^* peak of sp^2 oxygens. The π^* peak can be explained by carbonyl ($>C=O$) O atoms in partially contained reducing sugars, as mentioned above for the π^* peak in the C *K*-XANES. Although the change in the π^* peak intensity was negligible between RT–120 °C, the

peak intensity slightly increased between 150–180 °C. Such a π^* peak evolution, which depends on temperature in O *K*-XANES, corresponds to that in C *K*-XANES. It is therefore confirmed that sucrose molecules in sugars are partially reduced by heating above mp.

Spectral intensities near 545 eV decreased as the heating temperature increased from RT to 180 °C. Compared to the reference compounds, reference compounds exhibit shoulders near 533 eV, corresponding to the π^* peak. This suggests that the reference compounds partially contain reducing forms with carbonyl ($>C=O$) O atoms. Although σ^* peak can be observed near 538 eV in the reference compounds and sugars, sugars exhibit wider σ^* peak profile than reference compounds; Full width at half maximum (FWHM) of sugars is approximately 11 eV and that of the reference compounds is 8 eV. Especially, sugars exhibit the longer tailing to 545 eV. Such the broadening of XANES profile suggests intermolecular interactions of O atoms in sugars. Referring to the O *K*-XANES of water (H_2O) in gas, liquid, and solid phases [2], the observed σ^* peak broadening in 538 - 545 eV region of sugars can be explained by the formation of hydrogen bonds. Decrease of spectral intensities near 545 eV by heating can also be explained by decrease of hydrogen bonds in melted sugars than in solid sugars. This suggests that *in-situ* O *K*-XANES

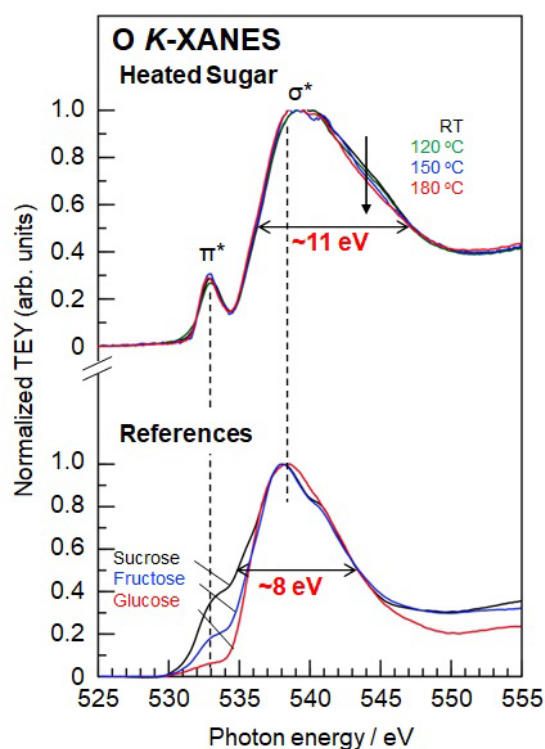


Fig. 2. *In-situ* O *K*-XANES of sugars heated between RT (27 °C)-180 °C and references.

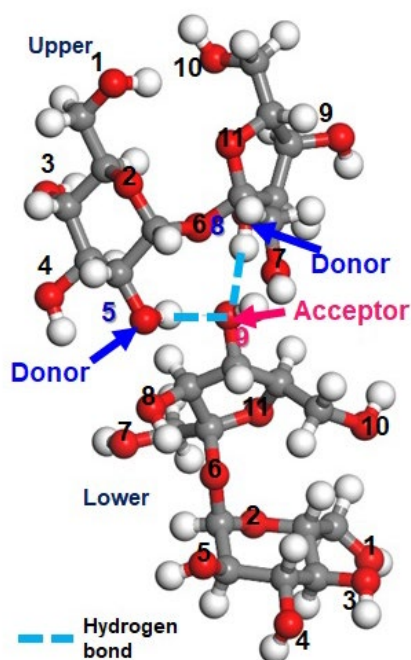


Fig. 3. Calculation model composed of two sucrose molecules, which was obtained from MD calculations.

measurements can observe thermal transformations of sugars, reflecting hydrogen bonds in sucrose molecules.

3.2. MD/DFT Calculations

Figure 3 shows the calculation model composed of two sucrose molecules, which was obtained from the MD calculations. In the model, O atoms numbered with 5 (denoted by 5O) and 8 (8O) in the upper sucrose molecule are donor atoms, and O atom numbered with 9 (9O) in the lower sucrose molecule is an acceptor atom forming hydrogen bonds. Figure 4 shows the calculated O *K*-XANES obtained from the CASTEP. Comparing the O atoms (5O, 8O, and 9O) forming hydrogen bonds to the other O atoms not forming hydrogen bonds, calculated XANES spectra of the upper 5O, 8O, and lower 9O exhibit the higher-energy shifts. Such the higher-energy shifts in O *K*-XANES correspond to the change in the σ^* peak width. This suggests that *in-situ* O *K*-XANES measurements can observe thermal transformations of sugars, reflecting hydrogen bonds in sucrose molecules.

4. Conclusions

The C *K*- and O *K*-XANES of sugars were successfully measured while heating between RT and 180 °C. From the C *K*-XANES, it can be suggested that reducing sugars are formed and sucrose molecules in sugars are decomposed into molecules like glucose and fructose by heating

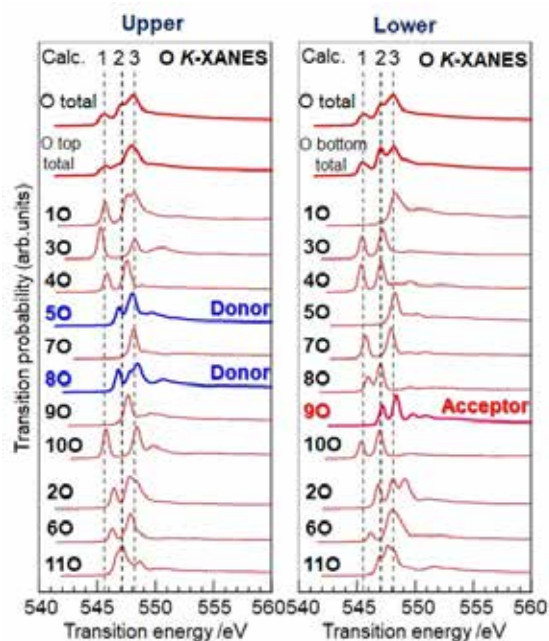


Fig. 4. Calculated O *K*-XANES spectra of the two-sucrose-molecules model, which were obtained from CASTEP.

around mp. From the O *K*-XANES, thermal transformations of sucrose molecules in sugars were observed, reflecting hydrogen bond transformations. XANES simulations by DFT calculations indicate that the O atoms forming hydrogen bonds between sucrose molecules exhibit a higher-energy shifted peaks. Such the calculations can well explain the spectral profiles of the O *K*-XANES of the heated sugars. It suggests that mp fluctuation of sugars depend on hydrogen bonds formed among sucrose molecules.

References

- [1] K. Maece and Y. Muramatsu, *LASTI Annual Report*, **21**, (2019) 57.
- [2] S. Myneni, Y. Luo, L. A. Näslund, M. Cavalleri, L. Ojamäe, H. Ogasawara, A. Pelmenchikov, P. Wernet, P. Väterlein, C. Heske, Z. Hussain, L. G. M. Pettersson, and A. Nilsson, *J. Phys. Condensed Matter*, **14**, (2002) L213.
- [3] K. Hiramatsu, K. Maece, T. Tanaka, R. Maruyama, T. Motokawa, and Y. Muramatsu, *LASTI Annual Report* **22**, (2020) 38.
- [4] Y. Muramatsu, K. Hiramatsu, K. Maece, and K. Sakamoto, *Anal. Sci.*, **38**, (2022) 717.
- [5] S. J. Clark, M. D. Segall, C. J. Pickard, P. J. Hasnip, M. I. J. Probert, K. Refson and M. C. Payne, *Krystallogr.*, **220**, (2015) 567.
- [6] M. Kamoda, *Proceedings of the Research Society of Japan Sugar Refineries' Technologists*, **9**, (1960) 158.

In-situ XANES Measurements of Eggs during Heating

Ikuya Shimogaki, Yasuji Muramatsu
Graduate School of Engineering, University of Hyogo

Abstract

To clarify the thermal denaturation of proteins, from the view point of chemical states, *in-situ* XANES in the C K, N K, and O K regions of heated egg yolk and egg white were measured in BL10. The egg samples were heated from room temperature to 180 °C under the vacuum of 10^{-5} Pa in a measurement chamber. Significant thermal changes were successfully observed in C K- and N K-XANES, but in O K-XANES. These results suggest the thermal transformation of carbon and nitrogen atoms in protein and lipid of egg yolk and white.

1. Introduction

Recently, a sample heating system was installed in the X-ray absorption spectroscopy (XAS) station at BL10, which enables to measure *in-situ* XAS spectra during sample heating up to 200 °C [1]. By using the heating system, we have observed thermal transformation of sugars around melting point [2]. To explore further target materials for chemical analysis dependent on heating temperature, we have focused on thermal denaturation of proteins.

Proteins are macromolecular compounds consisting of a large number of amino acids linked by peptide bonds. Proteins generally take complex conformations due to hydrogen bonds, disulfide bonds, and hydrophobic interactions. In addition, nonpolar side chains of amino acids aggregate inside the protein structure due to hydrophobic interactions, and hydrophilic side chains of amino acids hydrate with the solvent outside the structure. By heating, molecular structures of proteins drastically change. Intramolecular bonds such as hydrogen bonds are broken and the steric structure disintegrates. This is thermal denaturation of proteins. Such the structures result in thermal denaturation are unique and interesting. Although molecular structures in thermal denaturation of proteins have been commonly and widely analyzed by using X-ray diffraction method, the detailed structures and chemical transformations have not been well elucidated.

Hence, we have focused on thermal denaturation of proteins in egg yolk and white. In the present study, *in-situ* X-ray absorption near-edge spectra (XANES) in C K, N K, and O K regions of them were measured by using the heating system.

2. Experiments

Samples are commercially available egg yolk and white. Table 1 lists the general component of them. Main component of egg yolk are moisture, lipid, and protein, and of egg white is moisture and protein. Commercially available ovalbumin which is the main protein of egg white was also prepared for a reference sample.

XANES measurements were performed at the XAS chamber installed in BL10 with a total-electron-yield (TEY) method. In the sample heating system, samples are sandwiched between gold (Au) substrate and Au mesh (#100 mesh) cover, which are put on copper (Cu) sample plate. Liquid Egg yolk and white samples were hold between the Au-mesh and Au-plate substrate. Sample current of the egg samples can be detected through the Au-mesh/Au-plate and the Cu substrate. XANES spectra in the C K, N K, and O K regions were *in-situ* measured by heating from room temperature (RT) to 180°C. During heating, vacuum pressure of the XAS chamber was kept on 10^{-5} Pa.

3. Results and Discussion

Figure 1 shows C K -XANES of egg yolk and white, which were heated from RT to 180°C, with a reference ovalbumin. Egg yolk exhibits peaks at

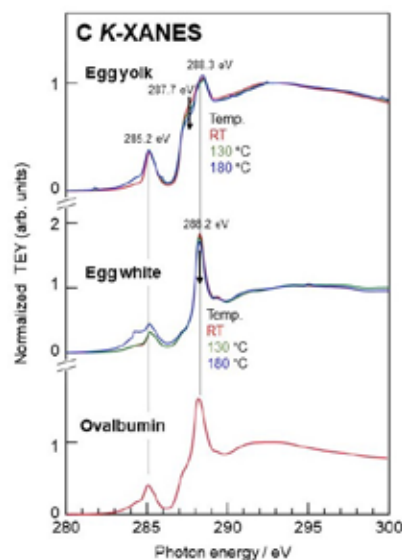


Fig. 1. C K-XANES of egg yolk and egg white heated from RT to 180 °C, compared to the reference ovalbumin.

Table 1 Component of eggs.

Component	Egg yolk	Egg white
moisture	49.6 %	88.3 %
protein	13.8 %	9.5 %
lipid	28.2 %	---
carbohydrate	6.7 %	1.6 %
Vitamin etc.	1.7 %	0.6 %

285.2 eV and 288.3 eV. Compared to ovalbumin, these peaks may be attributed similar structure of it. The shoulder intensity at 287.7 eV decreased as the heating temperature increased. As shown in Table 1, egg yolk contains lipid. Thus, the shoulder can be attributed unsaturated fatty acids, and thermal decomposition of lipid can be suggested in egg yolk. Spectral profile of egg white is as same as that of ovalbumin with the peaks at 285.2 eV and 288.2 eV. The 288.2-eV peak intensity of egg white slightly decreased as the heating temperature increased. This suggests the change in bonding states of peptide carbons by heating.

Figure 2 shows the N *K*-XANES of egg yolk, egg white, and ovalbumin. Egg yolk and white exhibit peaks at 401.6 eV and 406.4 eV, which correspond to the reference ovalbumin. Hence, nitrogen atoms in egg yolk and white take similar forms in ovalbumin. However, broad peak intensity near 412.0 eV in egg yolk and white increased as the heating temperature increased. Considering the

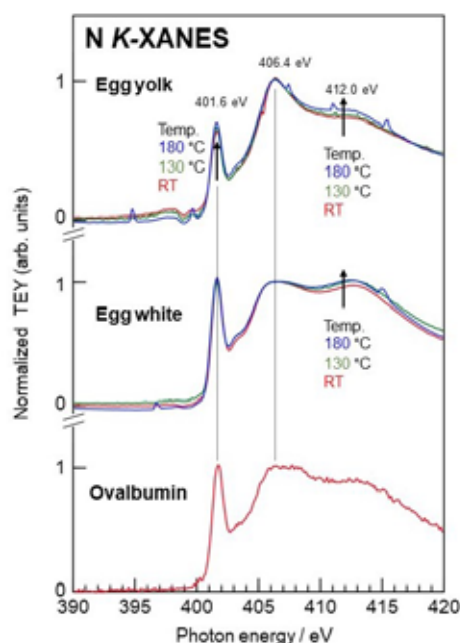


Fig. 2. N *K*-XANES of egg yolk and egg white heated from RT to 180 °C, compared to the reference ovalbumin.

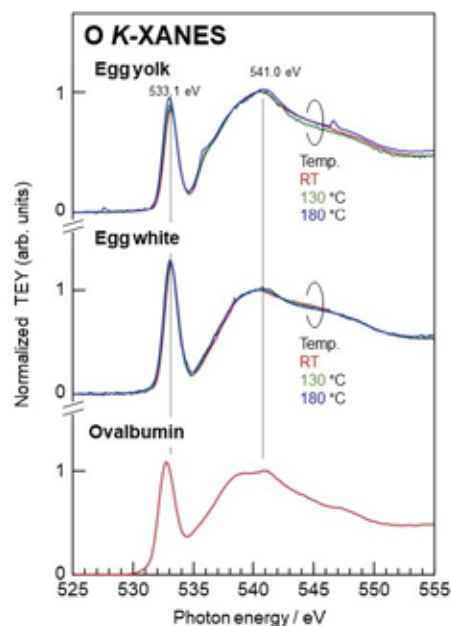


Fig. 3. O *K*-XANES of egg yolk and egg white heated from RT to 180 °C, compared to the reference ovalbumin.

lower 412.0-eV peak intensity in ovalbumin than in the egg yolk and white, the enhanced 412.0-eV peak may show the thermal transformation of peptide bonds in egg yolk and white.

Figure 3 shows the O *K*-XANES. Egg yolk and white exhibit two peaks at 533.1 eV and 541.0 eV, which can be attributed to π^* and σ^* peaks, respectively. This profile indicates the sp^2 -oxygen such as carbonyl oxygen (C=O), and is almost same as the reference ovalbumin. Hence oxygen atoms in egg yolk and white may arise from ovalbumin structure. Chemical states of oxygen may not change in thermal denaturation, because there is no significant profile change in egg yolk and white.

4. Conclusion

XANES spectra in the C *K*, N *K*, and O *K* regions of heated egg yolk and white were successfully observed by using the sample heating system in XAS chamber at BL10. These *in-situ* XANES observed thermal denaturation process of protein in eggs. Especially, thermal change in chemical states of carbon and nitrogen atoms in eggs are clearly observed. Such the *in-situ* XANES measurements will be a powerful tool to elucidate the thermal denaturation in proteins from the view point of chemical states.

References

- [1] Y. Muramatsu, K. Hiramatsu, K. Mae, and K. Sakamoto, *Anal. Sci.*, **38**, (2022).
- [2] K. Mae and Y. Muramatsu, *LASTI Annual Report* **21**, (2019) 57.

C *K*-XANES of Long-Chain Aliphatic Carbons Analyzed by the First Principles Calculations

Toshiyuki Tanaka, Yasuji Muramatsu
Graduate School of Engineering, University of Hyogo

Abstract

To clarify the σ^* peak structures in C *K*-XANES of carbon materials, C *K*-XANES spectra of various *n*-alkanes were measured in BL10/NewSUBARU, and the XANES profiles were theoretically simulated by the first principles calculations. Measured C *K*-XANES spectra exhibited two characteristic peaks near 288 eV. Incident-angle-dependent C *K*-XANES was also measured to confirm the molecular orientation. Considering the calculated XANES dependent on electric field vector directions, the measured *n*-alkanes are oriented perpendicular to the substrate plane.

1. Introduction

X-ray absorption near-edge structure (XANES) using synchrotron radiation (SR) has been utilized for electronic/chemical-state analysis of carbon materials. Additionally, theoretical XANES analysis has recently been performed using the first principles calculations. Hence, a combination of XANES measurements and theoretical analysis provides an advanced characterization method for carbon materials.

Graphitic carbons composed mainly of sp^2 -carbon (C) atoms generally exhibit characteristic π^* and σ^* peaks in C *K*-XANES. On the other hand, sp^3 -C atoms exhibit only σ^* peaks which take broader profiles composed of various chemical states of sp^3 -C structures. Although some characteristic σ^* peaks are attributed to typical functional groups, there is little theoretical analysis for the structures.

The present study aims to identify the broad σ^* peaks from the view point of local structures. The C *K*-XANES measurements of various *n*-alkanes and the theoretical XANES analysis by using the first principles calculations will be demonstrated.

2. XANES Measurements and Calculations

Table 1 shows the measured *n*-alkanes (C_nH_{2n+2}). These samples are commercially available powder compounds. Powder samples were pressed and held on an indium (In) substrate

Table 1 Measured compounds of *n*-alkanes.

Compound	Chemical formula
<i>n</i> -Eicosane	$C_{20}H_{42}$
<i>n</i> -Nonacosane	$C_{29}H_{60}$
<i>n</i> -Triacontane	$C_{30}H_{62}$
<i>n</i> -Hexatriacontane	$C_{36}H_{74}$
<i>n</i> -Pentacontane	$C_{50}H_{102}$

for XANES measurements. C *K*-XANES spectra of these samples were measured in BL10 at NewSUBARU by using a total-electron-yield (TEY) method.

XANES simulations were performed by using the DFT calculation package of CASTEP on the Materials Studio platform (Dassault Systems). Calculation models were constructed by using the coordinate data on the Cambridge Structural Database (CSD). Transition probabilities of individual C atoms in each model were obtained from CASTEP calculations in the ground-states and in the excited-states with C1s vacancies. After applying the transition energy correction, calculated XANES spectra were obtained by plotting the transition probabilities as the function of transition energies. To calculate the incident-angle-dependent XANES, electric field directions (E_a , E_b , E_c) for the **a**, **b**, and **c** axes on the molecular structure were specified in CASTEP calculations.

3. Results and Discussion

C *K*-XANES spectra of *n*-alkanes measured at a grazing angle (θ) of 90° (normal incidence) are shown in Figure 1. All molecules exhibited double peaks (denoted by **a** and **b**) around 288 eV and broad peaks around 293 eV. Relative intensities between peaks **a** and **b** are different among compounds, which may reflect the anisotropic structures. Figure 2 shows the incident-angle-dependent C *K*-XANES of *n*-alkanes. Intensities of the double peaks **a** and **b** around 288 eV decreased as the grazing angle become lower. This clearly shows the molecular orientation of the *n*-alkane samples pressed on the In substrates.

Figure 3 shows the calculated C *K*-XANES of the *n*- $C_{20}H_{42}$ crystal model varied by the specified electric field directions of E_a , E_b , and E_c , compared to the measured C *K*-XANES (normal incidence). The peaks **a** and **b** of the measured C *K*-XANES correspond to the calculated C *K*-

XANES peaks indicated by dotted lines in the figure. Additionally, the calculated peak intensity is clearly dependent on the electric field direction. Intensity of peak *b* is enhanced in E_a direction, that of peak *a* is in E_b direction. However, these peaks are not observed in E_c direction. In E_c

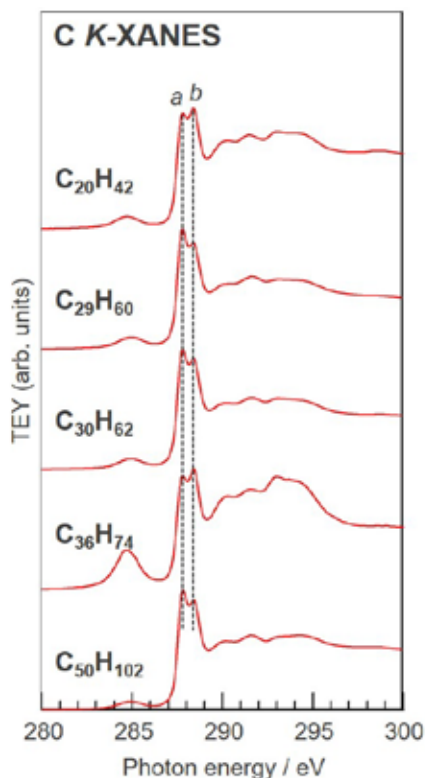


Fig. 1. Measured C K-XANES of *n*-alkanes.

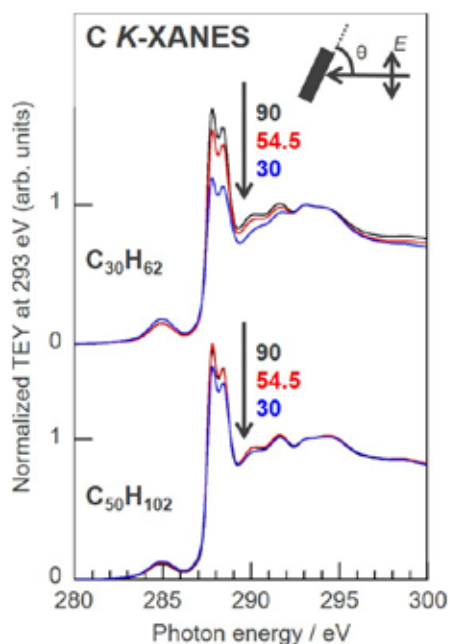


Fig. 2. Incident-angle-dependent C K-XANES of *n*-alkanes.

direction, electric field vector is parallel to the backbone chain of *n*-alkane molecule. Hence, the measured incident-angle-dependent C K-XANES suggests that the measured *n*-alkane samples are partially oriented perpendicular to the substrate plane.

4. Conclusion

To clarify the fine structures of the broad σ^* peak in C K-XANES of sp^3 -C materials, C K-XANES of various *n*-alkanes were measured and theoretically analyzed by CASTEP. The measured XANES spectra were reproduced by the band calculations of *n*-alkanes crystals, considering with the electric field direction. It can also be confirmed that the measured *n*-alkanes are partially oriented perpendicular to the substrate plane.

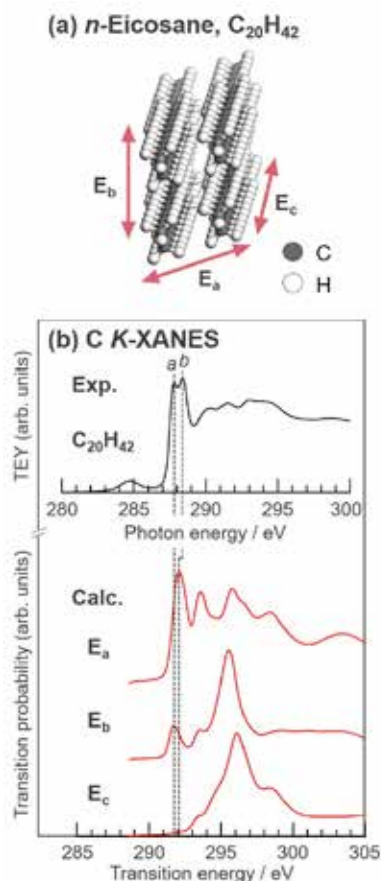


Fig. 3. Upper panel (a) shows the $C_{20}H_{42}$ crystal model. Lower (b) shows the calculated C K-XANES of the $C_{20}H_{42}$ crystal model, compared to the measured C K-XANES. Calculated XANES spectra are polarized in the electric field vectors of E_a , E_b , and E_c .

Fabrication of Ni-W Microgears Using LIGA Process

Kohzo Tamada¹, Sho Amano¹, Kana Okamoto², Masaya Takeuchi^{1,3},
Akinobu Yamaguchi¹, Yuichi Utsumi¹, Tohru Yamasaki²

¹Laboratory of Advanced Science and Technology for Industry, University of Hyogo,
3-1-2 Kouto, Kamigori, Ako-gun, Hyogo 678-1205, Japan

²Research Center for Advanced Metallic Materials, University of Hyogo,
2167 Shosha, Himeji, Hyogo 671-2280, Japan

³Graduate School of Engineering, University of Hyogo, 2167 Shosha, Himeji, Hyogo 671-2280, Japan

Abstract

Microgears made of Ni-W alloy that are expected to have high strength and ductility, i.e., high durability, were successfully fabricated by using the LIGA process with synchrotron radiation. Ni-W electrodeposited alloys have a Vickers hardness of about HV 600 and a tensile strength of about 2000 MPa or above for a sample thickness of up to about 20 μm . However, they lose their excellent mechanical properties with increasing sample thickness. For this reason, Ni-W electrodeposited alloys have not yet been used in the LIGA process for the fabrication of microcomponents. We consider that the decrease in strength is due to the increased electric resistance of the Ni-W film during the electrodeposition. To solve this problem, we developed a new process in which copper reversing mold are fabricated in the first step, then Ni-W alloy is electrodeposited on the copper reversing mold to prevent the electric resistance from increasing in the second step as the mold forming process. Using this process, microgears with reference diameters from 1000 to 80 μm were fabricated with high dimensional accuracy.

1. Introduction

Microturbines are an important component of microfluidic systems. Microgears have similar shapes to microturbines and are required to meet the increasing demand for ultrasmall motors in various fields, especially the medical field. Both microturbines and microgears are required to have high dimensional accuracy and high durability, but it is difficult for high dimensional accuracy on the order of microns to be achieved for metals in conventional machining. For example, the minimum reference diameter of gears in practical use is about 300 μm , and it is difficult to fabricate high-precision gears with a reference diameter of less than 300 μm [1].

On the other hand, the LIGA (an acronym for Lithographie, Galvanoformung und Abformung in German) process [2, Note1] using synchrotron radiation can be used to fabricate metallic components with a high aspect ratio and submicron-level dimensional accuracy. However, in the electroplating step of the LIGA process, only soft metals such as Ni and Cu can be deposited, and therefore it has been difficult to fabricate metallic micro-parts with high hardness and high durability. For example, Ni-Co electrodeposited alloy is a hard material with a Vickers hardness of HV 400, but a long time is generally required to deposit a thick layer of hard alloy plating owing to the low electrodeposition speed, and the layer may peel off from the substrate due to residual stress.

In this study, a Ni-W electrodeposited alloy [3-14] developed by Yamasaki and others, which

showed high strength and high ductility, has been applied to the LIGA process using synchrotron radiation to fabricate high-precision microgears with high durability. Ni-W electrodeposited alloys have nanocrystalline/amorphous composite structures with high plastic deformability despite their high strength. However, electrodeposited films of these alloys exhibit severe brittleness with increasing thickness. To solve this problem, we have developed a new process of double plating using a copper reversing mold. As a result, we succeeded in fabricating microgears made of Ni-W electrodeposited alloy with high plastic durability, and we evaluated their shape accuracy.

2. Materials and Methods

2.1. Double electroplating in LIGA process

In this study, a Ni-W alloy having about 17 at.% W with a Vickers hardness of about HV 600 and a tensile strength of about 2500 MPa was used as the electrodeposited alloy in the LIGA process. When the Ni-W alloy was directly deposited on an electrically insulating resist microstructure fabricated by lithography, the deposited alloy retained its high strength and ductility up to a thickness of about 20 μm . However, when the thickness exceeded 20 μm , the strength decreased due to embrittlement. This may be due to the increase in the electric resistance during the electrodeposition, i.e., the electric current flowed only from the Cu substrate (resistance of Cu $\sim 1.68 \times 10^{-8} \Omega \cdot \text{m}$) and the electric resistance increased

with increasing thickness of the electrodeposited Ni-W (resistance of Ni-W $\sim 7 \times 10^{-7} \Omega \cdot m$).

Thus, we developed a new process. As shown in Fig. 1, a metal reversing mold was made by electroforming copper sulfate in the first electroforming process, and then Ni-W electroforming was performed as the second electroforming in the mold forming process. In this process, because the current can flow not only through the substrate but also through the copper reversing mold, the increase in resistance can be prevented. We expected that high-strength Ni-W layers would be formed on the substrate and sidewall surfaces of a structure in the initial stage of electrodeposition, enabling the fabrication of high-strength microgears.

Figure 2 shows the results of tensile tests of micro-tensile specimens with a thickness of 60 μm produced by the double electroforming process, compared with those of specimens obtained by the conventional direct electroforming. As shown in Fig. 2, the nominal tensile strength of the directly deposited Ni-19 at.% W alloy is about 1600 MPa, while that of the alloy fabricated by the new process shown in Fig. 1 is about 2200 MPa. The ductility of the alloy fabricated by the double electroforming process was higher than that of the alloy fabricated by the conventional direct electroforming, and its strain was about twice as high. From these results, it was confirmed that the deposition of Ni-W on a copper reversing mold is effective for obtaining a film with about 20 μm thickness without any deterioration of its strength and ductility [8].

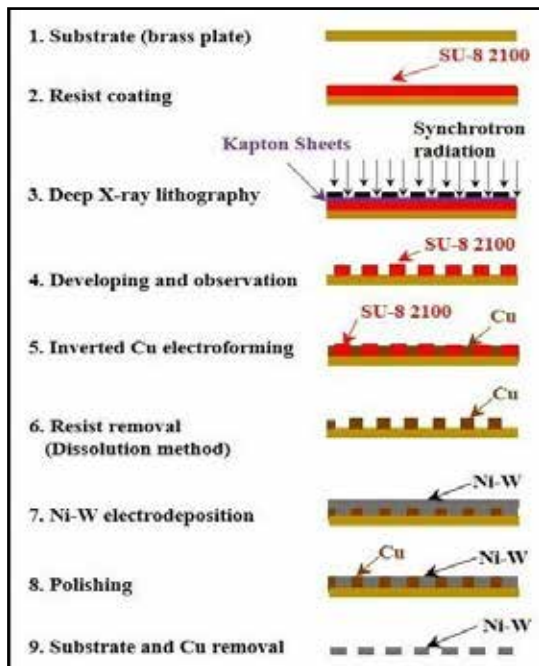


Fig. 1. Flowchart of production process of microgears.

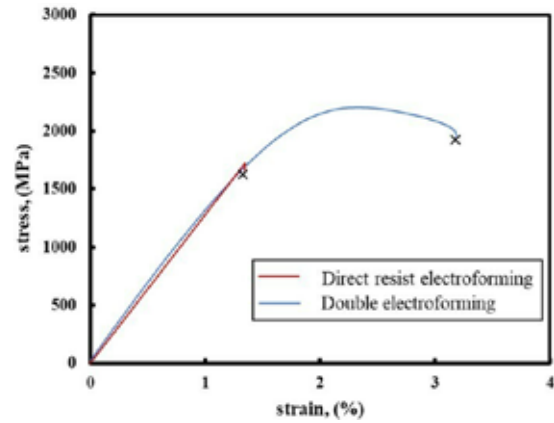


Fig. 2. Stress–strain curves obtained by tensile testing of micro-tensile specimens fabricated by direct resist electroforming and double electroforming.

2.2. Deep X-ray lithography

X-ray exposure for resist processing was performed at the LIGA beamline (BL11) of the New SUBARU synchrotron radiation facility of the University of Hyogo. The electron storage energy of New SUBARU is 1 GeV, the storage current is 300 mA, and X-rays of 2 to 6 keV are supplied [15]. The X-ray mask was a self-made membrane mask with Au as a light-shielding material. Resist processing was attempted with various gear patterns. Microgear inversion patterns were fabricated with four different numbers of gear teeth (12, 14, 17, and 24), twelve different reference diameters (80 to 1000 μm), and two pressure angles (20 and 25°). The addendum modification coefficient was 0, 0.05, 0.1, or 0.35. SU-8 2100 (Nippon Kayaku Co., Ltd.) was used as the resist, and it was applied on a brass substrate (YAMAMOTO-MS Co., Ltd.) with a thickness of about 100 μm using a spin coater. After the coating, the resist was preheated using a hot plate at 60 °C for 5 min, then at 75 °C for 2 h. A Kapton film (Du Pont-Toray Co., Ltd.) was sandwiched between the X-ray mask and the resist, and contact lithography was carried out. The resist sample was scanned at a speed of $v = 5$ mm/s during X-ray exposure to standardize the exposure intensity. The X-ray dose was set to 15 J/cm². After the exposure, the resist was postheated at 60 °C for 5 min and at 75 °C for 2 h. Next, the resist was immersed in SU-8 developer (Nippon Kayaku) to induce its reaction and produce the structure. Since SU-8 is a negative photoresist, the exposed area does not react and remains unchanged.

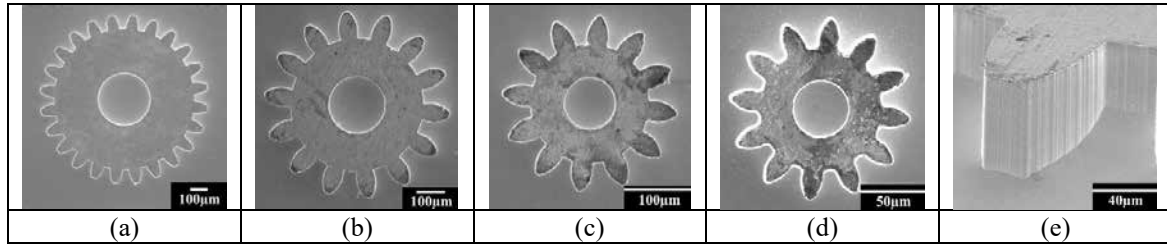


Fig. 3. SEM images of Ni-W microgears: (a) $\phi 1000 \mu\text{m}$, (b) $\phi 500 \mu\text{m}$, (c) $\phi 300 \mu\text{m}$, (d) $\phi 80 \mu\text{m}$, (e) enlargement of part of (b).

2.3. First electroforming

Copper sulfate was electrodeposited on the resist microgear structure formed by X-ray lithography as a primary electroforming. A copper reversing mold with a thickness of about $60 \mu\text{m}$ was fabricated in this electrodeposition. To prevent surface oxidation of the copper reversing mold, it was immersed in a discoloration inhibitor (Top Rinse CU-5, Okuno Chemical Industries Co., Ltd.) for 2 min, washed with water, and then quickly dried with a dryer. After that, the resist remaining on the mold was dissolved and removed using a remover. First, the substrate was immersed in Remover PG (Nippon Kayaku) at 70°C for 2 h to swell the resist, and then it was washed with water. Next, the resist was stripped in a 1:1 mixture of Remover K (Parts A and B) (Nippon Kayaku) at 70°C for 1 h and rinsed twice. Finally, it was neutralized with Neutralizer K (Nippon Kayaku) and rinsed with water and dried with ethanol.

2.4. Second electroforming (replication)

Microgears were fabricated by Ni-W electrodeposition on a copper reversing mold as a secondary electroforming. The plating solution was

a mixture of nickel sulfate and sodium tungstate, with citric acid and ammonium sulfate added as complexing agents. An Ir-Ta mesh was used as an anode plate on the resist-removed brass substrate.^(4,7) In addition, the brushing technique proposed by Nakayama *et al.* was applied, which can suppress the generation of voids and pits due to hydrogen bubbles.^(4,8) The plating time was adjusted so that the film thickness was approximately $100 \mu\text{m}$. The electrodeposited Ni-W microgears were immersed in HNO_3 solution to separate from the brass substrate and the copper reversing mold [4].

3. Reproducibility

Scanning electron microscopy (SEM; VE-7800, Keyence Corporation) was used to observe the fabricated Ni-W alloy microgears. The acceleration voltage was 10 kV. Figure 3 shows SEM images of microgears having diameters of 1000, 500, 300, and $80 \mu\text{m}$. These images show that microgears with a fine metallic luster could be fabricated in accordance with the designed mask pattern. Their thicknesses were measured to be about $60 \mu\text{m}$.

From the SEM images of Figs. 3(a)–3(d), the tooth tip diameter, reference circle diameter, and

Table 1. Shape evaluation of Ni-W microgears: (a) $\phi 1000 \mu\text{m}$, (b) $\phi 500 \mu\text{m}$, (c) $\phi 300 \mu\text{m}$, (d) $\phi 80 \mu\text{m}$.

	(a)		(b)		(c)		(d)	
	CAD dimensions (μm)	Average value (μm)	CAD dimensions (μm)	Average value (μm)	CAD dimensions (μm)	Average value (μm)	CAD dimensions (μm)	Average value (μm)
Tip diameter	1075	1041	583	556	350	340	94	87
Reference diameter	1000	966	500	479	300	291	80	75
Inside diameter	333	322	167	164	100	98	26	24
Shape error	3.3%		3.5%		2.6%		7.1%	

inner circle diameter were measured at three different locations, and their average values were calculated and compared with the CAD dimensions to obtain the shape error. The results are shown in Table 1. From the results, we conclude that microgears can be fabricated with accuracies of several percent by this process.

4. Summary

We succeeded in fabricating microgears made of Ni-W electrodeposited alloy using the LIGA process. We developed a new double plating method that involved the production of a copper reversing mold. The Ni-W electrodeposited alloy is expected to enable the production of highly durable precision microgears with a Vickers hardness of about HV 600 and a tensile breaking strength of about 2200 MPa because of its high strength and high ductility. The results of this study are summarized below.

(1) Microgears with a maximum reference diameter of 1000 μm and a minimum diameter of 80 μm were fabricated.

(2) As in table 1, the shape size error between the design and the fabricated microgears was evaluated to be several percent.

We are planning to clarify the material properties (composition, crystallite size, and hardness) of the gears and conduct dynamic property tests (wear and endurance tests) on interlocked gears to demonstrate their use as highly durable microgears. Using the same technology, a highly durable microturbine can be realized, and it will contribute to further research on microfluidics.

Note 1: The LIGA process was developed at Karlsruhe Nuclear Research Center (now Karlsruhe Institute of Technology) in Germany in the 1970s to fabricate micro-metallic mechanical parts, which are the components of micro-mechanisms. The LIGA process consists of three step: lithography (Lithographie), electroplating (Galvanoformung), and molding (Abformung). After the fabrication of a polymer (resist) microstructure by lithography, a mold is fabricated by electroplating. In the molding process, various materials such as resins, metals, and ceramics are processed to replicate the microstructures of the mold. This technology attracted worldwide attention in the 1990s as a completely new microfabrication technique. However, this technique is not yet in widespread use due to the lack of electrodeposited alloys with sufficient strength to be used as metal micro-parts.

References

- [1] Y. Kitakoga: *Int. J. Jpn. Soc. Precis. Eng.* **58** (1992) 1284 (in Japanese).
- [2] N. Nakajima and A. Umeda: *Advanced Machining Technology & Development Association: LIGA Process - Advancing Three-Dimensional Ultrafine Machining Technology* (Nikkan Kogyo Shimbun, 1998) pp. 89-97 (in Japanese).
- [3] T. Yamasaki, M. Yamada, H. Adachi, T. Nabeshima, and Y. Yokoyama: *Microsyst. Technol.* **20** (2014) 1941.
- [4] S. Nakayama, H. Adachi, T. Nabeshima, T. Miyazawa, and T. Yamasaki: *Sci. Adv. Mater.* **8** (2016) 2082.
- [5] T. Yamasaki, M. Sonobe, and H. Yokoyama: *Mater. Sci. Forum* **561-565** (2008) 1295.
- [6] H. Hosokawa, T. Yamasaki, N. Sugamoto, M. Tomizawa, K. Shimojima, and M. Mabuchi: *Mater. Trans.* **48-5** (2004) 1807.
- [7] T. Yamasaki: *Scr. Mater.* **44** (2001) 1497.
- [8] S. Nakayama, H. Adachi, and T. Yamasaki: *J. Alloys Compd.* **643** (2015) S22.
- [9] K. Fujita, K. Nagaoka, T. Suidu, T. Nabeshima, and T. Yamasaki: *J. Jpn. Inst. Met. Mater.* **77** (2013) 192 (in Japanese).
- [10] K. Fujita, T. Suidu, and T. Yamasaki: *J. Japan Inst. Metals* **75** (2011) 348 (in Japanese).
- [11] H. Yokoyama, T. Yamasaki, T. Kikuchi, and T. Fukami: *Mater. Sci. Forum* **561-565** (2007) 1295.
- [12] N. Oda, H. Matsuoka, T. Yamasaki, and T. Fukami: *J. Metastable Nanocryst. Mater.* **24-25** (2005) 411.
- [13] T. Nasu, M. Sakurai, T. Kamiyama, T. Usuki, O. Uemura, K. Tokumitsu, and T. Yamasaki: *Mater. Sci. Eng., A* **375-377** (2004) 163.
- [14] A. S. M. A. Haseeb: *Microsyst. Technol.* **14** (2008) 379.
- [15] M. Takeuchi, A. Yamaguchi, and Y. Utsumi: *J. Synchrotron Radiat.* **26** (2019) 528.

Fabrication of Free-form Shape Using LIGA Process with Independently Moving X-Ray Mask

Taki Watanabe, Sho Amano, Akinobu Yamaguchi, Yuichi Utsumi

*Laboratory of Advanced Science and Technology for Industry, University of Hyogo,
3-1-2 Kouto, Kamigori, Ako-gun, Hyogo 678-1205, Japan*

Abstract

Due to its characteristics, the LIGA process is good at machining high aspect ratio structures on surfaces with good verticality and low surface roughness. However, processing of shapes that depend on the two-dimensional pattern of the X-ray mask used has been mainly performed. In this study, we attempted to process a microstructure of a micron-order three-dimensional Free-Form shape on the PMMA surface by using a high-precision moving mask using a piezo actuator. We are also aiming to establish a LIGA process for making micro molds by electroforming on the PMMA surface and manufacturing resin parts by injection molding. In the experiment with NewSUBARU BL11, we succeeded in processing a conical shape with a lower end diameter of 63 μm , an upper end diameter of 2 μm , and a height of about 70 μm by exposing the sample while moving the sample by controlling the piezo actuator.

1. Introduction

The LIGA process is a processing technique that combines fine pattern formation by deep X-ray lithography using synchrotron radiation, mold fabrication by electroforming, and precision molding by mold. The LIGA process features a minimum dimension of sub μm (currently 0.2 μm) and a maximum height of 1 mm or more by deep X-ray lithography that utilizes the characteristics of soft X-ray transmission of 4.0 KeV or more and highly directional x-ray. It is possible to fabricate a structure having a high aspect ratio of (currently 3 mm), and the surface roughness of the side wall of the structure is on the order of several tens of nm, which is a mirror surface state. Taking advantage of these characteristics, deep X-ray lithography of a resist has been conventionally performed along a fine pattern of an absorber that shields soft X-rays. Therefore, in this study, we have developed a method for processing a Free-Form three-dimensional structure on the sample surface using a moving mask using a piezo actuator, which does not depend on the pattern of the soft X-ray mask.

2. Experiments

2.1. Mechanism of the Moving Mask

In order to process a shape that does not depend on the pattern of the X-ray mask, it is necessary to move the X-ray mask relative to the exposed sample to continuously change the exposed portion. To that end, we have developed our own moving mask device. The moving mask device developed in the exposure chamber was installed at the beamline dedicated to the LIGA process, New SUBARU BL11, University of Hyogo. By moving the exposure stage up and down, the dose amount of the entire sample surface is made uniform. During that

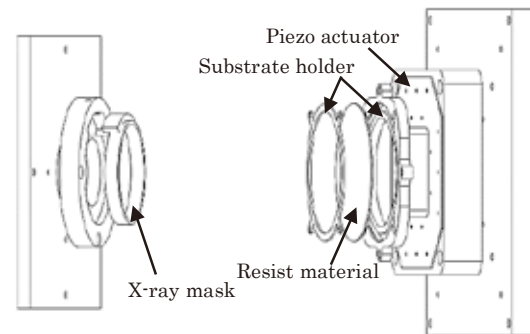


Fig. 1. Outline of moving mask.

time, the operation of the piezo actuator creates an dose amount distribution only in the pattern portion, and processes a Free-Form shape. Piezo actuator to use Since the actuator has an operating range of 200 μm up, down, left and right, and the operation reproducibility is 10 nm, it is possible to control the moving mask with extremely accurate operation. Fig. 1 shows the outline of the moving mask device.

The X-ray mask and the exposed sample were mechanically fixed to realize a moving mask. Soft X-rays are incident from the left hand of Fig. 1 and are patterned by an X-ray mask. Then, the surface of the exposed sample fixed to the piezo actuator is irradiated, and deep X-ray lithography is performed. By sandwiching the spacer, a gap of 500 to 1000 μm can be created between the portion that holds the X-ray mask and the portion that holds the exposed sample. As a result, it is possible to expose an exposed sample having a thickness in the range of 0 to 1000 μm with a moving mask.

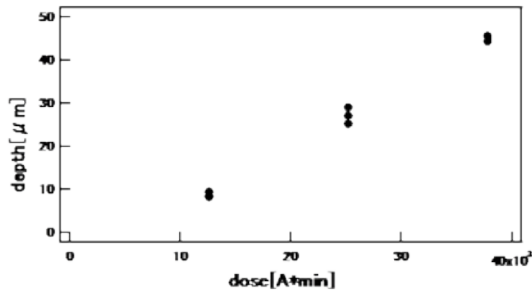


Fig. 2. Exposure rate:
Development time = 360 min.

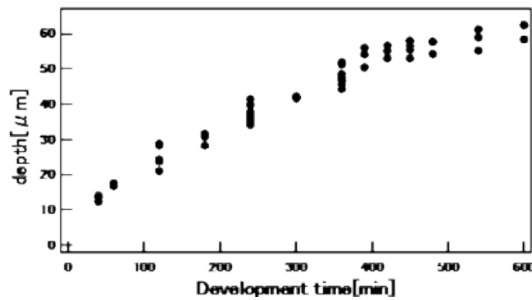


Fig. 3. Development rate:
(dose = 37800[A*min], 37.8°C).

depending on the dose amount, this was

Table 1. Ingredient of G-G developer.

Parameter	Vol%
2-(2-n-butoxy-ethoxy)ethanol	60
Tetrahydro-1, 4-oxazine	20
2-amino-ethanol-1	5
D. I. Water	15

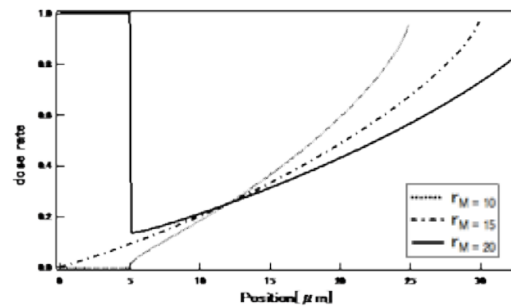


Fig. 4. Calculation results: r_M , Radius of circular motion.

2.2. Resist Materials

Synchrotron radiation is characterized by high intensity and small divergence angle. Therefore, PMMA is generally used as a resist material because of its good resolution. In this study as well, experiments were conducted using PMMA as the resist material. After irradiating PMMA with soft X-rays, development is performed using a developer. At that time, since the processing depth changes with the developer, the presence or absence of stirring, and the like. It is necessary to continue to develop a development method according to the pattern.

2.3. Dose distribution Calculation

Machining simulation is indispensable for machining fine 3D structures in this research. Here, the exposure amount distribution when the sample

is investigated. In addition, since the processing depth changes depending on the length of the developing time, the same investigation as in s was conducted. The exposure characteristics and development characteristics are shown in Fig. 2 and Fig. 3.

We used, G-G developer for development. Table 1 shows the ingredients. The development result of PMMA varies greatly depending on the exposure condition of the sample, the temperature of the sample, and the like. The amount of exposure when the circular motion was performed while changing the radius was calculated. Fig.4 shows the calculation results. The calculation formula is as follows.



Fig. 5. Output shape:
 $r_m=17 \mu\text{m}$, $r_M=16.2\mu\text{m}$

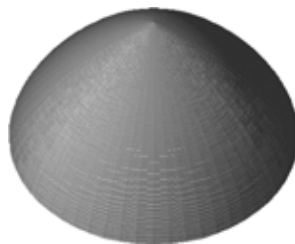


Fig. 6. Output shape:
 $r_m=15 \mu\text{m}$, $r_M=16.2$



Fig. 7. Output shape:
 $r_m=10 \mu\text{m}$, $r_M=16.2 \mu\text{m}$.

Table 2. Experimental conditions.

Resist material	PMMA
thickness [μm]	200
dose [$\text{A}\cdot\text{min}$]	37800
Developing time [min]	360
Developing degrees [$^{\circ}\text{C}$]	37.8
developer	G-G developer

$$E = 1 - \frac{1}{\pi} \arccos \left(\frac{r^2 + r_M^2 - r_m^2}{2r_M \cdot r} \right)$$

Here, E is the X-ray exposure energy at the distance r from the drive center, r_m is the radius of the X-ray mask absorber, and r is the distance from the drive center. From this calculation result, the processed shape of PMMA based only on the exposure amount was output. The results are shown in Fig. 5, Fig. 6, and Fig. 7.

2.4. Exposure experiments

An exposure experiment using the developed moving mask device was conducted at New SUBARU BL11, University of Hyogo. Table 2 shows the experimental conditions.

After the exposure experiment with synchrotron radiation X-rays, the development work was performed using a G-G developer. At the time of development, stirring was performed using a rotary blade to circulate the developer in detail. The rotation speed is 120 rpm.

Fig.8, Fig.9, and Fig.10 show the experimental results for each operating parameter. The pattern in Fig.8 was very different from the simulation, and the result was that a large hole was formed in the center. The pattern in Fig.9 was almost the same as the simulation, and the shape was as designed. The pattern in Fig.10 has a shape close to that of the simulation, although the angle of the wall surface is slightly different.

The reason why the shape differs from the simulation is that there is a gradient of the development speed depending on the dose amount. This is remarkable in the pattern of Fig.8. The hole in the central part was in a state where synchrotron radiation X-rays overlapped and was constantly irradiated, and a part that was developed early and a part that was developed late at the time of development were adjacent to each other. Therefore, it is considered that the depressed portion in the

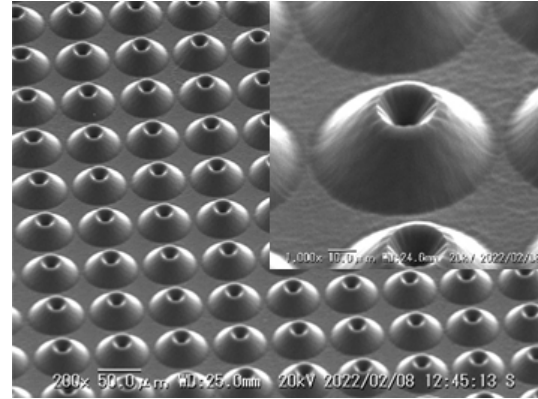


Fig. 8. Developed PMMA: $r_m=17 \mu\text{m}$, $r_M=16.2 \mu\text{m}$.

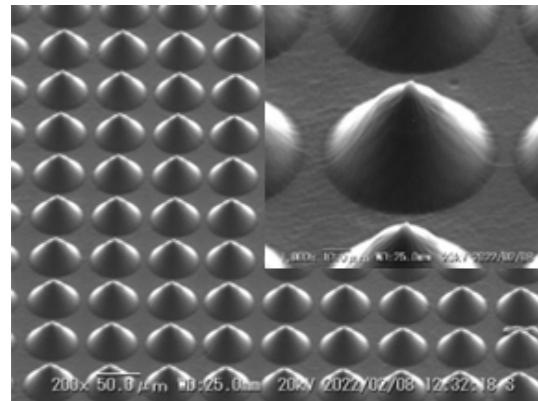


Fig. 9. Developed PMMA: $r_m=15 \mu\text{m}$, $r_M=16.2 \mu\text{m}$.

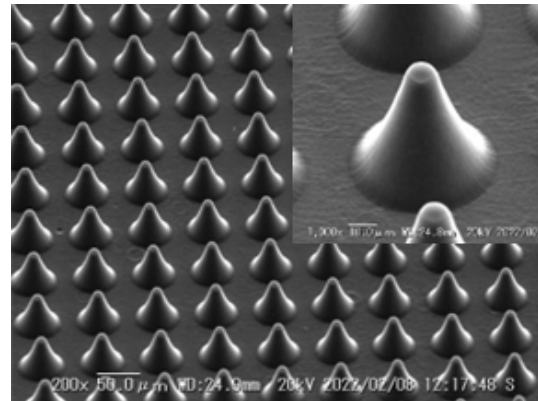


Fig. 10. Output shape: $r_m=10 \mu\text{m}$, $r_M=16.2 \mu\text{m}$.

center was developed quickly, and the development proceeded in the lateral direction from that portion. Therefore, it can be inferred that the shape did not match the simulation.

3. Summary and conclusion

In the LIGA process, deep X-ray lithography of resists that depend on the pattern of the X-ray mask has been conventionally performed. Therefore, in

II

this study, we aimed to manufacture a three-dimensional microstructure by moving the X-ray mask and the resist material relatively, and moving the resist while irradiating the resist surface with X-rays patterned by the X-ray mask. An exposure experiment was conducted using PMMA as a resist material using the moving mask device we invented and the New SUBARU BL11 of the University of Hyogo. As a result, depending on the pattern to be manufactured, it was possible to process it into a shape very close to the simulation, but some results were significantly different. This is because the development speed differs depending on the dose amount and the development is not uniform. A future task is to reflect the development characteristics in the simulation and complete a more advanced machining simulation. In addition, we aim to develop a nebulizer filter that applies the LIGA process using the moving mask device developed this time.

References

- [1] T. Chuang, T. Fang, M. Jiang, W. Lei, B. Shew, and C. Fu, *J. Micromech. Microeng.* **22** (2012) 085027.
- [2] K. W.-C. Lee, S. S. Lee, *Sens. Actuator A Phys.* **108** (2003) 121-127.
- [3] O. tabata, H. You, N. Matsuzuka, T. Yamaji, S. Uemura, I. Dama, *Microsyst. Technol.* **8** (2002) 93.
- [4] C.-M. Cheng, R.-H. Chen: *J. Micromech. Microeng.*, **11** (2001) 692.
- [5] M. Takeuchi, A. Yamaguchi, Y. Utsumi, *J. Synchrotron Rad.* **26** (2019) 528.

Deviation of Photoelectron Intensity from the Lambert-Beer's Law in Near-Ambient Pressure Hard X-Ray Photoelectron Spectroscopy

Kento Takenaka¹, Nanami Hosoe¹, Koji Takahara², Tomoaki Eguchi², Hirosuke Sumida³, Satoru Suzuki²
¹Graduate School of Science, University of Hyogo, ²LASTI, University of Hyogo, ³Mazda Motor Corp.

Abstract

In attempts to eliminate charging by introducing gas at near-ambient pressure hard X-ray photoemission spectroscopy (NAP-HAXPES), it was found that the effect was greater when the distance d between the sample surface and the aperture cone was longer. In this study we measured NAP-HAXPES spectra at various distance d gas (N₂ or Ar) pressures using an Au plate as a sample to investigate the pressure dependence of the photoelectron intensity. The spectral intensity was found to decrease exponentially with pressure. The measurement results follow $I/I_0 = \exp \{-\sigma P(d+d_0)/kBT\}$. It is thought that d_0 is necessary because gas remains inside the cone of the electron energy analyzer and photoelectron attenuation is occurring not only outside the cone but also inside.

1. Introduction

Recently, near-ambient pressure (NAP) photoelectron spectroscopy equipped with differential pumping system has become popular. It enables us to study chemical reactions in a gas atmosphere. It is also useful for removing or reducing the charging effect of insulating samples owing to the environmental charge compensation [1-3]. In a NAP photoelectron spectroscopy apparatus, the aperture cone of an electron energy analyzer also acts as a nozzle of a differential pumping system in addition to collecting photoelectrons. Under a gas pressure, attenuation of photoelectron intensity due to scattering by gas molecules becomes severe. Therefore, the aperture cone is normally placed as close as possible to the sample within the range that does not cause a pressure drop on the sample surface. Very recently however, we showed that the larger the distance d between the sample surface and the aperture cone, the more pronounced the environmental charge compensation effect in NAP hard X-ray photoelectron spectroscopy (HAXPES) [4]. Here, we systematically studied the pressure dependence of photoelectron intensity at various d value. Formal deviation of photoelectron intensity from the Lambert-Beer's law was observed.

2. Experiments

Measurements were performed at the beamline BL24XU, SPring-8, using a HAXPES apparatus equipped with the HiPP-2 electron energy analyzer (Scienta Omicron) shown in Fig 1. at $h\nu = 8$ keV. The diameter Φ of the aperture cone was 0.3 mm. The HAXPES apparatus was mounted on a stepping motor-controlled mobile stage. The d value was changed by moving the stage, as schematically shown in Fig 2. The Au 3d and 4f photoelectron intensities were measured at various d values and gas (N₂ or Ar) pressures, using an Au plate as a

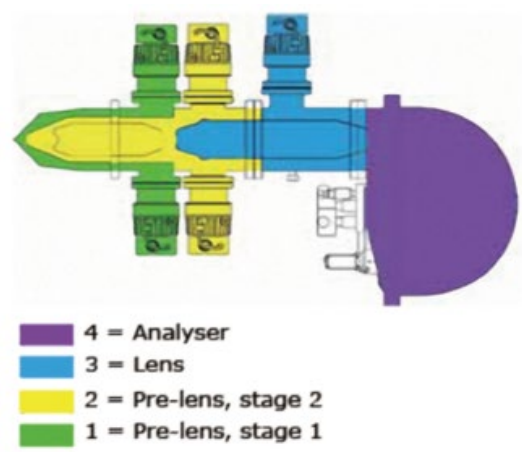


Fig 1. Schematic diagram of HiPP-2 [5].

sample.

3. Results and discussion

The attenuation of electrons passing through a gaseous atmosphere is considered to follow Lambert-Beer's law as shown below [6, 7].

$$I/I_0 = \exp(-\sigma P d / kBT) \quad (1)$$

where I and I_0 are photoelectron intensity at a certain pressure and a vacuum, σ is electron scattering cross section, kB , the Boltzmann constant, and T , temperature. Fig 3 shows the decrease in photoelectron intensity due to gas for each distance d . The larger the distance d , the greater the decrease in photoelectron intensity due to the gas. Also, $\ln(I/I_0)$ decreases linearly with gas pressure P at each distance d . The slope of the plot gives σd .

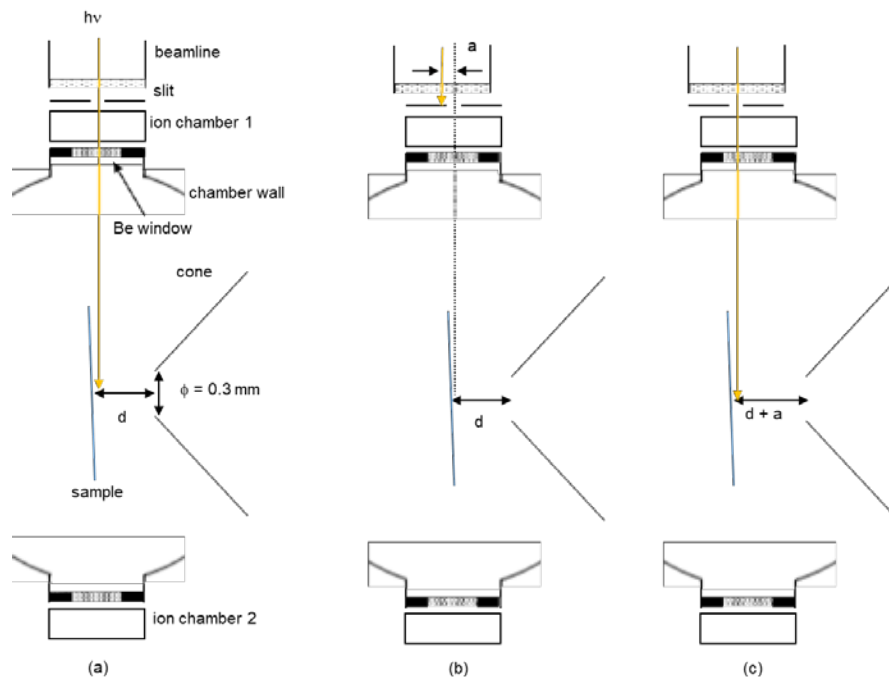


Fig 2. (a) Schematic of the beamline and analysis chamber (top view) in the initial state. (b) The analysis chamber with the slit and ion chambers was moved to the right by a distance a . (c) Measurement arrangement after the movement. The slit and sample surface are on the beam axis again, by moving them to the left by a distance a .

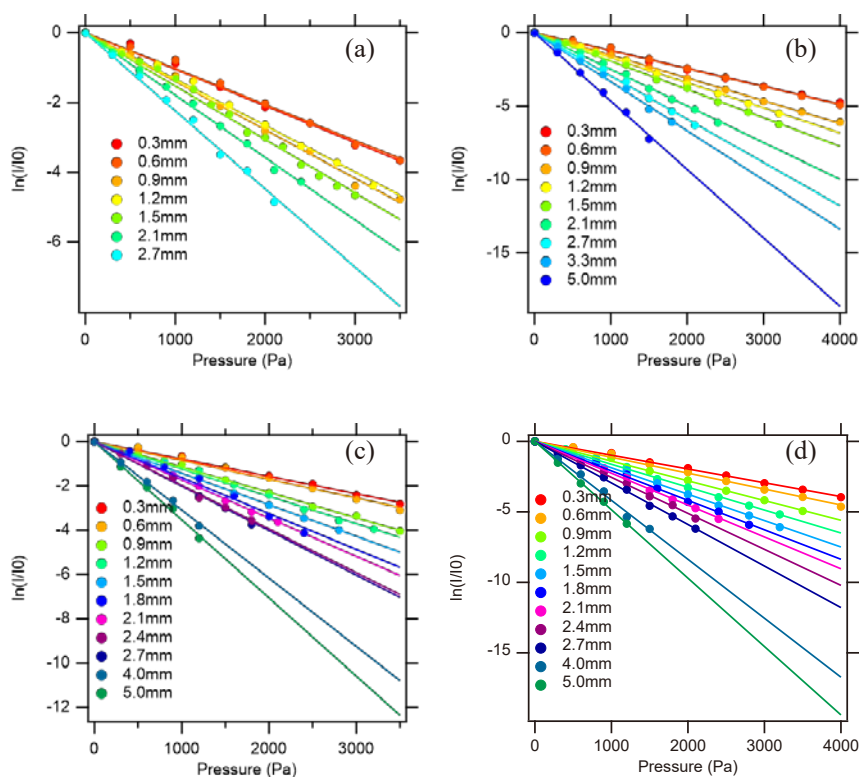


Fig 3. (a) N_2 gas pressure dependence of the relative intensity of the Au $4f$ peak for each distance d . (b) N_2 gas pressure dependence of the relative intensity of the Au $3d$ peak for each distance d . (c) Ar gas pressure dependence of the relative intensity of the Au $4f$ peak for each distance d . (d) Ar gas pressure dependence of the relative intensity of the Au $3d$ peak for each distance d .

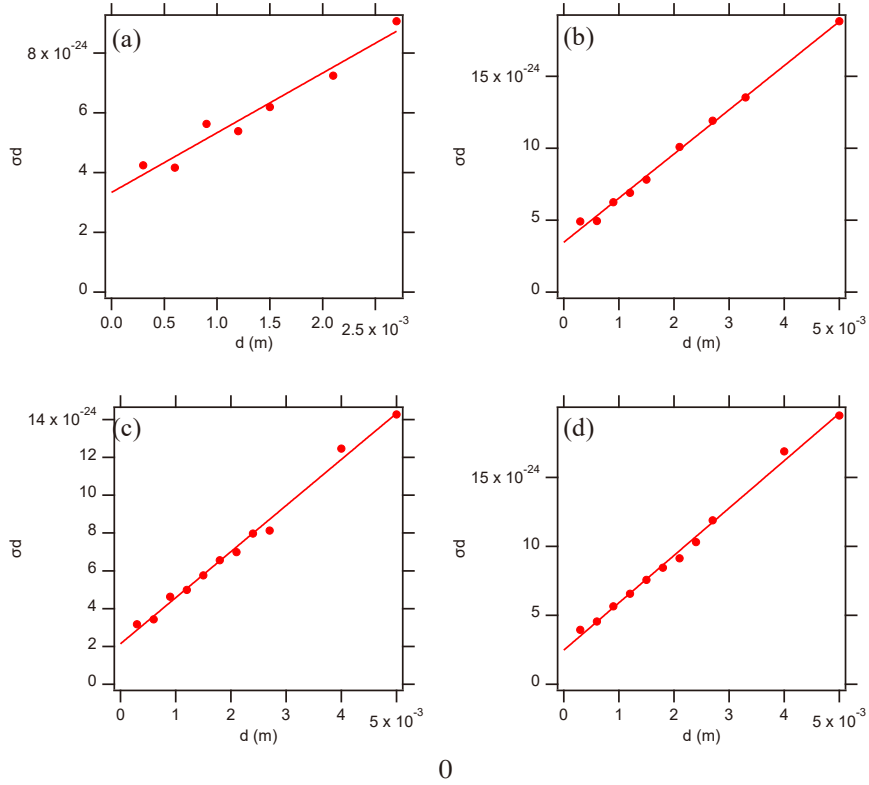


Fig 4. (a) σd vs d obtained from Au $4f$ photoelectron intensity in N_2 gas. (b) σd vs d obtained from Au $3d$ photoelectron intensity in N_2 gas. (c) σd vs d obtained from Au $4f$ photoelectron intensity in Ar gas. (d) σd vs d obtained from Au $3d$ photoelectron intensity in Ar gas.

Fig. 4 shows the obtained σd plotted against d . Unexpectedly however, the σd - d line does not pass through the origin. This means that, to reproduce the experimental result, d in eq. (1) needs to be formally replaced by $d+d_0$ (d_0 is a constant).

$$I/I_0 = \exp \{-\sigma P(d+d_0)/k_B T\} \quad (2)$$

Deriving σ and d_0 from eq.(2), $\sigma = 2.0 \times 10^{-21} \text{ m}^2$, $d_0 = 1.7 \times 10^{-3} \text{ m}$ for Au $4f$ (7.91 keV) and $\sigma = 3.1 \times 10^{-21} \text{ m}^2$, $d_0 = 1.1 \times 10^{-3} \text{ m}$ for Au $3d$ (5.91 keV) for N_2 gas and $\sigma = 2.4 \times 10^{-21} \text{ m}^2$, $d_0 = 8.8 \times 10^{-4} \text{ m}$ for Au $4f$ and $\sigma = 3.4 \times 10^{-21} \text{ m}^2$, $d_0 = 7.2 \times 10^{-4} \text{ m}$ for Au $3d$ for Ar gas. These values of σ are close to the literature value for electron scattering cross sections ($\sim 2.0 \times 10^{-21} \text{ m}^2$) [8].

There are two possible reasons for the appearance of d_0 . The first is that the path of photoelectrons is not the shortest distance d . Fig 5 shows the relationship between angular acceptance of the electron energy analyzer θ and the photoelectron pathway. The longest distance d' that can be taken as the path of a photoelectron is expressed by $d' = d/\cos\theta$. The angular acceptance of HiPP-2 is 26° ($\theta = \pm 13^\circ$) [5], which gives $d' = d/\cos 13^\circ \approx 1.03d$. Assuming that the path of the photoelectron is d' , $d_0 = d' - d = 0.03d$. However, if

we focus on the value of d_0 obtained from the measurement, $d_0 \gg 0.03d$, which is an inadequate explanation for d_0 .

The second is that photoelectron attenuation by the gas also occurs inside the cone. Lambert-Beer's law assumes that photoelectron attenuation occurs only from the sample surface to the cone tip. However, the inside of the cone is connected by an orifice to the outside of the cone where gas is introduced, and it is possible that gas flows into the inside of the cone and remains. In this case, attenuation of photoelectrons by the gas also occurs inside the cone, and the longer path of photoelectrons in the gas is related to d_0 . However, this is just one possibility, and further research is needed to clarify the reason.

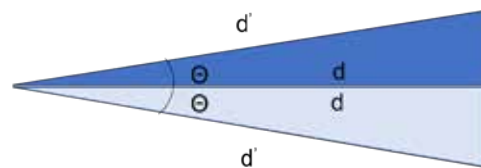


Fig 5. Schematic diagram of angular acceptance and the photoelectron

4. Conclusion

We investigated the gas pressure dependence of the spectral intensity at various distances d in NAP-HAXPES. Photoelectron intensity was found to decrease exponentially with pressure. In order to reproduce the measurement results, it is necessary to replace d in Lambert-Beer's law with $d + d_0$, where d_0 is considered to be the distance at which photoelectron decay occurs inside the cone.

Acknowledgment

HAXPES measurements were performed at the beamline BL24XU at SPring-8 (proposal no. 2020A3231 and 2020B3231).

References

- [1] Enviro™, <https://www.specs-group.com/nc/enviro/products/detail/enviroesca/>
- [2] X. R. Yu, H. Hantsche, *J. Electron Spectrosc. Relat. Phenom.* **50**, (1990), 19.
- [3] S. Matsumoto, T. Nanba, Y. Miura, *Surf. Sci.* **18**, (1997), 466.
- [4] S. Suzuki *et al.*, *J. Electron Spectrosc. Relat. Phenom.* **257**, (2022), 147192.
- [5] Scienta Omicron, <https://premium.ipros.jp/omicron/catalog/detail/557590/>.
- [6] Y. Takagi, T. Uruga, M. Tada, Y. Iwasawa, T. Yokoyama, *Acc. Chem. Res.* **51**, (2018), 719.
- [7] J. Kahk *et al.*, *J. Electron Spectrosc. Relat. Phenom.* **205**, (2015), 57.
- [8] H. Tawara, T. Kato, *At. Data Nucl. Data Tables* **36**, (1987), 167.

Shape Observation of Micro- and Nanobubbles Formed *In-situ* in a Scanning Electron Microscope

Koji Takahara, Satoru Suzuki
LASTI, University of Hyogo

Abstract

Surface microbubbles and nanobubbles were generated in situ by radiolysis of water in a liquid cell. The shape and contact angles were directly observed by scanning electron microscopy from the bubbles generated in the corners of the window. The observed contact angles were all close to 90° regardless of bubble size, indicating that the bubbles were shaped to maximize Laplace pressure. This result is the opposite of the surface bubble shape observed by AFM and is close to that reported by TEM. Bubble formation at a distance from the electron irradiation position was also analyzed by Monte Carlo simulation.

1. Introduction

In recent years, microbubbles and nanobubbles have been utilized in a variety of fields ranging from industrial fields such as agriculture and fisheries to daily necessities such as washing machines. In this study, among microbubbles and nanobubbles, surface microbubbles and surface nanobubbles, which are tiny bubbles in contact with the solid-liquid interface, are the subject of research. [1-3].

A surface bubble possesses the Laplace pressure a curvature radius-dependent additional pressure caused by surface tension [2]. The Laplace pressure increases the gas concentration gradient at the bubble-liquid interface. Simple diffusion theory predicts that a nanobubble disappears instantaneously ($\sim 100 \mu\text{s}$ for a 100 nm radius) because of the diffusion of gas molecules into the liquid, driven by the large concentration gradient. However, recent studies have revealed that the lifetime of a nanobubble reaches several months, although a detailed mechanism of the long lifetime remains unclear.

There have been several studies of surface nanobubble and microbubble shape measurements using AFM, where flattened shapes have been reported. [4-6]. However, in our previous study using SEM, hemispherical bubbles were observed at the edges of the electron-transparent window, which is contrary to previous AFM studies. Generally, a large contact angle is considered to be

disadvantageous for survival because it increases the Laplace pressure of the bubbles [7].

In this study, we report the cross-sectional SEM observation of microbubbles formed at the corner of the electron-transparent window. We also analyzed bubble formation at a location away from the irradiation site based on a Monte Carlo simulation of electron scattering in water. This report is based on our recently published paper [8].

2. Experiments

Liquid cells using Si chips with SiN or Si membranes (EM Japan Co., Ltd., Tokyo) as electron-transparent windows were constructed. The thickness and dimensions of the membrane were typically 15 nm and $100 \mu\text{m} \times 100 \mu\text{m}$, respectively. The contact angles of the water droplets on SiN and Si membranes stored in the atmosphere were approximately 92° and 88° , respectively. As far as this study is concerned, there was no clear difference in the experimental results obtained using SiN and Si membranes. Electron irradiation of the water and in situ observation were performed at room temperature in a vacuum using a conventional scanning electron microscope (JEOL, JSM-6700F). Without otherwise mentioning, the acceleration voltage was 5 kV, and the irradiation dose rate was $\sim 1 \times 10^{12} \text{ /cm}^2\text{s}$. Monte Carlo simulations were performed using the Single Scattering Monte Carlo Simulation software.

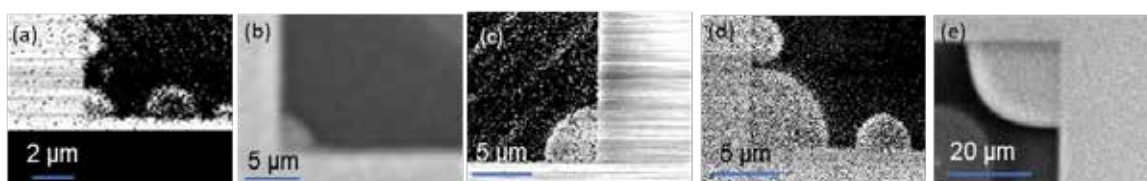


Fig. 1. (a)-(e) SEM images of bubbles with various sizes formed at the window.

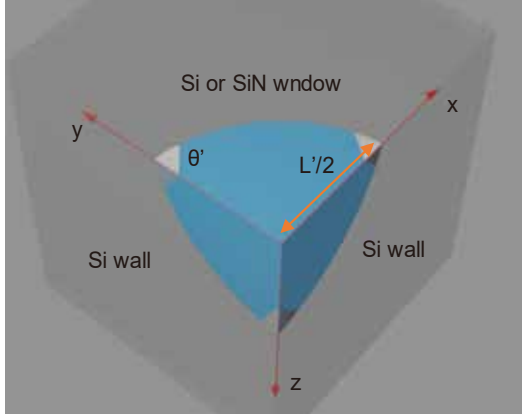


Fig. 2. Schematic of a bubble formed at a corner and definition of the observed bubble size $L'/2$ and contact angle θ' .

3. Results and discussion

3-1. Observation of bubbles formed at the corner

Fig. 1 shows a cross-sectional SEM image of electron irradiated microbubbles formed at the corners of an electron transmission window. A diagram of air bubbles formed at the corners is shown in Fig. 2. These bubbles attach to the window and two Si walls orthogonal to each other. Because the cross-section of the corner bubbles is observed via SEM, the observed size $L'/2$ does not correspond to the actual radius of curvature R . The physical properties of bubbles, such as pressure, are thought to be directly related to R , not $L'/2$. Here we assume that the wettability of the window and the wall is the same. Therefore, the shape of the bubble is expressed by a sphere with $(-a, -a, -a)$, ($a \geq 0$) as the center of the sphere as:

$$(x + a)^2 + (y + a)^2 + (z + a)^2 = R^2 \quad (1)$$

From geometrical considerations, the observed bubble size $L'/2$ and contact angle θ' are given by:

$$\frac{L'}{2} = \sqrt{R^2 - 2a^2} - a \quad (2)$$

$$\theta' = \tan^{-1}\left(\frac{L'/2 + a}{a}\right) \quad (3)$$

From eqs. (2) and (3), a and R are given by:

$$a = L'/2(\tan\theta' - 1) \quad (4)$$

$$R = \frac{L'}{2} \sqrt{1 + \frac{2}{\tan\theta' - 1} + \frac{3}{(\tan\theta' - 1)^2}} \quad (5)$$

As expected, $\theta' = 90^\circ$ results in $a = 0$ and $r = L'/2$, that is, the observed length exactly matches the real

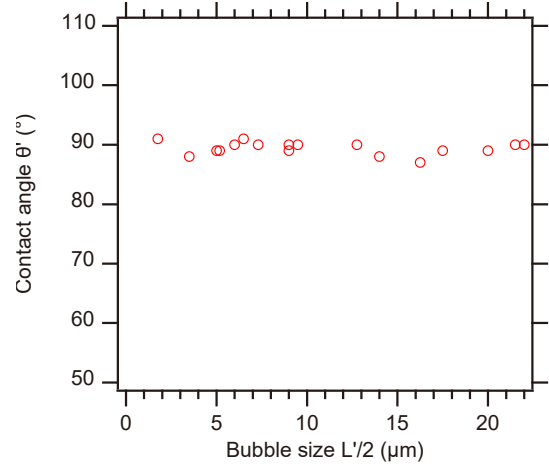


Fig. 3. Contact angles vs bubble sizes of 17 corner bubbles.

value. From eq. (3), the minimum θ' is 45° for a $\gg L'/2$. Consequently, a pancake-shaped bubble with a smaller contact angle cannot exist at the corner of the window. Therefore, if only pancake-shaped bubbles could stably exist, no bubbles would be observed at the corners. However, many microbubbles are observed at the corners. Regardless of their size, the shapes of the bubbles were very similar. The observed contact angles θ' vs. bubble sizes $L'/2$ of 17 bubbles observed at the corners are summarized in Fig. 3. All the contact angles are distributed in a narrow range close to 90° , regardless of the size observed in the SEM images. Notably, the smallest contact angle was 87° . This value gives only slight corrections: $a = 0.055L'/2$ and $R = 1.06L'/2$ from eqs. (4) and (5), respectively. The pressure inside a bubble P is given by:

$$P = P_0 + \frac{2\sigma}{R} \\ = P_0 + \frac{4\sigma}{L' \sqrt{1 + \frac{2}{\tan\theta' - 1} + \frac{3}{(\tan\theta' - 1)^2}}} \quad (6)$$

where P_0 is the pressure of the surrounding liquid, and σ is the surface tension of water (7.3×10^{-2} N/m) [9]. The second term $2\sigma/R$ is the Laplace pressure, which is approximately 1.4 atm for $R = 1 \mu\text{m}$. For a given L' , θ' of 45° and 90° provides the minimum and maximum Laplace pressures, respectively. Therefore, our results show that the bubbles have a shape that nearly maximize the Laplace pressure. This is relatively consistent with our previous observation of edge bubbles (with an average contact angle of 69° , where $0^\circ \leq \theta' \leq 90^\circ$). However, this result is contradictory to previous AFM studies. The reason behind this discrepancy is not known, and therefore, further studies are necessary.

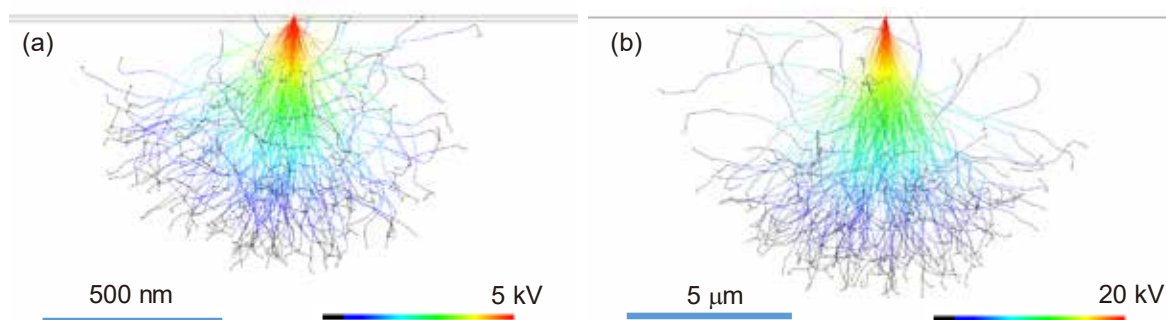


Fig. 4. Monte Carlo simulation results of electron scattering in water injected through a 15 nm thick Si window. Electron kinetic energy is (a) 5 and (b) 20 keV.

3-2. Monte Carlo simulation of electron scattering in water

Bubble formation was also observed at $\sim 25 \mu\text{m}$ away from the irradiation site, when local irradiation ($\sim 7 \times 10^{16} / \text{cm}^2\text{s}$ for 60 s) was performed at a relatively high kinetic energy of 20 keV, as shown in Fig. 4. To understand this mechanism, we performed Monte Carlo simulations of electron scattering in water. Figs. 4(a) and (b) show the simulation results obtained for electron kinetic energies of 5 and 20 keV, respectively. The incident electrons are injected into the water through a 15 nm thick Si window, demonstrating a minor effect. The increased kinetic energy significantly increases the penetration depth. The maximum penetration depths in water were estimated to be 0.70 and 8.4 μm for 5 and 20 keV, respectively. These values are consistent with those obtained from the semi-empirically derived formula (0.83 and 8.4 μm , respectively) [10]. Similarly, the lateral spreads extend to $\sim 0.5 \mu\text{m}$ and 5 μm from the irradiation site, respectively. Therefore, the radiolysis of water and formation of bubbles are considered to occur within these ranges. Once a bubble is formed, the range is further expanded as electron scattering is significantly suppressed in a gas. Because of the relatively long travelling length at 20 keV, nanobubble formation at locations away from a local irradiation site is possible when a microbubble is formed at the irradiation site. We believe that multiple nanobubbles merge at the corners and edges to grow into microbubbles.

4. Conclusion

We performed direct cross-sectional observation of bubbles formed in situ by electron irradiation. Regardless of the size of the bubbles, they were nearly hemispherical in shape, consistent with the bubbles at the edges of the window reported previously. These

shapes maximize Laplace pressure. This result is contrary to the AFM study but very close to the TEM results; further work is needed to clarify the discrepancy with the AFM study.

References

- [1] V. S. J. Craig, *Soft Matter* **7**, (2011), 40.
- [2] D. Lohse and X. Zhang, *Rev. Mod. Phys.* **87**, (2015), 981.
- [3] J. R. T. Seddon, D. Lohse, *J. Phys. Condens. Matter* **23**, 133001 (2011).
- [4] X. H. Zhang, N. Maeda, V. S. J. Craig, *Langmuir* **22**, (2006), 5025.
- [5] H. Teshima, T. Nishiyama, K. Takahashi, *J. Chem. Phys.* **146**, (2017), 014708.
- [6] T. Nishiyama, Y. Yamada, T. Ikuta, K. Takahashi, Y. Takata, *Langmuir* **31**, (2015), 982.
- [7] K. Takahara and S. Suzuki, *J. Appl. Phys.* **130**, (2021), 025302.
- [8] K. Takahara and S. Suzuki, *e-J. Surf. Sci. Nanotechnol.*, (accepted).
- [9] K. Yasui, T. Tuziuti, W. Kanematsu, K. Kato, *Phys. Rev. E* **91**, (2015), 033008.
- [10] H. Takahashi, *J. Surf. Sci. Soc. Jpn* **25**, (2004), 224.

Part 3. List of Publications



NewSUBARU Operation Room

List of publications

Papers

1. **“In situ water radiolysis in a scanning electron microscope and observation of micro- and nanobubbles formation”**
Koji Takahara and Satoru Suzuki
J. Appl. Phys. 130, 025302-1-8 (2021)
2. **“Properties and Classification of Diamond-Like Carbon Films”**
Naoto Ohtake, Masanori Hiratsuka, Kazuhiro Kanda, Hiroki Akasaka, Masanori Tsujioka, Kenji Hirakuri, Atsushi Hirata, Tsuguyori Ohana, Hiroshi Inaba, Makoto Kano, and Hidetoshi Saitoh
Materials 14, 315 (2021)
3. **“Effect of Soft X-Ray Irradiation on Film Properties of a Hydrogenated Si-Containing DLC Film”**
Kazuhiro Kanda, Ryo Imai, Shotaro Tanaka, Shuto Suzuki, Masahito Niibe, Takayuki Hasegawa, Tsuneo Suzuki, and Hiroki Akasaka
Materials 14, 924 (2021)
4. **“Performance of BL07A at NewSUBARU with installation of a new multi-layered-mirror monochromator”**
Shotaro Tanaka, Shuto Suzuki, Tomohiro Mishima, and Kazuhiro Kanda
J. Synchrotron Rad. 28, 618-623 (2021)
5. **“Soft X-ray absorption and emission spectra of nanographene prepared from pentacene with hot mesh deposition and soft X-ray irradiation”**
Akira Heya, Masahito Niibe, Kazuhiro Kanda, Ryo Yamasaki, and Koji Sumitomo
Jpn. J. Appl. Phys. 60, 045506 (2021)
6. **“Space Exposure of Amino Acids and their Precursors during the Tanpopo Mission”**
Kensei Kobayashi, Hajime Mita, Yoko Kebukawa, Kazumichi Nakagawa, Takeo Kaneko, Yumiko Obayashi, Tomohito Sato, Takuya Yokoo, Saaya Minematsu, Hitoshi Fukuda, Yoshiyuki Oguri, Isao Yoda, Satoshi Yoshida, Kazuhiro Kanda, Eiichi Imai, Hajime Yano, Hirofumi Hashimoto, Shin-ichi Yokobori, and Akihiko Yamagishi
Astrobiology 21, 1479-1493 (2021)
7. **“In situ X-ray diffraction study on structural changes of neutron-irradiated highly oriented pyrolytic graphite under room-temperature compression and decompression”**
Syusaku Nakamura, Wataru Nakamura, Shunjiro Fujii, Shin-ichi Honda, Masahito Niibe, Mititaka Terasawa, Yuji Higo, and Keisuke Niwase
Diamond Relat. Mater. 123, 108828 (2022)
8. **“Photocatalytic Activity Enhancement of Anatase/Rutile-Mixed Phase TiO₂ Nanoparticles Annealed with Low-Temperature O₂ Plasma”**
Retsuo Kawakami, Yuki Mimoto, Shin-ichoro Yanagiya, Akihiko Shirai, Masahito Niibe, Yoshitaka Nakano, and Takashi Mukai
Phys. Status Solidi A 218, 2100536 (2021)

9. **“A novel measurement approach for near-edge x-ray absorption fine structure: Continuous 2π angular rotation of linear polarization”**
Yoshiki Kudo, Yasuyuki Hirata, Masafumi Horio, Masahito Niibe, and Iwao Matsuda
Nucl. Inst. Meth. Phys. Res. A 1018, 165804 (2021)
10. **“Electronic structure of a borophene layer in rare-earth aluminum / chromium boride and its hydrogenated derivative borophane”**
Masahito Niibe, Mathis Cameau, Nyuyen Thanh Cuong, Omeji Ilemana Sunday, Xiaoni Zhang, Yuki Tsujikawa, Susumu Okada, Kunio Yubata, Takahiro Kondo, and Iwao Matsuda
Phys. Rev. Mater. 5, 084007 (2021)
11. **“In situ observation of Transformation of neutron-irradiated highly oriented pyrolytic graphite (HOPG) by X-ray diffraction under high-pressure and high-temperature treatment”**
Shin-ichi Honda, Yuji Higo, Keisuke Niwase, Masahito Niibe, Mititaka Terasawa, Eiji Taguchi, and Syusaku Nakamura
Jpn. J. Appl. Phys. 60, 095002 (2021)
12. **“Liquid Mixing Evaluated Using Entropy in a Lab-on-a-disc Platform”**
A. Yamaguchi, A. Ishimoto, S. Saegusa, M. Sugiyama, S. Amano, and Y. Utsumi
Sensors and Materials 12, 4371-4382 (2021)
13. **“Development of Microfluidic Device Coupled with Post-wall Waveguide for Microwave Heating at 24.125 GHz”**
Kaito Fujitani, Mitsuyoshi Kishihara, Tomoyuki Nakano, Ryota Tanaka, Akinobu Yamaguchi, and Yuichi Utsumi
Sensors and Materials, 33, 4399-4408 (2021)
14. **“Transporting Powder with Surface Acoustic Waves Propagating on Tilted Substrate”**
T. Saiki, Y. Takizawa, T. Kaneyoshi, K. Iimura, M. Suzuki, A. Yamaguchi, and Y. Utsumi
Sensors and Materials, 12, 4409-4426 (2021)
15. **“Manipulation of Powder with Surface Acoustic Wave Actuator to Control Standing and Traveling Modes”**
Yukako Takizawa, Yusuke Fukuchi, Kazuya Hamaguchi, Satoshi Amaya, Yuichi Utsumi, Masahiro Takeo, Kenji Iimura, Michitaka Suzuki, and Tsunemasa Saiki
Sensors and Materials 33, 4427–4439 (2021)
16. **“Fabrication of Ni-W micro-gears using LIGA Process”**
K. Tamada, S. Amano, K. Okamoto, M. Takeuchi, A. Yamaguchi, Y. Utsumi, and T. Yamasaki
Sensors and Materials 12, 4455-4460 (2021)
17. **“Observation of individual resonances in magnetic vortex core gyration using time-resolved magneto-optical Kerr microscope with picosecond laser diode illumination”**
T. Ogasawara and A. Yamaguchi
Jpn. J. Appl. Phys. 61, 018001 (2021)

18. **“Enhancement in spin-orbit torques by change in uniaxial in-plane magnetic anisotropy of Py/Pt bilayers on single crystal 128° Y-cut LiNbO₃ substrate”**
M. Ito, A. Yamaguchi, D. Oshima, T. Kato, M. Shima, and K. Yamada
Appl. Phys. Lett. 119, 152407 (2021)
19. **“X-ray photoemission spectroscopy study of uniaxial magnetic anisotropy induced in a Ni layer deposited on a LiNbO₃ substrate”**
Akinobu Yamaguchi, Takuo Ohkochi, Masaki Oura, Keisuke Yamada, Tsunemasa Saiki, Satoru Suzuki, Yuichi Utsumi, and Aiko Nakao
Nanomaterials 11, 1024 (2021)
20. **“Effect of atomic Hydrogen Exposure on Hydrogenated Amorphous Carbon Thin Films”**
Yuichi Haruyama, Daiki Morimoto, Akira Heya, Koji Sumitomo, Seigo Ito, Kumiko Yokota, and Masahito Tagawa
Jpn. J. Appl. Phys. 60, 125504 (2021)
21. **“Pencil graphite rods decorated with nickel and nickel-iron as low-cost oxygen evolution reaction electrodes”**
Ramón Arcas, Yuuki Koshino, Elena Mas-Marzá, Ryuki Tsuji, Hideaki Masutani, Eri Miura-Fujiwara, Yuichi Haruyama, Seiji Nakashima, Seigo Ito, and Francisco Fabregat-Santiago
Sustainable Energy & Fuels. 5, 3929-3938 (2021)
22. **“Development of a high-power EUV irradiation tool in a hydrogen atmosphere”**
Tetsuo Harada, Shinji Yamakawa, Mitsunori Toyoda, and Takeo Watanabe
Jpn. J. Appl. Phys. 60, 087005 (2021)
23. **“Modified-edge-support heat treatment method of polyimide for crystalline, large-area, and self-standing ultrathin graphite films”**
Kensuke Murashima, Yuki Kawashima, Shuhei Ozaki, Atsushi Tatami, Masamitsu Tachibana, Takeo Watanabe, Tetsuo Harada, and Mutsuaki Murakami
Carbon 181, 348-357 (2021)
24. **“Affinity Analysis of Photoacid Generator in the Thin Film of Chemical Amplification Resist by Contact Angle Measurement”**
Shinji Yamakawa, Aiko Yamamoto, Seiji Yasui, Takeo Watanabe, and Tetsuo Harada
J. Photopolym. Sci. Technol. 34, 111-115 (2021)
25. **“The Measurement of the Refractive Index n and k Value of the EUV Resist by EUV Reflectivity Measurement Method”**
Yosuke Ohta, Atsushi Sekiguchi, Tetsuo Harada, and Takeo Watanabe
J. Photopolym. Sci. Technol. 34, 105-110 (2021)
26. **“Study on Fabrication of X-ray collimators by X-ray lithography using synchrotron radiation”**
S. Saegusa, N. Narukage, Y. Utsumi, and A. Yamaguchi
J. Photopolym. Sci. Technol. 34, 213-218 (2021)

- 27. “Fundamental Evaluation of Resist on EUV Lithography at NewSUBARU Synchrotron Light Facility”**
Takeo Watanabe, Tetsuo Harada, Shinji Yamakawa
J. Photopolym. Sci. Technol. 34, 49-53 (2021)
- 28. “A Global Shutter Wide Dynamic Range Soft X-Ray CMOS Image Sensor With Backside-Illuminated Pinned Photodiode, Two-Stage Lateral Overflow Integration Capacitor, and Voltage Domain Memory Bank”**
Hiroya Shike, Rihito Kuroda, Ryota Kobayashi, Maasa Murata, Yasuyuki Fujihara, Manabu Suzuki, Shoma Harada, Taku Shibaguchi, Naoya Kuriyama, Takaki Hatsui, Jun Miyawaki, Tetsuo Harada, Yuichi Yamasaki, Takeo Watanabe, Yoshihisa Harada, and Shigetoshi Sugawa
IEEE Trans. Electron Devices 68, 2056-2063 (2021)
- 29. “Anisotropic pyrochemical dry etching of fluorinated ethylene propylene induced by pre-irradiation with synchrotron radiation”**
Kaito Fujitani, Masaya Takeuchi, Yuichi Haruyama, Akinobu Yamaguchi, and Yuichi Utsumi
AIP Advances 11, 025104 (2021)
- 30. “Trial Fabrication and Evaluation of PTFE Substrate Integrated Waveguide Butler Matrix for Short Millimeter-Wave”**
Mitsuyoshi Kishihara, Kaito Fujitani, Akinobu Yamaguchi, Yuichi Utsumi, and Isao Ohta
IEICE Tech. Rep. 121, 5-10 (2021)
- 31. “In situ Fluorescence Yield Soft X-ray Absorption Spectroscopy of Electrochemical Nickel Deposition Processes with and without Ethylene Glycol”**
Akinobu Yamaguchi, Naoya Akamatsu, Shunya Saegusa, Ryo Nakamura, Masaru Kato, Ichizo Yagi, Tomoko Ishihara, and Masaki Oura,
RSC Advances 12, 10425-10430 (2022)
- 32. “Physically Unclonable Functions Taggant for Universal Steganographic Prints”**
T. Fukuoka, Y. Mori, T. Yasunaga, K. Namura, M. Suzuki, and A. Yamaguchi
Scientific Reports 12, 985 (2022)
- 33. “Analysis of DNA Radiation Damage by Soft X-Ray Irradiation”**
Kazuki Yoshida,, Naoto Matsuo,, Kazushige Yamana, Koji Sumitomo, Akira Heya, Tetsuo Harada, Tetsuo Tabei, Abstracts of IEICE TRANSACTIONS on Electronics (Japanese Edition), J105-C, 74-77 (2022)

Books

1. **“Nanomagnetic Materials: Fabrication, Characterization and application“**
A. Yamaguchi, A. Hirohata, B. Stadler, (Editor&Author) , Elsevier, 2021 (ISBN 978-0128223499)

Proceedings

1. **“Construction of a Compact Electron Injector Using A Gridded Rf Thermionic Gun And A C-Band Accelerator“**
T. Inagaki, T. Fukui, T. Hara, T. Hiraiwa, H. Maesaka, H. Tanaka, T. Asaka, H. Dewa, N. Hosoda, E. Iwai, C. Kondo, T. Magome, T. Ohshima, T. Sakurai, K. Yanagida, S. Inoue, K. Kajimoto, Y. Minagawa, S. Nakata, T. Seno, H. Sumitomo, R. Takesako, S. Tanaka, R. Yamamoto, M. Yoshioka, and S. Hashimoto
IPAC2021, WEPAB039 (2021)
2. **“Commissioning of the new 1.0GeV electron linac for NewSUBARU storage ring”**
Takahiro Inagaki, Toshihiko Hiraiwa, Hirokazu Maesaka, Toru Hara, Hitoshi TanakaA), Takao Asaka, Hideki Dewa, Naoyasu Hosoda, Eito Iwai, Chikara Kondo, Tamotsu Magome, Takashi Ohshima, Tatsuyuki Sakurai, Kenichi Yanagida, Yousuke Hamada, Takashi Sugimoto, Toshiro Itoga, Noriyoshi Adumi, Satoshi Hashimoto, Hitoshi Fujii, Shinobu Inoue, Kazuyuki Kajimoto, Yasuyuki Minagawa, Shotaro Nakata, Hiroshi Sumitomo, Shinichiro Tanaka, Ryo Yamamoto, Masamichi Yoshioka, Nobuyuki Nishimori, Kota Ueshima, Yuji Hosaka, and Taiki Iwashita
Proc. of 18th. Particle Accelerator Society in Japan Annual Meeting, TUOB03, p.102 (2021)
3. **“Present status of the NewSUBARU synchrotron light facility”**
Satoshi Hashimoto, Hitoshi Fujii, Hamada Yousuke, Yasuyuki Minagawa, Kazuyuki Kajimoto, Shoutarou Nakata, Hideyuki Hirayama, and Shinichirou Tanaka
Proc. of 18th. Particle Accelerator Society in Japan Annual Meeting, THP057, p.978 (2021)
4. **“Operation status and high power rf conditioning results of C-band main accelerator at NewSUBARU injector”**
Takahiro Inagaki, Takao Asaka, Chikara Kondo, Takashi Ohshima, Eito Iwai, Masamichi Yoshioka, Hiroshi Sumitomo, Yasuyuki Minakawa, Kazuyuki Kajimoto, Shinichiro Tanaka, and Satoshi Hashimoto
Proc. of 18th. Particle Accelerator Society in Japan Annual Meeting, THP033, p.895 (2021)
5. **“Damage-Less Removal of Surface Contamination Using Atomic Hydrogen Generated on Heated Tungsten Mesh”**
Akira Heya, Tetsuo Harada, Masahito Niibe, Koji Sumitomo, and Takeo Watanabe
Proc. SPIE, 11908, 119080S (2021)
6. **“Hydrogen damage and cleaning evaluation of Mo/Si multilayer using high-power EUV irradiation tool”**
Tetsuo Harada, Ayato Ohgata, Shinji Yamakawa, and Takeo Watanabe
Proc. SPIE 11908, 119080U (2021)

- 
7. **“Beyond EUV measurement at NewSUBARU synchrotron light facility”**
Takuto Fujii, Shinji Yamakawa, Tetsuo Harada, and Takeo Watanabe
Proc. SPIE 11908, 119080T (2021)
 8. **“Ultra-low density, nanostructured free-standing films for EUV Pellicles”**
Márcio D. Lima, Takahiro Ueda, Luis Plata, Yang Yang, Vincent Le, Nicklas Keller, Chi Huynh,
Tetsuo Harada, Takeshi Kondo
Proc. SPIE 11517, 1151709 (2021)
 9. **“Fundamental research activities on EUV lithography at NewSUBARU synchrotron light facility”**
Takeo Watanabe, Tetsuo Harada, and Shinji Yamakawa
Proc. SPIE 11908, 1190807 (2021)

International Meetings

1. **“Space Exposure of Amino Acids and Amino Acid Precursors in the Tanpopo and the Tanpopo 2 Missions”**
Hirofumi Hashimoto, Hajime Mita, Shin-ichi Yokobori, Kazuhiro Kanda, Akihiko Yamagishi, Hiromi Shibata, Itsuki Sakon, Tomohiro Sato, Kazumichi Nakagawa, Yoko Kebukawa, Isao Yoda, Hajime Yano, Miki Nakayama, Hitoshi Fukuda, Yoshiyuki Oguri, Satoshi Yoshida, Takuya Yokoo, Kai Terasawa, and Jun-ichi Takahashi
43rd Connecting space research for global impact Scientific Assembly (COSPAR2021), Online, 2021/1-2
2. **“Hydrogen damage and cleaning evaluation of Mo/Si multilayer using high-power EUV irradiation tool”**
Tetsuo Harada, Ayato Ohgata, Shinji Yamakawa, and Takeo Watanabe
Photomask Japan 2021, Online, 2021/4
3. **“Beyond EUV measurement at NewSUBARU synchrotron light facility”**
Takuto Fujii, Shinji Yamakawa, Tetsuo Harada, and Takeo Watanabe
Photomask Japan 2021, Online, 2021/4
4. **“Damage-less removal of surface contamination using atomic hydrogen generated on heated tungsten mesh”**
Akira Heya, Tetsuo Harada, Masahito Niibe, Koji Sumitomo, and Takeo Watanabe
Photomask Japan 2021, Online, 2021/4
5. **“Fundamental research activities on EUV lithography at NewSUBARU synchrotron light facility”**
Takeo Watanabe, Tetsuo Harada, and Shinji Yamakawa
Photomask Japan 2021, Online, 2021/4
6. **“Aqueous-soluble Ink including Nano Beacon”**
Akinobu Yamaguchi, Yuichi Utsumi, Kyoko Namura, Motofumi Suzuki, and Takao Fukuoka
Pittcon 2021, L51-03, Oral, 2021/3
7. **“X-ray radiolysis-induced-photochemical Reaction at Interface between liquid and substrate”**
Shunya Saegusa, Naoya Akamatsu, Ikuya Sakurai, Ikuo Okada, Yuichi Utsumi, and Akinobu Yamaguchi
2021 International Conference on Electronics Packaging (ICEP 2021), TB3-2, Oral, 2021/5
8. **“Affinity Analysis of Photoacid Generator in the Thin Film of Chemical Amplification Resist by Contact Angle Measurement”**
Shinji Yamakawa, Ako Yamamoto, Seiji Yasui, Takeo Watanabe, and Tetsuo Harada
ICPST-38, Online, 2021/6
9. **“The Measurement of the Refractive Index n and k Value of the EUV Resist by EUV Reflectivity Measurement Method”**
Yosuke Ohta, Atsushi Sekiguchi, Tetsuo Harada, and Takeo Watanabe
ICPST-38, Online, 2021/6

10. **“Fundamental Evaluation of Resist on EUV Lithography at NewSUBARU Synchrotron Light Facility”**
Takeo Watanabe, Tetsuo Harada, and Shinji Yamakawa
ICPST-38, Online, 2021/6
11. **“EUV Resist Development Program at NewSUBARU”**
Takeo Watanabe, Shinji Yamakawa, and Tetsuo Harada
2021 EUVL Workshop, Online, 2021/6
12. **“In-situ X-ray diffraction study on structural changes of neutron-irradiated highly oriented pyrolytic graphite under room-temperature compression and decompression”**
S. Nakamura, M. Ichikawa, W. Nakamura, S. Fujii, S. Honda, M. Niibe, M. Terasawa, Y. Higo, and K. Niwase
4th International Conf. On New Diamond and Nano Carbon, Online, 2021/6
13. **“Study on spin-orbit-torque induced magnetization modulation using planar Hall effect in cross-shaped multilayer wires”**
A. Yamaguchi, N. Matsumoto, W. Yoshikawa, and Y. Fujii
Micro and Nano Engineering Conference (MNE) 2021, Turin, Italy, (Hybrid), Poster, 2021/9
14. **“X-ray-induced photo-processes for functional nano/microstructures and materials in aqueous liquid solutions”**
A. Yamaguchi, S. Saegusa, I. Sakurai, I. Okada, M. Ishihara, and Y. Utsumi
Micro and Nano Engineering Conference (MNE) 2021, Turin, Italy, (Hybrid), Poster, 2021/9
15. **“pH dependence of X-ray-induced synthesis and immobilization of nickel nano/microparticles”**
S. Saegusa, I. Sakurai, I. Okada, M. Ishihara, Y. Utsumi, and A. Yamaguchi
Micro and Nano Engineering Conference (MNE) 2021, Turin, Italy, (Hybrid), Poster, 2021/9
16. **“Structural and Electrical Properties of Nanographene Prepared from Pentacene by Hot Mesh Deposition and Soft X-ray Irradiation”**
Akira Heya, Masahito Niibe, Kazuhiro Kanda, Ryo Yamasaki, and Koji Sumitomo
28th International Workshop On Active-Matrix Flatpanel Displays and Devices, Online, 2021/6-7
17. **“The measurement of the refractive index n and k value of the EUV resist by EUV reflectivity measurement method”**
Yosuke Ohta, Atsushi Sekiguchi, Tetsuo Harada, and Takeo Watanabe
MNC 2021, Online, 2021/10
18. **“Fundamental Study of the Origin of the Stochastics in EUV Resist”**
Takeo Watanabe, Tetsuo Harada, and Shinji Yamakawa
MNC 2021, Online, 2021/10
19. **“Anisotropic pyrochemical dry etching of fluorinated ethylene propylene initiated by irradiation of synchrotron radiation”**
K. Fujitani, Y. Haruyama, A. Yamaguchi, S. Amano, and Y. Utsumi
MNC 2021, Online, 2021/10

20. **“Photobacterial Activity of Anatase Titanium Dioxide Nanoparticles Annealed with the Assistance of Nonequilibrium Atmospheric-Pressure Oxygen Plasma”**
R. Kawakami, Y. Mimoto, A. Shirai, S. Yanagiya, M. Niibe, Y. Nakano, and T. Mukai
42nd International Symposium on Dry Process (DPS2021), Online, 2021/11
21. **“Nonequilibrium Atmospheric-Pressure O₂ Plasma-Assisted Annealing Effect on Photocatalytic Activity of Anatase/Rutile-Mixed Phase TiO₂ Nanoparticles”**
Y. Mimoto, R. Kawakami, S. Yanagiya, M. Niibe, Y. Nakano, and T. Mukai
42nd International Symposium on Dry Process (DPS2021), Online, 2021/11
22. **“In situ formation of micro- and nanobubbles by water radiolysis in a scanning electron microscope”**
Koji Takahara and Satoru Suzuki
9th International Symposium on Surface Science (ISSS-9), Online, 2021/11-12
23. **“Cross-sectional Observation of Micro- and Nanobubbles Formed In-situ in a Scanning Electron Microscope”**
Koji Takahara and Satoru Suzuki
9th International Symposium on Surface Science (ISSS-9), Online, 2021/11-12
24. **“Elimination of the charging effect in near-ambient-pressure hard X-ray photoelectron spectroscopy”**
Kento Takenaka, Kenta Adachi, Koji Takahara, Hirosuke Sumida, and Satoru Suzuki
9th International Symposium on Surface Science (ISSS-9), Online, 2021/11-12
25. **“Soft X-ray L-emission spectra of S, Cl and K elements obtained by high energy resolution spectrometer”**
Masahito Niibe and Takashi Tokushima
9th International Symposium on Surface Science (ISSS-9), Online, 2021/11-12
26. **“Soft X-ray Absorption, Emission and Photoelectron Spectroscopy of Ammonia Borane (NH₃BH₃)”**
Masahito Niibe, Yuichi Haruyama, and Seigo Ito
9th International Symposium on Surface Science (ISSS-9), Online, 2021/11-12
27. **“Removal of Si Native Oxide by Irradiating Atomic Hydrogen”**
D. Morimoto, A. Heya, K. Sumitomo, S. Ito, S. Suzuki, and Y. Haruyama
9th International Symposium on Surface Science (ISSS-9), Online, 2021/11-12
28. **“Effect of Atomic Hydrogen Exposure on Hydrogenated Amorphous Carbon Films”**
Yuichi Haruyama, Daiki Morimoto, Akira Heya, Koji Sumitomo, Seigo Ito, Kumiko Yokota, and Masahito Tagawa
9th International Symposium on Surface Science (ISSS-9), Online, 2021/11-12
29. **“Biomimetic Diamond-like Carbon Coating on a Lumen of Small-diameter Long-sized Tube Functionalized by Oxygen Plasma Treatment”**
Yuichi Imai, Tatsuyuki Nakatani, Kazuhiro Kanda, Shinsuke Knitsugu, Yasuhiro Fujii, Daiki Ousaka, Susumu Ouzawa, and Tomio Uchi
Material research meeting 2021 (MRM2021), Yokohama, 2021/12

- 30. “Totally-viewed structural analysis on DLC films using low energy positron beam, soft x-ray beam and high energy ion beam”**
Kazuhiro Kanda, Masahito Niibe, Hiroki Akasaka, Tsuneo Suzuki, Fuminobu, Hori, Atsushi Yabuuchi, and Atsushi Kinomura
International Chemical Congress of Pacific Basin Societies 2021 (Pacifichem2021), Online, 2021/12
- 31. “Formation and robustness of complex amino acid precursors with large molecular weights in space”**
Kensei Kobayashi, Soushi Kuramoto, Tomohito Sato, Yoko Kebukawa, Hajime Mita, Hitoshi Fukuda, Yoshiyuki Oguri, Kazuhiro Kanda, and Hiromi Shibata
International Chemical Congress of Pacific Basin Societies 2021 (Pacifichem2021), Online, 2021/12
- 32. “Study of electrochemical reaction of nickel sulfamate with ethylene glycol using X-ray absorption fluorescence spectroscopy”**
N. Akamatsu, S. Saegusa, R. Nakamura, Y. Utsumi, M. Kato, I. Yagi, T. Ishihara, M. Oura, and A. Yamaguchi
Pacifichem 2021, Oral, 2021/12
- 33. “Synthesis and deposition of nano/micro-copper particles using X-ray radiolysis-induced-photochemical reaction”**
A. Yamaguchi, I. Sakurai, I. Okada, M. Ishihara, and Y. Utsumi
Pacifichem 2021, Poster, 2021/12
- 34. “Study on X-ray-radiolysis-based deposition of nano/micro-copper particles as three dimensional additive manufacturing process”**
A. Yamaguchi, I. Sakurai, U. Okada, A. Yamaguchi, M. Ishihara, and Y. Utsumi
Pacifichem 2021, Poster, 2021/12
- 35. “Simulation verification of forward/reverse analysis in big data of 4D-XPS measurements”**
Satoshi Toyoda, Masashi Yoshimura, Hirosuke Sumida, Susumu Mineoi, Masatake Machida, Akitaka Yoshigoe, Akira Yoshikawa, Satoru Suzuki, and Kazushi Yokoyama
27th Workshop on Electron Device Interface Technology (EDIT27), Online, 2022/1

Academic Degrees

Master of Engineering

Takuto Fujii (University of Hyogo)

“Improvement of optical system for the carbon region and Beyond-EUV utilization at BL-09 beamline of NewSUBARU”

Naoya Akamatsu (University of Hyogo)

“Creation of microsystems for controlling chemical reactions”

Kaito Fujitani (University of Hyogo)

“Microfabrication of fluorine resin FEP by Synchrotron Radiation photochemical reaction and application to microwave-induced chemical reaction chip”

Shota Matsuo (University of Hyogo)

"Advanced Electron Beam Anomaly Detection with Machine Learning at NewSUBARU”

LASTI Annual Report Vol. 23 (2021)

February 2023, Published by
Laboratory of Advanced Science and Technology for Industry
University of Hyogo
3-1-2 Kouto, Kamigori-Cho, Ako-gun, Hyogo 678-1205, JAPAN
Phone: +81-791-58-0249 / FAX: +81-791-58-0242

Editorial board

Takeo Watanabe (Editor in Chief)
Akinobu Yamaguchi
Koji Nakanishi
Yuichi Haruyama

Laboratory of Advanced Science and Technology for Industry,
University of Hyogo

3-1-2 Kouto, Kamigori, Ako-gun, Hyogo 678-1205 Japan

兵庫県立大学 高度産業科学技術研究所

〒678-1205 兵庫県赤穂郡上郡町光都 3-1-2

